

**STUDY OF THE SELF NOISE GENERATED BY
VENTILATED SUPERCAVITATING VEHICLES**

Jeffrey Gilbert and Michael Howe
Boston University, College of Engineering
110 Cummington Mall, Boston MA 02215

30 April, 2015

Final Technical Report of work performed under
ONR Grant No. N00014-11-1-0314
University/Laboratory Initiative

Prepared for
Office of Naval Research, Code 333
875 N. Randolph St., One Liberty Center
Arlington, VA 22203-1995

ABSTRACT

This study investigates the self noise from a ventilated supercavitating vehicle. A ventilated supercavity is a gaseous envelope surrounding an underwater vehicle that significantly reduces the drag felt by the vehicle. But the hydrodynamic noise generated by the creation of the supercavity could impact the successful deployment of the vehicle. A principal source of self noise for these types of vehicles is sound created by the ventilating gas jets impinging on the air-water interface. Analytical models of the radiated sound through the interface have been developed. Sometimes jets impinging on the interface entrain bubbles beneath the surface. This thesis outlines a theory to predict the influence of bubbles near the interface.

Experimental measurements were made at the Naval Undersea Warfare Center (NUWC) in Newport, RI to test the accuracy of the model. These measurements include the unsteady force spectrum of a gas jet impinging on a rigid wall. The acoustic pressure spectrum of a gas jet striking the air-water interface was also recorded. The experimental results were compared to theoretical models for validation.

Contents

1	Introduction	1
1.1	Motivation	1
1.2	Background	2
1.2.1	Cavitation	2
1.2.2	Supercavitating vehicles	3
1.2.3	Free gas jets impinging on plates	6
1.2.4	Underwater Noise	7
1.3	Approach	9
1.4	Outline	10
2	Measurements of the jet exit velocity and in air acoustic spectrum	12
2.1	Experimental setup and procedure	12
2.2	Data Analysis	14
2.2.1	Compressible gas flow theory	14
2.2.2	Post-processing	17
2.2.3	Uncertainty	18
2.3	Results	19

2.3.1	Jet exit velocity measurements	19
2.3.2	In air acoustic pressure spectrum measurements	28
2.4	Conclusions	31
3	Measurements of the unsteady force spectrum of a gas jet impacting a rigid wall	32
3.1	Experimental setup and procedure	32
3.2	Data Analysis	36
3.2.1	Post processing	36
3.2.2	Uncertainty	36
3.3	Results	37
3.3.1	Comparison with Foley	42
3.4	Conclusions	46
4	Acoustic measurements of gas jets impacting a planar air-water interface	47
4.1	Experimental setup and procedures	47
4.2	Data analysis	50
4.2.1	Post-processing	50
4.2.2	Uncertainty	51
4.3	Results	52
4.3.1	Relationship between jet velocity and acoustic power	57
4.4	Conclusions	68

5 Acoustic measurements of gas jets generating bubble entrainment at the air-water interface	69
5.1 Experimental setup and procedures	69
5.2 Data analysis	71
5.2.1 Post-processing	71
5.2.2 Uncertainty	72
5.3 Results	72
5.4 Conclusions	75
6 Sound generated by a gas-jet impingement on a bubbly gas-water interface	76
6.1 The acoustic problem	77
6.2 Foley's problem	77
6.2.1 Comparison of acoustic model to measured results	79
6.3 Influence of a bubbly cloud	88
6.3.1 Mean properties of the cloud	88
6.3.2 Calculation of the radiated sound	90
6.3.3 The far field pressure	93
6.3.4 The acoustic pressure frequency spectrum	94
6.3.5 Comparisons with measured acoustic power	96
6.4 Influence of a bubbly layer	101
6.4.1 Mean properties of the bubble layer	101

6.4.2 Calculation of the radiated sound	102
6.4.3 The far field acoustic pressure	104
6.4.4 The acoustic pressure frequency spectrum	106
6.5 Conclusions	110
7 Conclusions	112
7.1 Summary	112
7.2 Recommendations to reduce self noise	113
7.3 Recommendations of future work	114
A Review of select topics in linear acoustics	119
A.1 The linear wave equation	119
A.2 Acoustic impedance, intensity, and power	123
A.3 Acoustic compactness and the near and far fields	125
A.4 Monopoles, dipoles, and quadrupoles	125
B Acoustic Green's function	127
C Equipment specifications	130
C.1 Flow rate sensor, Sierra 824 Top-Trak Mass Flow Meter	130
C.2 Pressure sensor, Omega PX209 Pressure Transducer	130
C.3 Temperature sensor, Omega SCASS-1256-6 Thermocouple	131
C.4 In air microphone, Brüel and Kjaer 4938 Series Microphone	131

C.5 Unsteady force transducers, PCB Piezotronics 208C01 and 208A11 Dynamic Force Sensors	131
C.6 Hydrophones, G.R.A.S. 10CC Hydrophone	132
D Bibliography	133

List of Tables

3.1	Test matrix for the force measurement experiments.	35
4.1	Test matrix for acoustic measurements on Aug. 20-21 of 2012 at ATF.	50

List of Figures

1.1	Supercavitating vehicle in a water tunnel with a smooth cavity surface.	5
1.2	Supercavitating vehicle in a water tunnel with a rough and bubbly cavity surface.	5
1.3	Acoustic paths of transmission for a supercavitating vehicle with a deflector.	6
2.1	Gas jet ventilation system with pressure, temperature, and flow rate sensors. These sensors measure p_1 , T_1 , and Q_1 , respectively.	13
2.2	Gas jet exit velocity for the $1/16''$ nozzle with a goal velocity of 140 ft/s.	20
2.3	Gas jet exit velocity for the $1/16''$ nozzle with a goal velocity of 180 ft/s.	20
2.4	Gas jet exit velocity for the $1/16''$ nozzle with a goal velocity of 220 ft/s.	21
2.5	Gas jet exit velocity for the $1/8''$ nozzle with a goal velocity of 140 ft/s.	22
2.6	Gas jet exit velocity for the $1/8''$ nozzle with a goal velocity of 180 ft/s.	22
2.7	Gas jet exit velocity for the $1/8''$ nozzle with a goal velocity of 220 ft/s.	23
2.8	Gas jet exit velocity for the $3/16''$ nozzle with a goal velocity of 140 ft/s.	24

2.9	Gas jet exit velocity for the 3/16" nozzle with a goal velocity of 180 ft/s.	24
2.10	Gas jet exit velocity for the 3/16" nozzle with a goal velocity of 220 ft/s.	25
2.11	Gas jet exit velocity for the 0.355" nozzle with a goal velocity of 140 ft/s.	26
2.12	Gas jet exit velocity for the 0.355" nozzle with a goal velocity of 180 ft/s.	26
2.13	Gas jet exit velocity for the 0.355" nozzle with a goal velocity of 220 ft/s.	27
2.14	Gas jet exit velocity for the 1/16" nozzle with the pressure regulator set to 50 psi.	28
2.15	In air measurement of the free gas jet with a nozzle diameter of 1/16" and an exit velocity of 180 ft/s.	29
2.16	In air measurement of the free gas jet with a nozzle diameter of 1/8" and an exit velocity of 180 ft/s.	29
2.17	In air measurement of the free gas jet with a nozzle diameter of 3/16" and an exit velocity of 180 ft/s.	30
2.18	In air measurement of the free gas jet with a nozzle diameter of 0.355" and an exit velocity of 180 ft/s.	30
3.1	Layout of the force sensors on the steel plate.	33
3.2	Top view of the force sensors and accelerometer.	34
3.3	Side view of the force sensors and jet nozzle.	34

3.4	Power spectral density measurements of the force sensors for 1/16" jet diameter.	38
3.5	Power spectral density measurements of the force sensors for 1/8" jet diameter.	39
3.6	Power spectral density measurements of the force sensors for 3/16" jet diameter.	39
3.7	Power spectral density measurements of the force sensors for 0.355" jet diameter.	40
3.8	Force sensor power spectral density for the 1/8" diameter nozzle and exit velocity of 222 ft/s. The plot to the right is the accelerometer data from the same run.	40
3.9	Force sensor power spectral density for the 1/16" diameter nozzle with the input pressure set to 50 psi. The plot to the right is the accelerometer data from the same run.	41
3.10	Force sensor power spectral density for the 1/8" diameter nozzle with the input pressure set to 50 psi. The plot to the right is the accelerometer data from the same run.	41
3.11	Comparison with the unsteady force measurements made by Foley for an 1/8" nozzle with an exit velocity of 140 ft/s.	43
3.12	Comparison with the unsteady force measurements made by Foley for an 1/8" nozzle with an exit velocity of 180 ft/s.	43
3.13	Comparison of the normalized unsteady force for the 1/8" nozzle at an exit velocity of 220 ft/s with the empirical curve fit from equation 3.3.1, $\alpha = 25$, $\epsilon = 0.5$	45

3.14 Comparison of the normalized unsteady force for the 1/8" nozzle at an exit velocity of 180 ft/s with the empirical curve fit from equation 3.3.1, $\alpha = 25$, $\epsilon = 0.5$	45
3.15 Comparison of the normalized unsteady force for the 1/8" nozzle at an exit velocity of 140 ft/s with the empirical curve fit from equation 3.3.1, $\alpha = 25$, $\epsilon = 0.3$	46
4.1 Hydrophone layout for acoustic experiments on Aug. 20-21 of 2012 at the ATF.	49
4.2 Comparisons of smoothed pressure frequency spectrum and raw pressure frequency spectrum data.	51
4.3 Measured acoustic pressure spectrums for the 1/16" nozzle jets. . . .	52
4.4 Measured acoustic pressure spectrums for the 1/8" nozzle jets. . . .	53
4.5 Measured acoustic pressure spectrums for the 3/16" nozzle jets. . . .	53
4.6 Measured acoustic pressure spectrums for the 0.355" nozzle jets. . . .	54
4.7 Picture of indentation created by a 1/16" nozzle jet with an exit velocity of 220 ft/s. The indentation is at a relative maximum of about 3/8".	55
4.8 Picture of indentation created by a 1/16" nozzle jet with an exit velocity of 220 ft/s taken 5 frames after Figure 4.7. The indentation is at a relative minimum of about 1/4".	56
4.9 Picture of indentation created by a 1/8" nozzle jet with an exit velocity of 220 ft/s. The indentation is at a relative maximum of about 1.25".	56

4.10 Picture of indentation created by a 1/8" nozzle jet with an exit velocity of 220 ft/s taken 8 frames after Figure 4.9. The indentation is at a relative minimum of about 1"	57
4.11 Average acoustic power spectrum vs the log of the velocity for the 1/16" nozzle. This plot shows no dependence on exit velocity.	58
4.12 Average acoustic power spectrum vs the log of the velocity for the 1/8" nozzle. The slope of the data fit is $\beta = 1.98$	59
4.13 Average acoustic power spectrum vs the log of the velocity for the 3/16" nozzle. The slope of the data fit is $\beta = 2.55$	59
4.14 Average acoustic power spectrum vs the log of the velocity for the 0.355" nozzle. The slope of the data fit is $\beta = 4.622$	60
4.15 Comparison of measured acoustic spectra between 2012 and 2013 with jet exit velocities of 140 ft/s.	61
4.16 Comparison of measured acoustic spectra between 2012 and 2013 with jet exit velocities of 220 ft/s.	61
4.17 Average acoustic power spectrum vs the log of the velocity for the 3/16" nozzle taken in 2013. The slope of the data fit is $\beta = 3.45$	62
4.18 Average acoustic power spectrum between 2-7 kHz vs the log of the velocity for the 1/8" nozzle taken in 2012. The slope of the data fit is $\beta = 1.04$	63
4.19 Average acoustic power spectrum between 7-20 kHz vs the log of the velocity for the 1/8" nozzle taken in 2012. The slope of the data fit is $\beta = 1.45$	64

4.20 Average acoustic power spectrum between 20-50 kHz vs the log of the velocity for the 1/8" nozzle taken in 2012. The slope of the data fit is $\beta = 2.56$.	64
4.21 Average acoustic power spectrum between 2-7 kHz vs the log of the velocity for the 3/16" nozzle taken in 2012. The slope of the data fit is $\beta = 2.27$.	65
4.22 Average acoustic power spectrum between 7-20 kHz vs the log of the velocity for the 3/16" nozzle taken in 2012. The slope of the data fit is $\beta = 2.82$.	65
4.23 Average acoustic power spectrum between 20-50 kHz vs the log of the velocity for the 3/16" nozzle taken in 2012. The slope of the data fit is $\beta = 2.52$.	66
4.24 Average acoustic power spectrum between 2-7 kHz vs the log of the velocity for the 0.355" nozzle taken in 2012. The slope of the data fit is $\beta = 2.54$.	66
4.25 Average acoustic power spectrum between 7-20 kHz vs the log of the velocity for the 0.355" nozzle taken in 2012. The slope of the data fit is $\beta = 2.75$.	67
4.26 Average acoustic power spectrum between 20-50 kHz vs the log of the velocity for the 0.355" nozzle taken in 2012. The slope of the data fit is $\beta = 5.46$.	67
5.1 Pressure spectrum for 1/16" nozzle, pressure regulator set to 50 psi for bubble entrainment.	73

5.2	Pressure spectrum for 1/8" nozzle, pressure regulator set to 50 psi for bubble entrainment.	74
5.3	Underwater image of the bubble cloud produced by the 1/16" nozzle set to 50 psi for bubble entrainment.	74
5.4	Underwater image of the bubble cloud produced by the 1/8" nozzle set to 50 psi for bubble entrainment.	75
6.1	Foley's model used to estimate the sound generated by an unsteady jet incident normally on the gas-water interface.	77
6.2	Predicted acoustic model for the 1/16" nozzle.	81
6.3	Predicted acoustic model for the 1/8" nozzle.	81
6.4	Predicted acoustic model for the 3/16" nozzle.	82
6.5	Predicted acoustic model for the 0.355" nozzle.	82
6.6	Comparison of measured and predicted acoustic pressure spectrum for the 1/8" nozzle with an exit velocity of 220 ft/s.	83
6.7	Comparison of measured and predicted acoustic pressure spectrum for the 3/16" nozzle with an exit velocity of 220 ft/s.	83
6.8	Comparison of measured and predicted acoustic pressure spectrum for the 0.355" nozzle with an exit velocity of 220 ft/s.	84
6.9	Average modeled acoustic power spectrum vs the log of the velocity for the 1/8" nozzle over the 2-7 kHz frequency range. The slope of the data fit is $\beta = 1.82$	86
6.10	Average modeled acoustic power spectrum vs the log of the velocity for the 3/16" nozzle over the 2-7 kHz frequency range. The slope of the data fit is $\beta = 2.21$	86

6.11 Average modeled acoustic power spectrum vs the log of the velocity for the 3/16" nozzle over the 7-17 kHz frequency range. The slope of the data fit is $\beta = 2.43$.	87
6.12 Average modeled acoustic power spectrum vs the log of the velocity for the 0.355" nozzle over the 2-7 kHz frequency range. The slope of the data fit is $\beta = 2.19$.	87
6.13 Average modeled acoustic power spectrum vs the log of the velocity for the 0.355" nozzle over the 7-20 kHz frequency range. The slope of the data fit is $\beta = 3.63$.	88
6.14 Production of sound by a jet incident on the water interface in the presence of a hemispherical bubble cloud.	89
6.15 Mean gain $G(\omega)$ in the sound pressure level produced by a hemispherical bubble cloud of nominal radius 5 cm for different values of the bubble resonance frequency f_b . The 'Raw gain' is calculated without averaging with respect to the cloud radius when $f_b = 50$ kHz.	95
6.16 Predicted acoustic gains through a bubble hemisphere with a radius of 2.5" composed of bubbles with individual radii of 0.032".	97
6.17 Measured acoustic pressure spectrum, 0-5 kHz, for the 1/16" nozzle set to 50 psi.	98
6.18 Measured acoustic pressure spectrum, 0-5 kHz, for the 1/8" nozzle set to 50 psi.	98

6.19 Comparison of modeled bubble hemisphere acoustic results and measured pressure spectrums for the 1/16" set at 50 psi. The hemisphere was modeled with a radius of 1.18" composed of bubbles with internal radii of .0354"	100
6.20 Comparison of modeled bubble hemisphere acoustic results and measured pressure spectrums for the 1/8" set at 50 psi. The hemisphere was modeled with a radius of 1.18" composed of bubbles with internal radii of .0354"	100
6.21 Model used to calculate the sound generated when the jet is incident normally on the lower face $x_3 = 0$ of a uniform bubbly interface between the cavity in $x_3 < 0$ and water in $x_3 > h$	102
6.22 The non-dimensional acoustic pressure frequency spectrum. The dashed line is for $h = 0$ and the solid line is for a bubble layer of thickness 0.39"	107
6.23 Illustrating the variation of $\Delta(\Omega, \theta)$ when $\theta = 0^0$, $\bar{\rho} = 980 \text{ kg/m}^3$, $\bar{c}_o = 100 \text{ m/s}$, $h_{\max} = 10 \text{ mm}$ and $f_b = 5, 10, 20, 30, 40 \text{ kHz}$	109
6.24 The non-dimensional acoustic pressure frequency spectrum in the normal direction $\theta = 0$ and conditions (6.4.16),(6.4.18). The dotted line represents Foley's spectrum [7,8] for $h = 0$. The solid lines are of the rectified acoustic spectrum for $h_{\max} = 10 \text{ mm}$ and $f_b = 5, 10, 20, 30, 40 \text{ kHz}$	110
7.1 Diagram of gas jet interacting with a deflector plate normal to the interface.	115

7.2 Diagram of gas jet interacting with a deflector in a cavity oriented in the forward direction.	117
A.1 Directivity of the sound from a dipole and quadrupole source.	126

Chapter 1

Introduction

A supercavity is a volume of gas that completely encloses an underwater vehicle.

The supercavity is created and sustained by continually injecting gas into the region where cavitation first occurs. Hydrodynamic 'self-noise' generated by the supercavity could interfere with the successful deployment of the vehicle. In order to reduce this problem it is necessary to understand the noise production mechanisms.

One of the principal sources of noise is believed to be the gas ventilation system, and the outcome of this project will be to study its impact on the vehicle self noise.

This project is an extension of work done by Foley investigating sound generated by a supercavitating vehicle [1,2].

1.1 Motivation

The U.S. Navy is interested in developing high-speed supercavitating underwater vehicles. The Office of Naval Research is coordinating the collaborative effort between various naval laboratories. The primary goal of this project is to get a better understanding of the self-noise generated by the gas ventilation system. This includes investigating the influence of bubbles near the air-water

interface on the radiated sound. This study will allow vehicle designers to make informed decisions about the gas ventilation systems used in supercavitating vehicles.

1.2 Background

1.2.1 Cavitation

Cavitation is the creation of pockets of air or vapor within a liquid volume.

Cavitation often occurs when there is a drop in pressure below the liquid's vapor pressure causing it to change phase. Cavitation can occur in liquids that are either in motion or at rest. Pockets of cavitation can form both within the body of a liquid and on solid boundaries. Cavitation on a solid boundary is called fixed cavitation, and is of primary importance in the study of underwater vehicles. In supercavitating vehicles, the boundary geometry of the 'cavatator' at the nose causes flow separation from the solid wall. High velocity flow drops the pressure, and cavitation occurs within the separation region. These small cavities group together to form a larger cavity attached to the boundary. Without flow separation and this region of relative calm, any small cavities formed are unable to attach to the boundary and are convected away by the liquid flow [3-5].

If a stable flow is established, the cavity can either be maintained or expanded downstream of the injection site. Cavities which begin and end on the same solid boundary are called partial cavities. Cavities that end downstream of the boundary on which they begin are called supercavities. The artificial injection of more gas into an initial cavity in order to expand or maintain it is called ventilation. The role of the gas ventilation system in the context of supercavitating vehicles will be

discussed in the next section.

1.2.2 Supercavitating vehicles

A supercavitating vehicle is a high speed underwater vehicle that travels inside a stable gaseous supercavity. The elimination of friction with the water reduces the drag by up to 90% [6,7]. The supercavity is initiated by flow separation at the cavitator, which is a specialized name for the nose of these types of vehicles. The cavity is then expanded by ventilating more gas into the initial cavity [3,6,7]. The gas injection rate is carefully controlled to maintain cavity stability [8,9]. Under stable high speed conditions, the gas exhausts from the rear of the cavity by periodically shedding ring vortices with gaseous cores. At lower speeds, the supercavity resembles a plume and gas escapes through two trailing hollow vortex tubes formed by buoyancy induced bifurcation[3,10].

Supercavitating vehicles rely on high frequency acoustic sensors in the nose for navigation. Safe deployment of a supercavitating vehicle therefore requires that any interference from cavity self-noise be identified, quantified, and possibly eliminated [11-14]. The principal sources of self-noise are thought to be the gas-jet ventilation system and propulsive sources at the rear of the vehicle [1,2,15,16]. But sound from the propulsive system is confined primarily to lower frequencies. Also, sound from the rear of the vehicle is substantially attenuated by propagation over the pressure-release cavity surface [17]. Turbulence in the aqueous boundary layer at the edge of the cavitator generates sound and hydrodynamic pressure perturbations as it convects across the edge [13,15,18,19]. To analyze other sources of sound downstream of the cavitator, it is reasonable to treat the edge of the supercavity

as a pressure release surface. Then the sound generated by turbulence quadrupoles should contribute little to the overall sound, because the pressure release surface causes the pressure to vary as $\rho_w v^2 M^3$, where the Mach number $M = v/c_w \ll 1$, v representing flow velocity and ρ_w, c_w are respectively the mean density and sound speed in the water[20]. Ventilation noise sources include direct gas impingement on the cavity interface and the break-up of the interface into a roughened spray/bubble layer. These are potentially high frequency sources of sound characterized by instabilities with length scales smaller than the supercavity radius [11,12,15,16].

Foley *et al.* [2,6] used a specially designed supercavitating vehicle to investigate the radiated noise from cavity ventilation. In a typical design the ventilating gas is injected through a series of inlet nozzles and redirected with a deflection device so that the gas strikes the interface at a shallow angle, producing a relatively smooth interface (Figure 1.1). In Foley's experiments (at the Penn State Applied Research Laboratory (ARL)) the deflector was removed so that each jet impinged directly on the interface at close to normal incidence. Impingement at normal incidence at speeds between 40-50 m/s leads to the entrainment of gas bubbles (Figure 1.2).



Figure 1.1: Supercavitating vehicle in a water tunnel with a smooth cavity surface.



Figure 1.2: Supercavitating vehicle in a water tunnel with a rough and bubbly cavity surface.

It is important to consider the various paths of self noise to the acoustic sensors at the nose of the supercavitating vehicle. A popular design choice is to deflect

the gas jets to impact the interface at a shallow angle. A potential issue with this design choice is that it transmits vibrations directly through the structure towards the acoustic sensors at the nose (Figure 1.3). The total acoustic signal at the nose would be a combination of the vibrations transmitted through the structure and the signal that travels through the water. Supercavitating vehicles with deflectors tend to produce a more stable cavity, which is essential to the operation of these vehicles. As a result, it will be important to understand the interaction between gas jets and deflector plates.

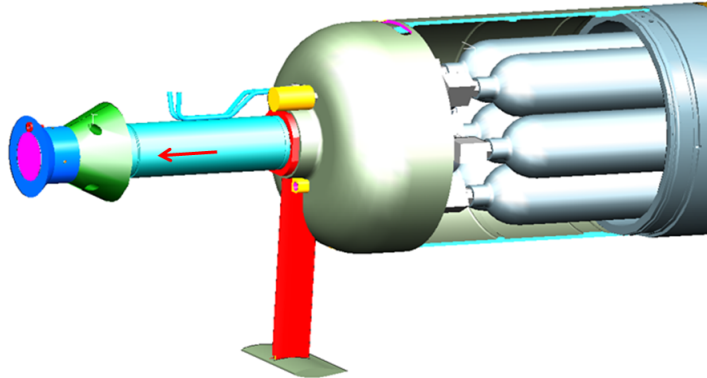


Figure 1.3: Acoustic paths of transmission for a supercavitating vehicle with a deflector.

1.2.3 Free gas jets impinging on plates

A review of existing literature showed that the dynamics of jet impingement are well explored. Many experimental and theoretical studies of impingement on both rigid and free surfaces have been made [21-23]. In these studies, the heat transfer

aspect of the jet impingement was a priority due to its application to manufacturing processes. The acoustics of a jet impinging on a plate have also been explored experimentally [24-26]. These studies focus on sound production mechanisms like shed vorticity and turbulence rather than the unsteady motion of a free surface. One experiment performed by Strong *et al* [27] is more relevant to the supercavitating problem because it measured the unsteady pressure generated by gas jets on a flat surface. Foley used Strong's measurements as a check for some of her experimental measurements [2]. A study of free jet velocities shows that over small length scales, the exit velocity of the jet at the nozzle is the same as the impact velocity of the jet on the interface [28]. As a result, experiments in this study were designed so that the jet exit velocity would be the same as its impact velocity.

1.2.4 Underwater Noise

The primary basis of this work is Foley's previous investigations into sound generated by the ventilation systems of supercavitating vehicles. Foley developed an acoustic model to predict the radiated sound a jet impinging on a smooth air-water interface. This model uses the measured unsteady force of a jet impinging on a rigid wall as an input. Search of the literature has shown that there have been no underwater measurements of gas jets impinging on an air-water interface. It therefore became a major goal of this investigation to take underwater acoustic measurements of gas jets impinging on an air-water interface. This would provide the first real chance to compare the acoustic model to real data. Foley et al [2] made measurements of the unsteady force spectrums of a gas jet impinging on a rigid wall. These measurements will be used as a basis of comparison for the force

measurements described in this thesis.

The theories described later in this thesis are an extension of Foley's original theory to account for the presence of bubbles. This led to considerable research into the acoustics of bubbly mixtures. Wood predicted that the frequency dependent sound speed in a bubbly mixture is dependent on the void fraction and resonant frequency of the bubbles in the mixture[29]. The resonant frequency of bubbles was shown to be a function of the radius by Minnaert[30]. Brennen provides an excellent overview of the acoustics of bubbly mixtures[6]. Sound in multi-phase flows are influenced by viscous and thermal diffusion [6,31]. The results of Wood and Minnaert are described in great detail, and provides a good discussion of the treatment of damping mechanisms, called η , in the frequency dependent sound speed equation. Fox *et al.* [32] performed experiments to measure the sound speed and attenuation through a bubbly fixture. They experimentally determined that a value of $\eta = 0.5$ matched their measurements. But analytical predictions of the attenuation for the experiments performed by Fox *et al.* [32] give a value of $\eta = 0.1$ [1]. While η is definitely dependent on the resonant frequency of the bubbles, it's exact value is still somewhat ambiguous.

While there have been no underwater measurements of gas jets hitting an air water interface, there have been underwater measurements of rainfall[33]. This is not the problem examined in this study, but the measured results could give some insight into noise spectrums generated by impacts at the surface. Pressure spectrums from this study show relatively flat broadband signals from 4-20 kHz. Studies have also been made of the collective oscillations of bubble clouds in salt water formed by a plunging water jet [34]. This paper highlights the importance of understanding bubble dynamics in a saltwater environment. Bubbles are profuse

in a saltwater environment, and sound interacting with clouds of bubbles can be a strong sound production mechanism [34]. For random noise generated by a gas jet hitting the interface, it seems reasonable to expect a relatively flat signal over that frequency range. Analytical studies have also been made to study the impact noise of a drop falling on water[35]. This model focuses on the impact of the drop on the interface as the main mechanism of sound transmission. The motivation for this study was to examine the effects of spray from impinging gas jets on the interface of a supercavity. These drops would likely fall back down to the interface and generate noise without bubble entrainment. Studies by Carey [36] on the acoustics of bubble plumes created by plunging water waves also provided insight into the acoustics of multiphase fluids. His discussion included a summary of Wood's result, and discussed the bubble cloud as an acoustic source. Carey's paper also described some fundamental differences between bubbles in fresh water and salt water. Bubbles in salt water tend to be smaller than those in fresh water because the ionic properties of the saltwater prevent bubble coalescence.

1.3 Approach

The first task in preparation for taking measurements related to sound generated by supercavitating vehicles was to design a surrogate gas injection system. The purpose of this system was to generate a steady jet of air while recording the flow data in order to calculate the jet exit velocity. After creating a reliable system for creating gas jets, this system was ready to be used in the other experiments planned in this study.

Analytical predictions coupled with experimental measurements have been

made to study the self noise from ventilated supercavitating vehicles. Foley's theory of sound generated through the air-water interface was extended to include the influence of a bubbly cloud formation. The final expression for radiated sound depends on empirical measurements of the unsteady force of the gas jet impinging on a rigid wall. Force measurements were taken at the Naval Undersea Warfare Center (NUWC) in Newport, RI on August 14-15, 2012. Gas jets of several different diameters were examined. The force measurements are used as an input to the theoretical radiated sound.

The sound of gas jets impinging on an air-water interface were recorded at the Acoustic Test Facility (ATF) at NUWC on August 20-21, 2012. The measurements were compared to Foley's original theory of sound generated through the air-water interface. Some of the gas jets were designed to entrain a cloud of bubbles beneath the surface. These results were compared to the predictions of sound generated through a bubbly cloud.

1.4 Outline

Measurements of the gas jet injection system are described in Chapter 2. The measurement of the unsteady force spectrum from gas jets impacting a rigid wall is discussed in Chapter 3. The acoustic measurements of gas jets impacting a planar air-water interface, and a bubbly air-water interface are discussed in Chapters 4 and 5. Chapter 6 describes in detail the calculation of sound radiated by a gas jet impingement on a gas-water interface. Chapter 7 summarizes the results of the previous chapters and provides suggestion for further research into the self noise of ventilated supercavitating vehicles.

Chapter 2

Measurements of the jet exit velocity and in air acoustic spectrum

This chapter discusses measurements of the gas jet injection system. Section 2.1 will describe the experimental setup and procedures. Section 2.2 will describe the data post-processing. This will include a description of the fluid dynamics theory used to calculate the jet exit velocities. Section 2.3 will present the results of the measurements. Section 2.4 will summarize the conclusions based on these measurements.

2.1 Experimental setup and procedure

In order to calculate the exit velocity of the gas jet at the nozzle, several measurements were taken of the gas flowing through the system. Pressure, temperature, and flow rate sensors were used to record p_1 , T_1 , and Q_1 respectively upstream of the jet nozzle (see Appendix C for sensor documentation). A sketch of the gas jet ventilation system is shown in Figure 2.1. The nitrogen gas is stored in a compressed bottle. Nitrogen gas was selected for this study because it is safe and easy to obtain. The pressure regulator controls the input pressure to the nitrogen gas, and is used to set the flow rate. The gas then travels 15' through a 1/4"

high pressure air hose until it reaches the sensors. The pipe diameter through the instrumentation section of the system is $1/2''$. The gas then travels another $5'$ until it reaches the jet nozzle. The instrumentation was located as close to the jet nozzle as possible. Four jet nozzles were used, with exit diameters of $1/16''$, $1/8''$, $3/16''$, and $0.355''$. The gas flow data was recorded using a *National Instruments* DAQPad attached to a PC running LabView software.

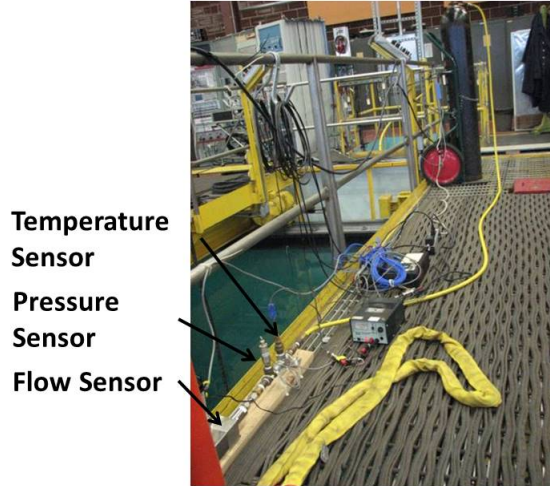


Figure 2.1: Gas jet ventilation system with pressure, temperature, and flow rate sensors. These sensors measure p_1 , T_1 , and Q_1 , respectively.

The gas jets were measured for flow rates attempting to match the desired exit velocities used in the acoustic measurements. The goal was to achieve jet exit velocities of 220 ft/s, 180 ft/s, and 140 ft/s. The flow rates chosen to get close to the goal velocities were based on incompressible flow theory. For incompressible flow, the exit velocity is the flow rate divided by the area of the exit nozzle. In addition to this, measurements were made for the $1/16''$ and $1/8''$ jet nozzles with the pressure set to 50 psi. These two high velocity tests were meant to calculate

the exit velocity for the jets that entrained a bubble cloud beneath the air-water interface.

In an effort to understand the noise of the gas jet ventilation system, in air recordings of the acoustic pressure spectrum were taken of the free jet. Nozzles with diameters $1/16''$, $1/8''$, $3/16''$, and $0.355''$ were again used for this measurement. Gas jets with exit velocities of 140 ft/s and 180 ft/s were recorded. The microphone was positioned $13/8''$ from the jet nozzle (see Appendix C for microphone documentation). This position was chosen to match the distance the gas jet would be set from the air-water interface in the acoustic experiments. The force spectrum data was sampled at a rate of 72 kHz using a *National Instruments* DAQPad and a PC running LabView software.

2.2 Data Analysis

2.2.1 Compressible gas flow theory

When a fluid moves at speeds comparable to the speed of sound, the flow is said to be *compressible*. One of the most important effects of compressibility is *choking*, where the flow rate is limited by the speed of sound, c . Compressible flow calculations depend on both the Mach number $M = V/c$, where V is the fluid velocity, and the specific heat ratio $\gamma = \frac{c_p}{c_v}$ [37]. For moderate changes in temperature, it is reasonable to use perfect gas assumptions with constant specific heats. This leads to the perfect gas law $p = \rho RT$, where p is pressure, ρ is density, R is the gas constant, and T is the temperature. The changes in enthalpy, h , can be calculated $dh = c_p dT$. The gas injection system used in ventilated supercavitating

vehicles can be modeled as an adiabatic isentropic gas flow.

The mass flux through the system is defined as $\dot{m} = \rho_E V_E A_E$, where ρ_E is the exit density, V_E is the exit velocity, and A_E is the area of the jet nozzle.

$$V_E = \frac{\dot{m}}{\rho_E A_E} \quad (2.2.1)$$

Assuming insentropic flow

$$\begin{aligned} \frac{\rho_E}{\rho_1} &= \left(\frac{p_E}{p_1} \right)^{1/\gamma} \\ \rho_E &= \rho_1 \left(\frac{p_E}{p_1} \right)^{1/\gamma} \end{aligned} \quad (2.2.2)$$

where p_1 is the measured pressure spectrum upstream of the nozzle, and p_E is the exit pressure at the nozzle. The exit pressure is assumed to be the same as atmospheric pressure. Substitute into (2.2.1)

$$V_E = \frac{\dot{m}}{\rho_1 A_E} \left(\frac{p_1}{p_E} \right)^{1/\gamma} \quad (2.2.3)$$

From Bernoulli

$$\frac{1}{2} V_1^2 = c_p (T_A - T_1) \quad (2.2.4)$$

where c_p is the specific heat of the gas, T_A is the ambient temperature, and T_1 is the measured temperature upstream of the nozzle. From the perfect gas law

$$\rho_1 = \frac{p_1}{R T_1} \quad (2.2.5)$$

Also the mass flux $\dot{m} = \rho_1 V_1 A_1 = \rho_1 Q_1$, where Q_1 is the measured volumetric flow rate upstream of the nozzle. Use (3.2.5) to obtain

$$T_1 = \frac{V_1 A p_1}{\dot{m} R} \quad (2.2.6)$$

Substitute this expression into (2.2.4)

$$\frac{1}{2} V_1^2 = c_p T_A - \frac{V_1 c_p A p_1}{\dot{m} R}$$

$$V_1^2 + \frac{2 V_1 c_p A p_1}{\dot{m} R} = 2 c_p T_A$$

Note that $c_p/R = \gamma/(\gamma - 1)$

$$V_1^2 + \frac{2 V_1 \gamma A p_1}{\dot{m} (\gamma - 1)} = 2 c_p T_A$$

$$\left(V_1 + \frac{\gamma A p_1}{\dot{m} (\gamma - 1)} \right)^2 = \left(\frac{\gamma A p_1}{\dot{m} (\gamma - 1)} \right)^2 + 2 c_p T_A$$

$$V_1 = \left[\left(\frac{\gamma A p_1}{\dot{m} (\gamma - 1)} \right)^2 + 2 c_p T_A \right]^{1/2} - \frac{\gamma A p_1}{\dot{m} (\gamma - 1)} \quad (2.2.7)$$

Using $\dot{m} = \rho_1 V_1 A$

$$\frac{\dot{m}}{\rho_1} = V_1 A = A \left[\left[\left(\frac{\gamma A p_1}{\dot{m} (\gamma - 1)} \right)^2 + 2 c_p T_A \right]^{1/2} - \frac{\gamma A p_1}{\dot{m} (\gamma - 1)} \right] \quad (2.2.8)$$

Substitute this into (2.2.3)

$$V_E = \frac{A}{A_E} \left(\frac{p_1}{p_E} \right)^{1/\gamma} \left[\left[\left(\frac{\gamma A p_1}{\dot{m} (\gamma - 1)} \right)^2 + 2 c_p T_A \right]^{1/2} - \frac{\gamma A p_1}{\dot{m} (\gamma - 1)} \right] \quad (2.2.9)$$

This theory works until the exit velocity of the jet gets close to the speed of sound. When this happens, the flow speed is determined by the critical pressures and densities of the gas in the system. The critical pressure is [37]

$$p_c = p_1 \left(\frac{2}{\gamma + 1} \right)^{\gamma/(\gamma-1)} \quad (2.2.10)$$

The critical density is [13]

$$\rho_c = \frac{\rho_1}{\left(\frac{p_1}{p_c} \right)^{1/\gamma}} \quad (2.2.11)$$

The velocity through the nozzle is then given by

$$V_c = \left(\frac{\gamma p_c}{\rho_c} \right)^{1/2} \quad (2.2.12)$$

2.2.2 Post-processing

The measurements p_1 , T_1 , and Q_1 were used to calculate the exit velocity of the gas jet from the nozzle. The first step in analyzing the data was adjusting the flow rate data to match the actual pressure and temperature conditions in the lab. The *Sierra Top-Trak* flow meter is calibrated to standard temperature ($T_{ST} = 70^{\circ}F$), and pressure ($p_{ST} = 1$ atm) conditions. The formula for this conversion is

$$Q_1 = \frac{p_{ST}}{p_1} \frac{T_1}{T_{ST}} Q_{ST} \quad (2.2.13)$$

Next use equation (2.2.5) to calculate ρ_1 . Next calculate the mass flux

$$\dot{m} = \rho_1 Q_1 \quad (2.2.14)$$

After the mass flux, \dot{m} , has been calculated, use equation (2.2.7) to calculate the velocity at the sensors, V_1 . Finally plug V_1 into Equation (2.2.9) to find the exit velocity at the nozzle, V_E . When the exit velocity at the nozzle gets close to the speed of sound, a different set of equations was used to calculate the exit velocity. This only occurs in the runs where the pressure at the regulator was set to 50 psi. In these cases, the flow is choked, and the exit velocity is determined by the critical pressures and densities of the gas. Equations (2.2.10-2.2.12) are used to calculate the choked flow exit velocity.

Some work needed to be done on the microphone time series data to calculate the power spectral density. The power spectral density of the voltage was calculated for the microphone using a Hanning window and $N = 2048$ Fourier transform points using the following formula

$$S = \frac{1}{LF} \frac{2T}{n_d N^2} \sum_{r=1}^{n_d} X X^* \quad (2.2.15)$$

where $LF = 0.375$ is the Hanning window loss factor, $N = 2048$ is the number of Fourier transform points, $n_d = 50$ is the number of averages, X is the Fourier transform of the windowed time series, and X^* is the complex conjugate of X . The time series used to calculate the power spectral density began 0.25 s after data acquisition began, and ended 1.1378 s later. A time series of this length ensures that 50 averages are used to calculate the power spectral density.

2.2.3 Uncertainty

The main source of error in the gas jet exit velocity is from the flow rate sensor (see Appendix C for documentation). The *Sierra Top-Trak* flowmeter has a $+/- 5\%$

error. It was also difficult to accurately set the pressure regulator for the low flow rates. In hindsight, a needle valve after the pressure regulator could have been used for finer control of the flow rates.

The only source of error for the in-air measurements was the microphone itself. The Brüel and Kjaer 4938 is accurate to $\pm 1\%$. During processing, the raw voltage is converted to decibels. Due to the logarithmic nature of decibels and the relatively small error from the microphone, it is customary to assume that the acoustic recordings are accurate to $+/- 1$ dB.

2.3 Results

2.3.1 Jet exit velocity measurements

Plots of the calculated gas jet exit velocities for the $1/16''$ nozzle are shown in Figures 2.2-2.4. It was difficult for the gas jet injection system to produce a steady exit velocity at these low flow rates. This is evident in the variability of the calculated exit speed.

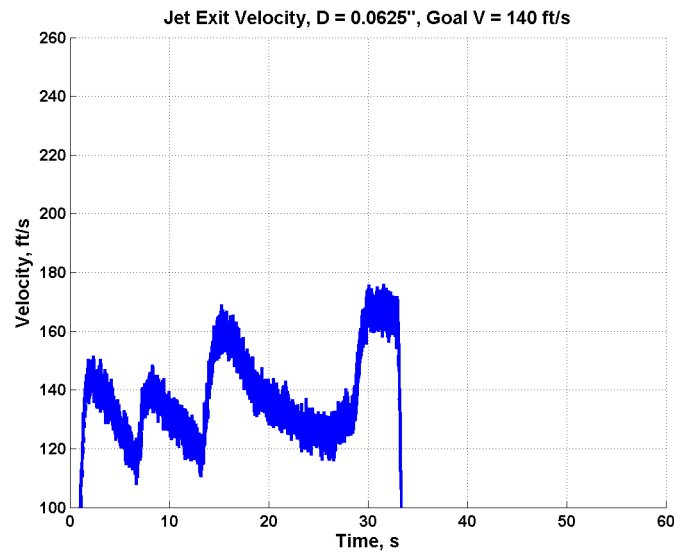


Figure 2.2: Gas jet exit velocity for the $1/16"$ nozzle with a goal velocity of 140 ft/s.

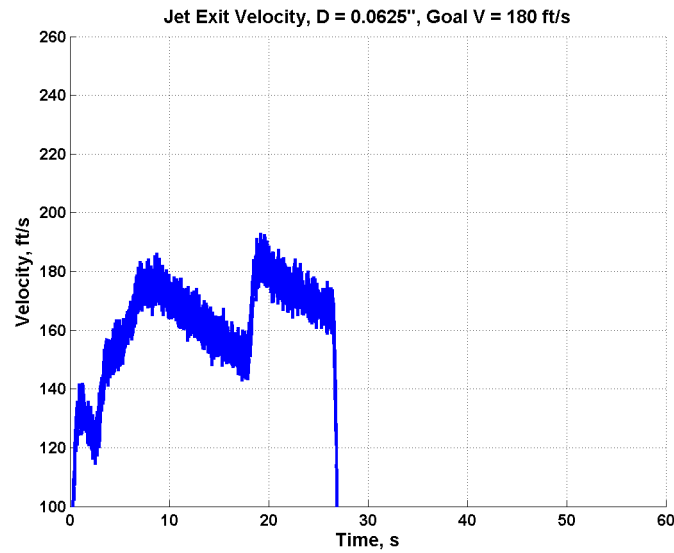


Figure 2.3: Gas jet exit velocity for the $1/16"$ nozzle with a goal velocity of 180 ft/s.

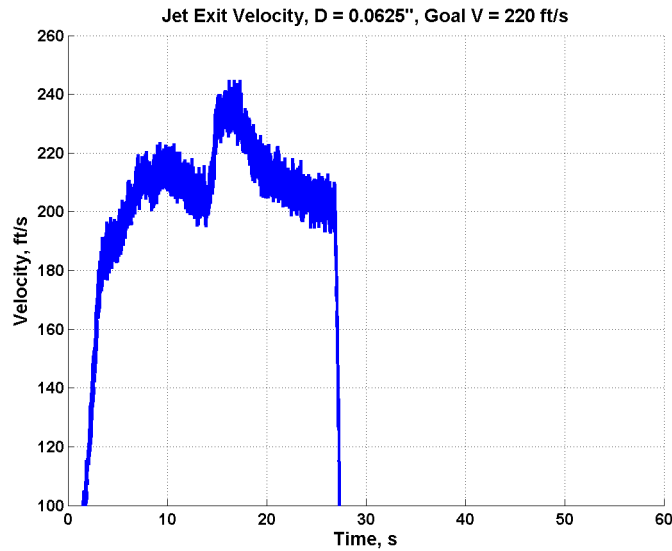


Figure 2.4: Gas jet exit velocity for the $1/16"$ nozzle with a goal velocity of 220 ft/s.

Plots of the calculated gas jet exit velocities for the $1/8"$ nozzle are shown in Figures 2.5-2.7. The gas jet system was better at controlling the higher flow rates. As the nozzle diameter and velocity increase, the calculated exit velocity gets smoother.

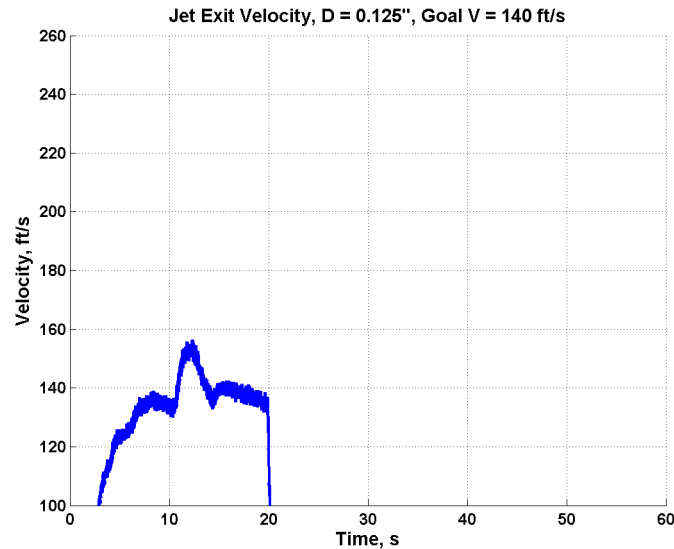


Figure 2.5: Gas jet exit velocity for the $1/8"$ nozzle with a goal velocity of 140 ft/s.

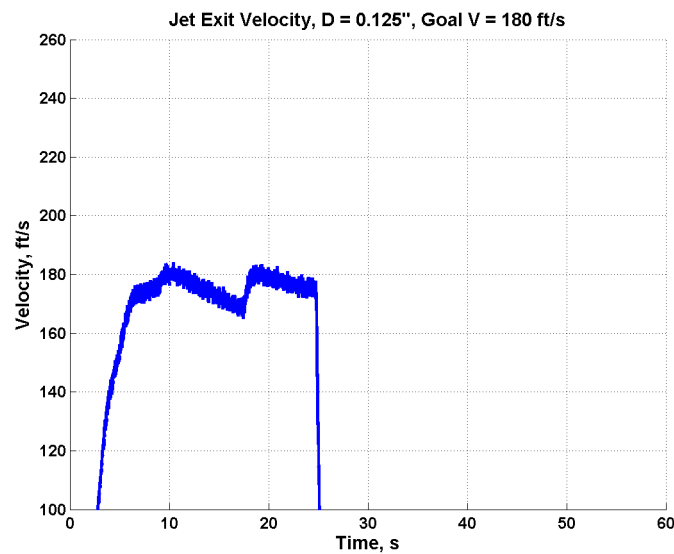


Figure 2.6: Gas jet exit velocity for the $1/8"$ nozzle with a goal velocity of 180 ft/s.

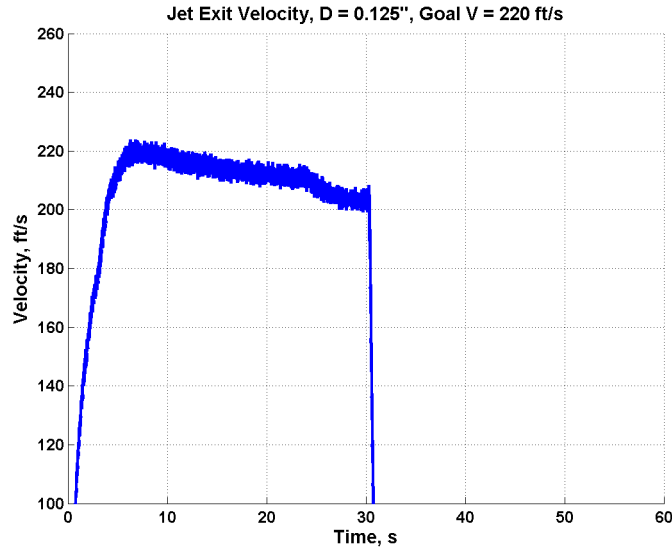


Figure 2.7: Gas jet exit velocity for the 1/8" nozzle with a goal velocity of 220 ft/s.

Plots of the calculated gas jet exit velocities for the 3/16" nozzle are shown in Figures 2.8-2.10. The gas jet system maintained a relatively steady flow rate for this nozzle. The calculated exit velocities were slightly below the goal velocities. The goal velocities were based on incompressible flow theory. The calculated exit velocities shows the difference between compressible and incompressible flow theory for this case.

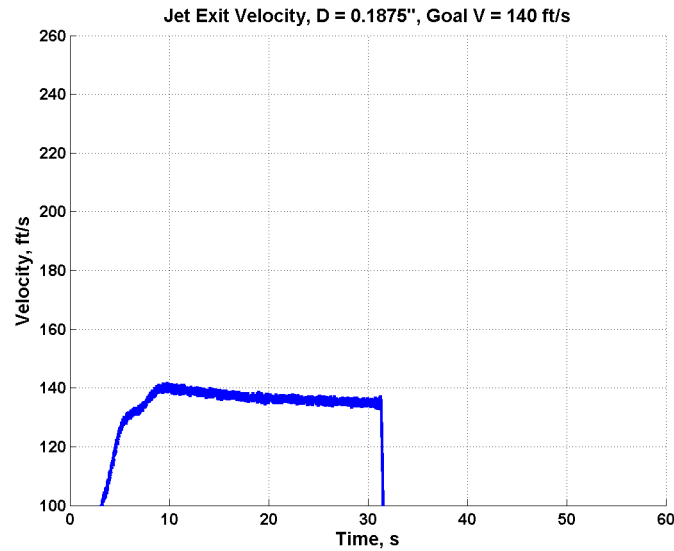


Figure 2.8: Gas jet exit velocity for the $3/16"$ nozzle with a goal velocity of 140 ft/s.

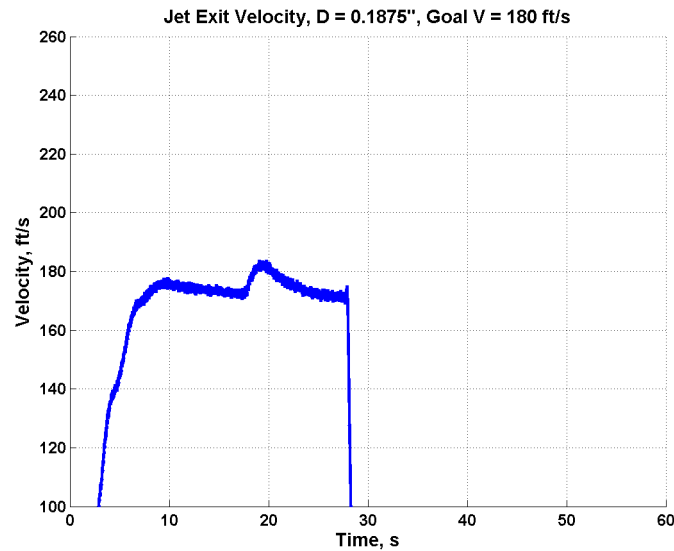


Figure 2.9: Gas jet exit velocity for the $3/16"$ nozzle with a goal velocity of 180 ft/s.

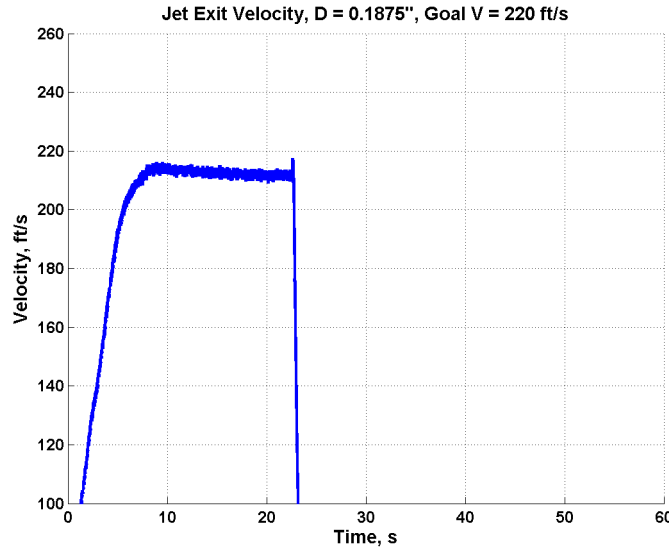


Figure 2.10: Gas jet exit velocity for the 3/16" nozzle with a goal velocity of 220 ft/s.

Plots of the calculated gas jet exit velocities for the 0.35" nozzle are shown in Figures 2.11-2.13. The gas jet system was able to maintain a steady flow rate for this nozzle. The calculated exit velocities were much lower than the goal velocities. The results from this nozzle indicate that there is a greater difference between compressible and incompressible flow theory when the nozzle size is increased.

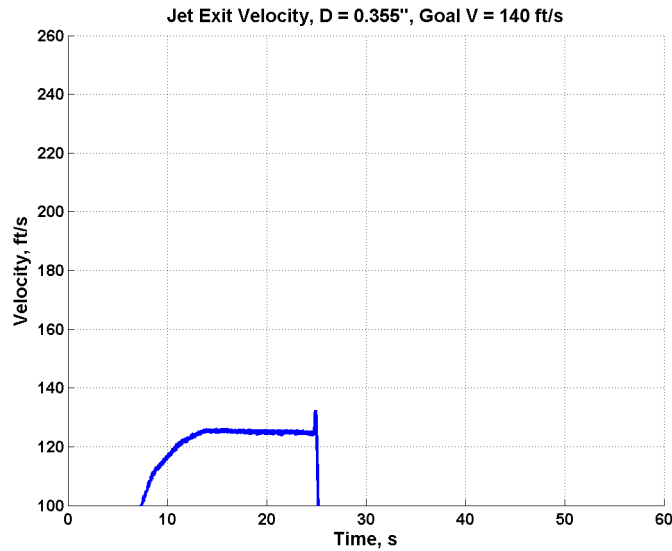


Figure 2.11: Gas jet exit velocity for the 0.355" nozzle with a goal velocity of 140 ft/s.

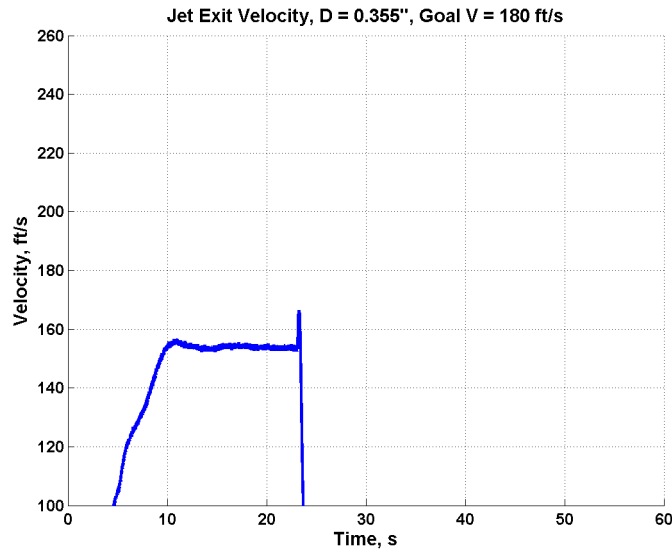


Figure 2.12: Gas jet exit velocity for the 0.355" nozzle with a goal velocity of 180 ft/s.

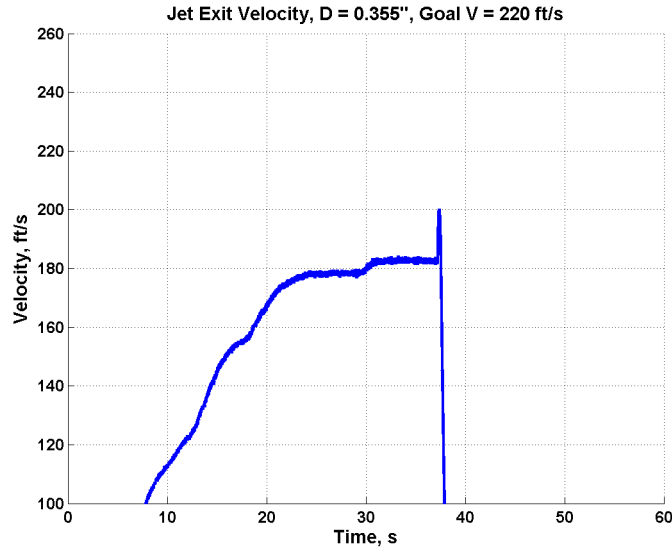


Figure 2.13: Gas jet exit velocity for the 0.355" nozzle with a goal velocity of 220 ft/s.

When the pressure regulator was set to 50 psi for the 1/16" and 1/8" nozzles, the jet exit velocity gets close to the speed of sound. The critical exit velocity is calculated using Equation 2.2.12. Plots of the critical velocity for the 1/16" nozzle are shown in Figure 3.14. For both nozzles the critical velocity was ≈ 1056 ft/s.

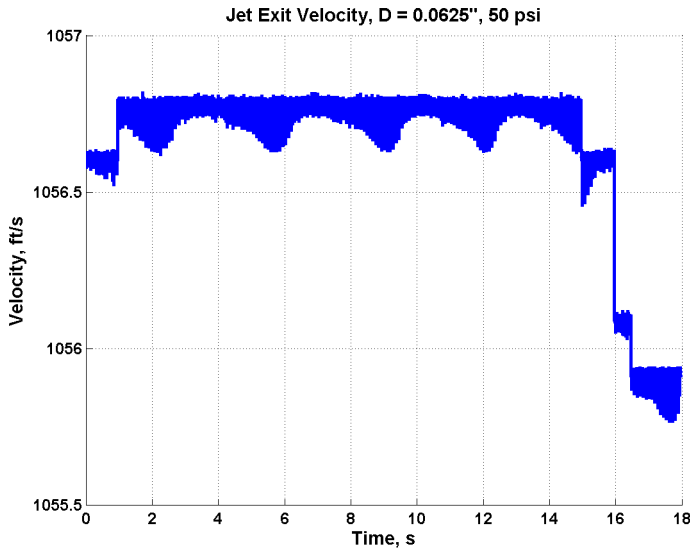


Figure 2.14: Gas jet exit velocity for the 1/16" nozzle with the pressure regulator set to 50 psi.

2.3.2 In air acoustic pressure spectrum measurements

The acoustic power spectrum for the 1/16" nozzle with an exit velocity of 180 ft/s is shown in Figure 2.15. The biggest spike in the spectrum occurs near 7 kHz. Some smaller peaks occur at around 16 and 24 kHz. The acoustic power spectrum for the 1/8" nozzle with an exit velocity of 180 ft/s is plotted in Figure 2.16. This spectrum also shows a spike near 7 kHz, but is otherwise mostly flat. The acoustic power spectrum for the 3/16" nozzle with an exit velocity of 180 ft/s is shown in Figure 2.17. This spectrum shows the same spike near 7 kHz. The acoustic power spectrum for the 0.355" nozzle with an exit velocity of 180 ft/s is shown in Figure 2.18. This spectrum appears quite different from the other nozzles. It has quite a few more spikes, including some large ones above 20 kHz.

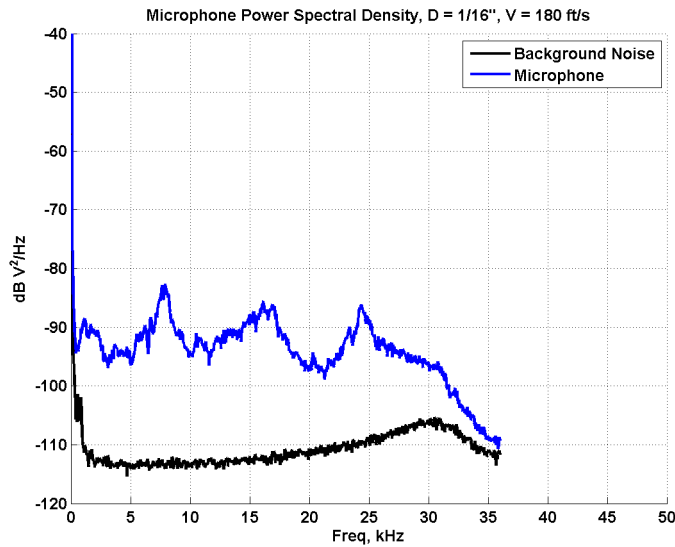


Figure 2.15: In air measurement of the free gas jet with a nozzle diameter of $1/16''$ and an exit velocity of 180 ft/s.

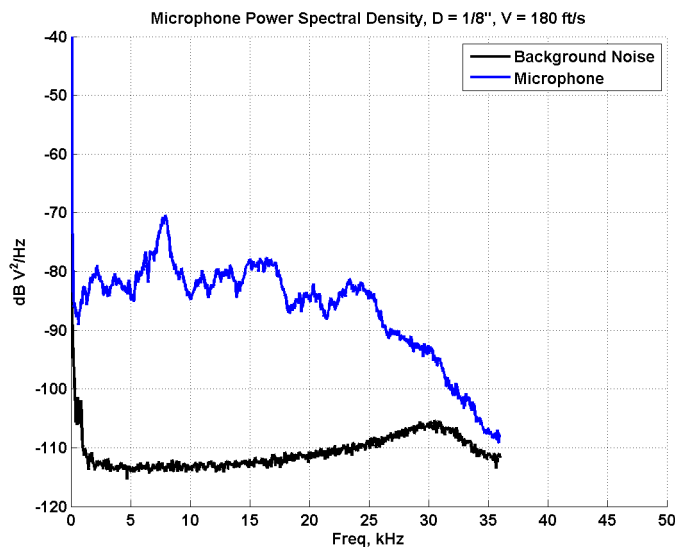


Figure 2.16: In air measurement of the free gas jet with a nozzle diameter of $1/8''$ and an exit velocity of 180 ft/s.

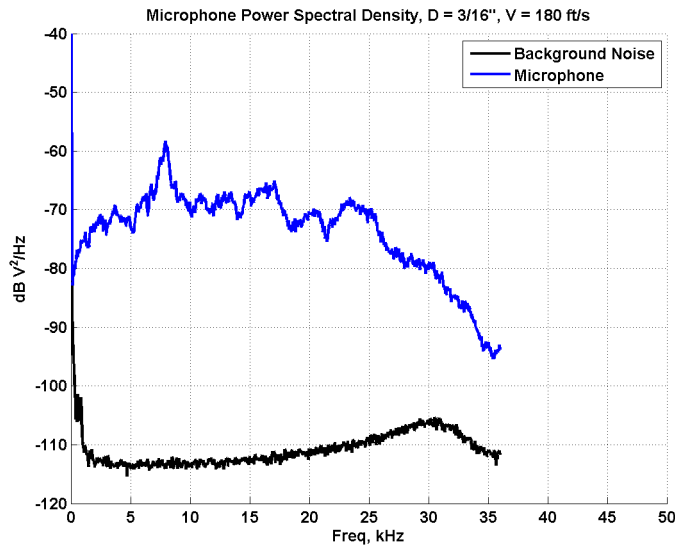


Figure 2.17: In air measurement of the free gas jet with a nozzle diameter of $3/16''$ and an exit velocity of 180 ft/s.

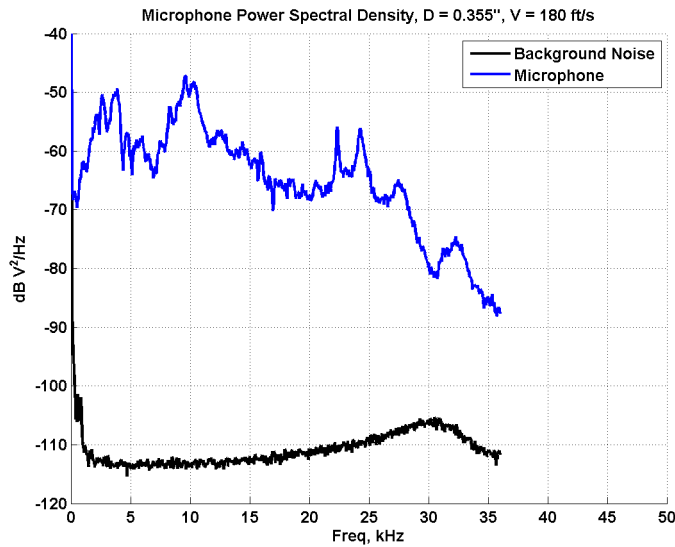


Figure 2.18: In air measurement of the free gas jet with a nozzle diameter of $0.355''$ and an exit velocity of 180 ft/s.

2.4 Conclusions

The measurements of the gas jet exit velocities are important in the analysis of the acoustic data. These velocities will be used to try and determine the relationship between jet exit velocity and radiated acoustic sound. The experimental measurements of the gas jet exit velocities from the gas injection system show that the exit velocity is not always steady. This is especially true at the lower flow rates used in the smaller nozzles.

The in air recordings of the acoustic spectrum of the free gas jet show that there are some tones generated by the jet injection system. Spectrum for the 1/16", 1/8", and 3/16" nozzles all show a spike at 7 kHz. This tone appears to be a characteristic feature of the gas jet injection system for these nozzles. This could be a result of irregularities in the flow through the system. An effort was made to keep the flow as smooth as possible within the system, but the attachment of the sensors to measure the flow rate created changes in the interior pipe diameter.

Chapter 3

Measurements of the unsteady force spectrum of a gas jet impacting a rigid wall

This chapter describes the force spectrum measurements performed at NUWC Newport, RI on August 14-15, 2012. Section 3.1 will describe the experimental setup, including the sensors used and data acquisition parameters. It also will outline the procedure used to collect the force spectrum data. Section 3.2 will describe the data post-processing, as well as the uncertainty of the measured data. Section 3.3 will present the recorded measurements, while section 3.4 will compare these results to the measurements previously made by Foley. Section 3.5 will highlight the important conclusions from this experiment.

3.1 Experimental setup and procedure

The force measurement experiments took place in an anechoic chamber located at NUWC. The chamber is designed to have as little background noise as possible, and is completely lined with sound dampening tiles to virtually eliminate reflected

noise. An array of force sensors was mounted to a massive rigid plate to record the unsteady force spectrum of the gas jet hitting a rigid wall. An array of 7 PCB Piezotronics force sensors was attached to 12" square steel plates as shown in Figures 3.1-3.3. A PCB Piezotronics accelerometer (see Appendix C for documentation) was attached to the steel plates to measure the vibrations of the entire structure. These steel plates were mounted to a translation table that could accurately position the rigid wall near the gas jet. The data from 6 of the force sensors and the accelerometer was acquired using a *National Instruments* DAQPad using Labview software at a sampling rate of 90 kHz. The force data was passed through a low pass filter set at 40 kHz, and then 20 dB of gain was applied to the signal.

Layout of Force Sensors

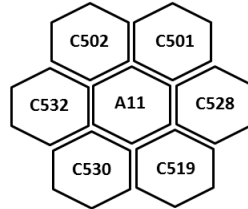


Figure 3.1: Layout of the force sensors on the steel plate.

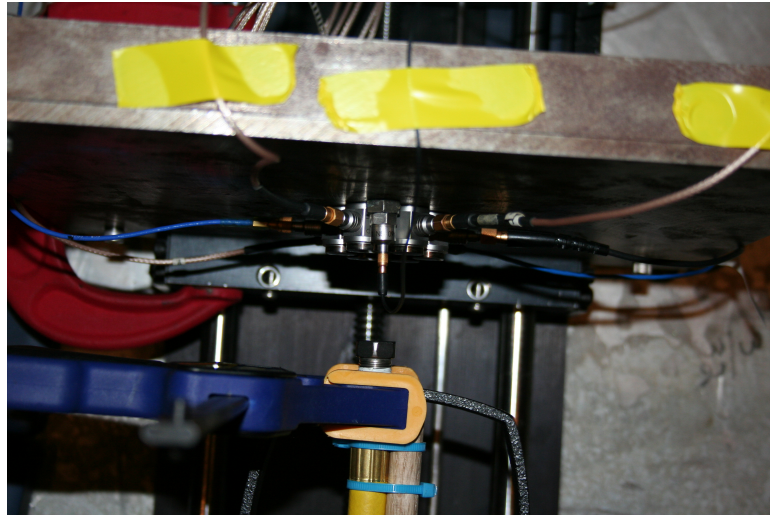


Figure 3.2: Top view of the force sensors and accelerometer.

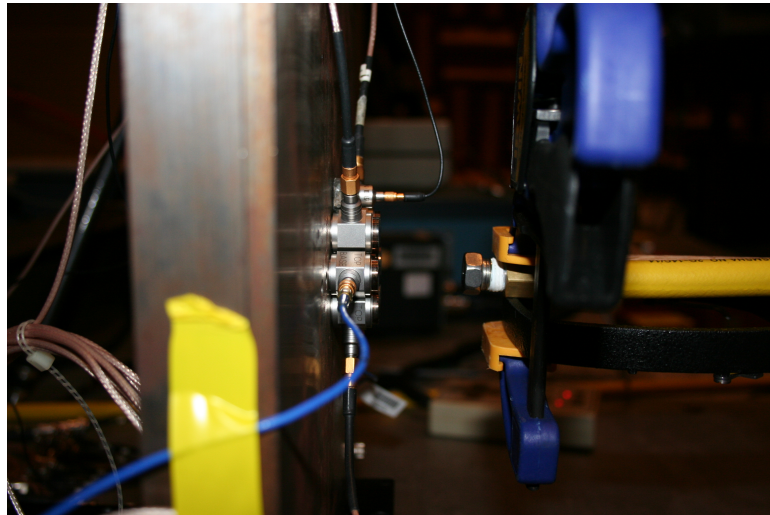


Figure 3.3: Side view of the force sensors and jet nozzle.

The model of the gas injection system investigated in these tests is a single jet of gas hitting a rigid wall at a normal angle. In order to create these conditions, a system was devised that could shoot the air jets at controllable and measurable velocities. The gas used in the tests came from a compressed Nitrogen bottle. Nitrogen was chosen for these experiments because of its stability. The flow rate

was controlled with a 0-250 psi pressure regulator. The flow rate was measured using a *Sierra Top-Trak* flowmeter (see Appendix C for documentation). A *National Instruments* DAQPad attached to a PC running Labview software acquired the data from the flowmeter.

After passing through the flowmeter, the gas flowed through a 1/4" air hose to detachable nozzles positioned next to the rigid wall. The diameters of the nozzles used in the tests were 1/16", 1/8", 3/16", and 0.355", and the nominal exit velocities investigated were 220 ft/s, 180 ft/s, and 140 ft/s. There were two additional runs using the 1/16" and 1/8" nozzles with the input pressure set to 50 psi. These were chosen to gather force spectrum measurements for the bubble entraining jets. The jet was positioned 1.375" from the force sensor array. Table 3.1 summarizes the test parameters.

Nozzle Diameter	Gas Jet Exit Velocities	Pressure Settings for Bubble Entrainment	Jet Distance from Interface
1/16"	140, 180, 220 fps	50 psi	1 3/8"
1/8"	140, 180, 220 fps	50 psi	1 3/8"
3/16"	140, 180, 220 fps		1 3/8"
0.355"	140, 180, 220 fps		1 3/8"

Table 3.1: Test matrix for the force measurement experiments.

The procedure for acquiring the test data was the same in each trial. First, the pressure regulator was adjusted until the flow rate meter displayed the appropriate reading to achieve the desired nominal exit velocity. This flow rate was calculated determine by an incompressible flow approximation and the nozzle exit diameter. For the cases where the input pressure was set to 50 psi, a shutoff valve in front of the flowmeter was closed. The regulator then set the system pressure to 50 psi, and the valve was reopened. After the gas was

flowing at the desired rate, the Labview software was used to begin the data acquisition. After 5 seconds, the data acquisition was stopped, and the gas flow turned off.

3.2 Data Analysis

3.2.1 Post processing

The power spectral density of the voltage was calculated for the force sensors and accelerometer using a Hanning window and $N = 2048$ Fourier transform points using the following formula

$$S = \frac{1}{LF} \frac{2T}{n_d N^2} \sum_{r=1}^{n_d} XX^* \quad (3.2.1)$$

where $LF = 0.375$ is the Hanning window loss factor, $N = 2048$ is the number of Fourier transform points, $n_d = 50$ is the number of averages, X is the Fourier transform of the windowed time series, and X^* is the complex conjugate of X . The time series used to calculate the power spectral density began 0.25 s after data acquisition began, and ended 1.1378 s later. A time series of this length ensures that 50 averages are used to calculate the power spectral density.

3.2.2 Uncertainty

The main source of inaccuracy in this measurement was the vibration of the entire plate structure. An accelerometer was attached to the plate to measure the vibrations. Another factor to consider is the potential changes in velocity inherent

in the gas jet system. The flow measurements indicate that the exit velocity is steadier at the higher flow rates. Finally, the force sensors themselves have a +/- 1% error (see Appendix C for documentation).

3.3 Results

The power spectral densities for the 1/16" diameter nozzle are shown in Figure 3.4. It was difficult to accurately adjust the pressure regulator to achieve the desired exit velocities for the 1/16" nozzle. For the 1/16" nozzle, the data hits the noise floor at 8 kHz. Figures 3.5-3.6 show the power spectral densities measured from the center sensor for the 1/8" and 3/16" nozzles respectively. The power spectral densities dip between 1-4 kHz, rise back up 3 dB, and then descend. Figure 3.7 shows the power spectral density measured from the center sensor for the .355" nozzle. The power spectral densities for the .355" nozzle do not have a local minimum between 1-4 kHz. Consistent features in the data are spikes at 15 kHz and 32 kHz. The spike at 32 kHz can be attributed to the natural resonance frequency of the force sensors (see Appendix C for sensor documentation).

Figure 3.8 plots the power spectral densities measured from all the force sensors as well as the accelerometer data for the 1/8" nozzle at 222 ft/s. The graph on the left is the force measurements. The blue curve corresponds to the A11 force sensor which was mounted in the center. The other curves represent the outer ring of sensors. The graph on the right is the power spectral density calculated from the accelerometer. A spike in the accelerometer data at 15 kHz indicates the entire structure was vibrating at this frequency. This could be related to the spike in force data at 15 kHz.

Figure 3.9 plots the power spectral densities measured from the full array of

force sensors and the accelerometer for the 1/16" nozzle with pressure set to 50 psi. The force power spectral density is relatively flat for the A11 sensor, with the exception of the resonant peak at 32 kHz. The outer force sensors have a spike between 7-8 kHz. The accelerometer shows that the entire structure is vibrating at frequencies greater than 7 kHz. Figure 3.10 plots the power spectral densities measured from the full array of force sensors and the accelerometer for the 1/8" nozzle with the pressure set to 50 psi. The force power spectral density is flat for the A11 sensor until 10 kHz, where it decreases by 6 dB and then flattens out again. The outer force sensors have a spike between 7-10 kHz. The accelerometer data for the 1/8" nozzle is similar to the data from the 1/16" nozzle with slightly higher amplitudes.

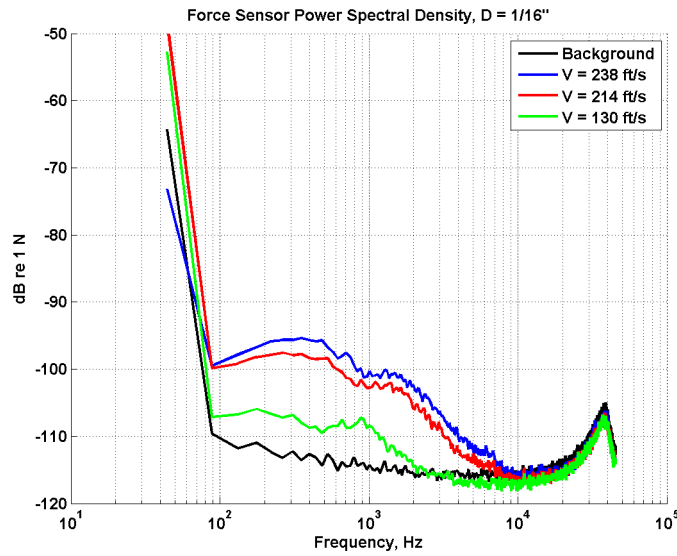


Figure 3.4: Power spectral density measurements of the force sensors for 1/16" jet diameter.

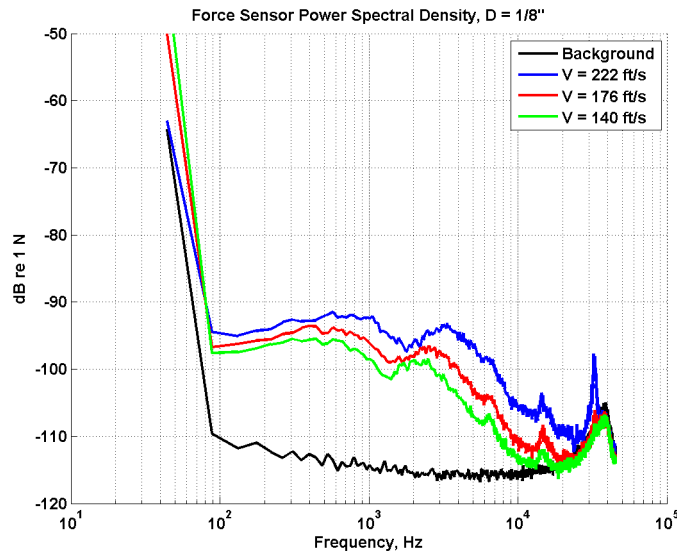


Figure 3.5: Power spectral density measurements of the force sensors for $1/8''$ jet diameter.

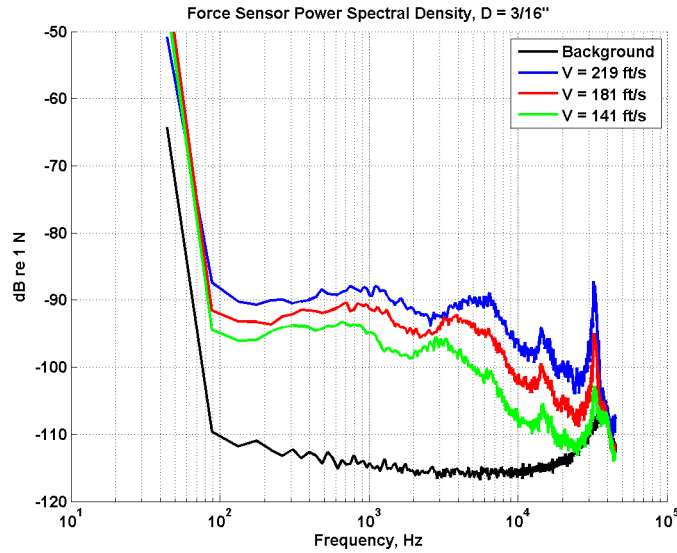


Figure 3.6: Power spectral density measurements of the force sensors for $3/16''$ jet diameter.

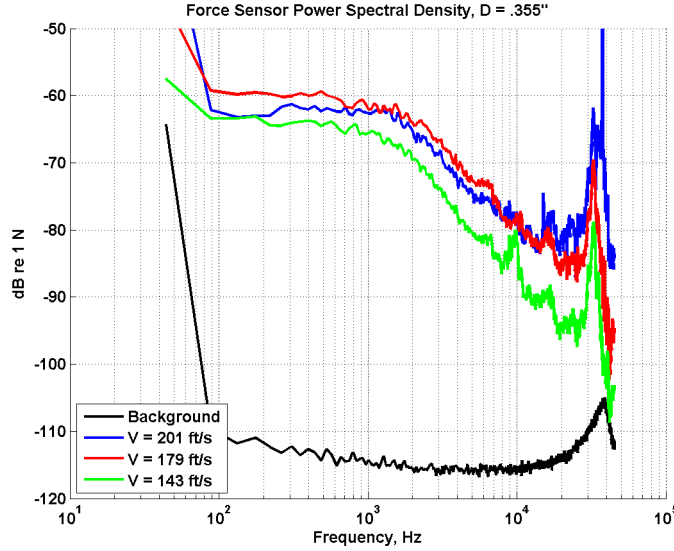


Figure 3.7: Power spectral density measurements of the force sensors for $0.355''$ jet diameter.

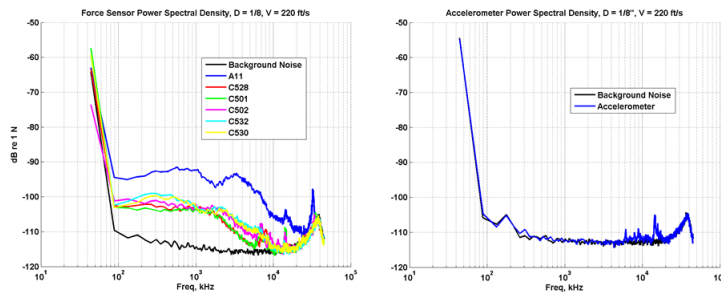


Figure 3.8: Force sensor power spectral density for the $1/8''$ diameter nozzle and exit velocity of 222 ft/s. The plot to the right is the accelerometer data from the same run.

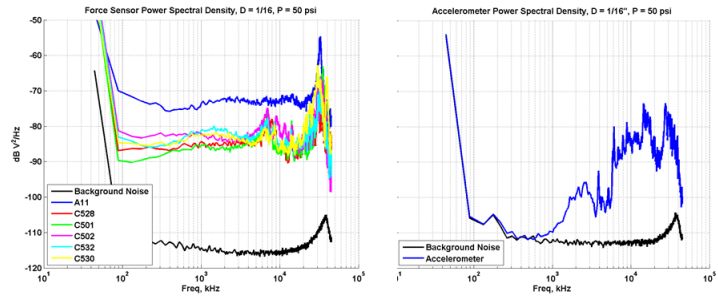


Figure 3.9: Force sensor power spectral density for the 1/16" diameter nozzle with the input pressure set to 50 psi. The plot to the right is the accelerometer data from the same run.

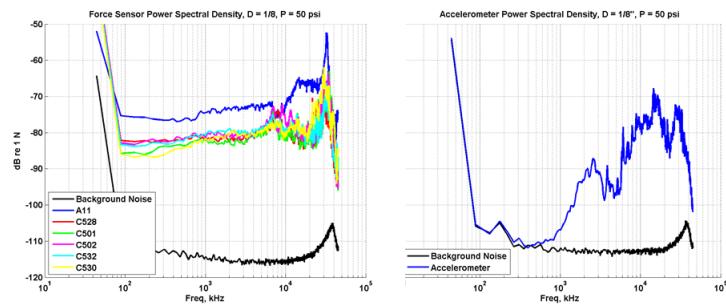


Figure 3.10: Force sensor power spectral density for the 1/8" diameter nozzle with the input pressure set to 50 psi. The plot to the right is the accelerometer data from the same run.

3.3.1 Comparison with Foley

Foley *et al* performed a similar set of measurements of the unsteady force of gas jets impinging on a rigid plate [1,2]. The difference in the two experiments was the gas jet injection system. Foley used a modified test vehicle to generate the gas jets[2]. This turned out to be a significant source of vibration that interfered with the measurement. The gas jet system used in this experiment used a system of high pressure hoses that could deliver a measurable amount of gas without unnecessary vibrations. Figure 3.11 plots a comparison of the measured unsteady force spectrum of the two experiments for a 1/8" nozzle with an exit velocity of 140 ft/s. Foley's data appears to be noisier between 3-10 kHz, and the measurements from this experiment show more of the sensor resonant spike at 32 kHz. Other than that the two measurements are similar. Figure 3.12 shows shows the comparison of the force spectrums for a 1/8" nozzle with an exit velocity of 180 ft/s. Foley's data appears to be much noisier between 3-20 kHz. But just before Foley's frequency jumps up, it lines up well with the measurements made in this experiment.

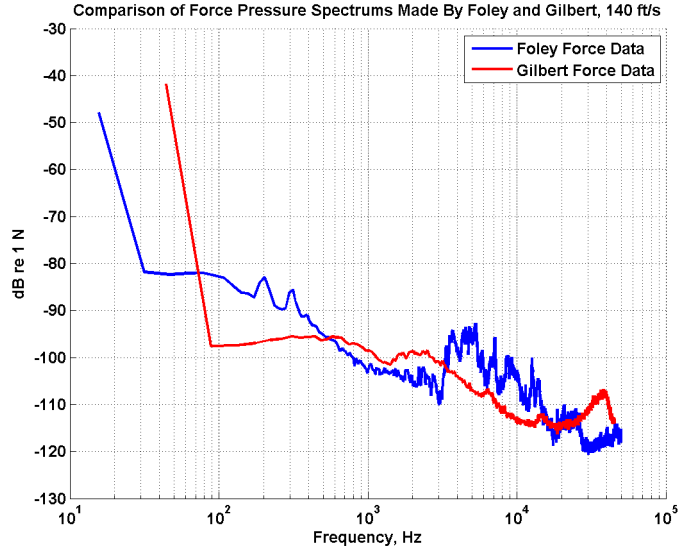


Figure 3.11: Comparison with the unsteady force measurements made by Foley for an 1/8" nozzle with an exit velocity of 140 ft/s.

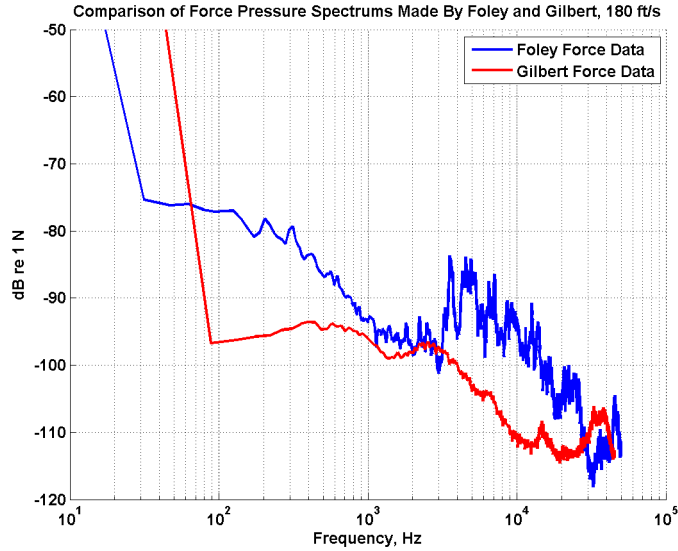


Figure 3.12: Comparison with the unsteady force measurements made by Foley for an 1/8" nozzle with an exit velocity of 180 ft/s.

Foley [1] estimated the form of $\Phi_{FF}(\omega)$ from measurements of the surface force spectrum produced by low speed jet impact on a nominally rigid wall. From these

measurements it was deduced that $\Phi_{FF}(\omega)$ is well approximated by the empirical formula

$$\frac{\Phi_{FF}(\omega)U}{F_o^2 D} = \frac{\alpha}{\left(1 + \epsilon^2(\omega D/U)^2\right)^{\frac{5}{4}}} \quad (3.3.1)$$

where α and $\epsilon \sim 1.6$ are constants. The value of α is adjusted to give the best fit to the measurements, and assumes a mean value of about 20 for Foley's [1] measurements. F_o is the nominal mean force exerted by the jet on the wall, and $F_o^2 = (\rho_A U^2)^2 (\frac{\pi}{4} D^2)^2$ where ρ_A is the mean gas density ($\sim 1.2 \text{ kg/m}^3$ in the experiments).

This empirical formula was compared to the measured force spectrums from this experiment for the $1/8''$ nozzle in order to be consistent with Foley's experiments. Figure 3.13 compares the normalized force pressure spectrum with the empirical curve fit for the $1/8''$ nozzle at an exit velocity of 220 ft/s. In this case the value of α was 60 and ϵ was 0.7. Figure 3.14 compares the normalized force pressure spectrum with the empirical curve fit for the $1/8''$ nozzle at an exit velocity of 180 ft/s. In this case the value of α was 60 and ϵ was 0.7. Figure 3.15 compares the normalized pressure spectrum with the empirical curve fit for the $1/8''$ nozzle at an exit velocity of 140 ft/s. In this case the value of α was 100 and ϵ was 0.5. The changing values of α and ϵ indicate that these parameters are dependent on the jet exit velocity.

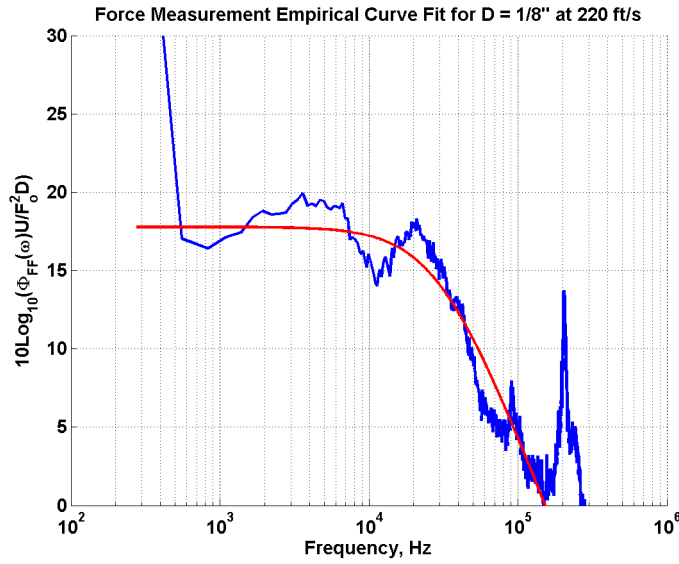


Figure 3.13: Comparison of the normalized unsteady force for the 1/8" nozzle at an exit velocity of 220 ft/s with the empirical curve fit from equation 3.3.1, $\alpha = 60$, $\epsilon = 0.7$

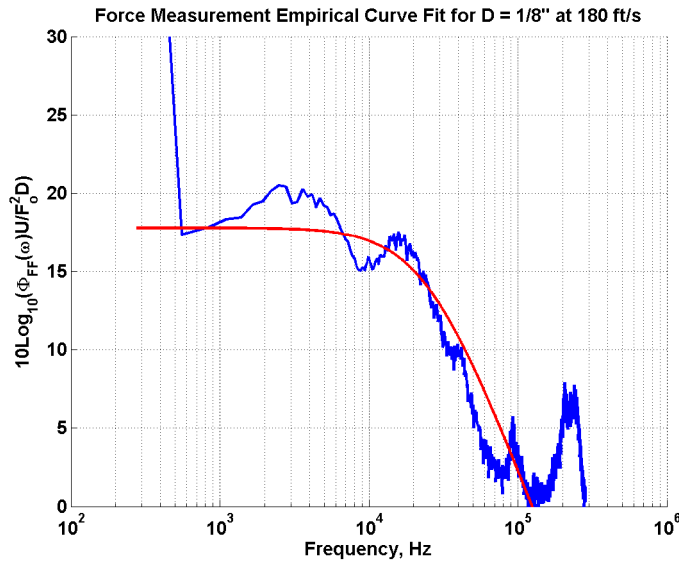


Figure 3.14: Comparison of the normalized unsteady force for the 1/8" nozzle at an exit velocity of 180 ft/s with the empirical curve fit from equation 3.3.1, $\alpha = 60$, $\epsilon = 0.7$

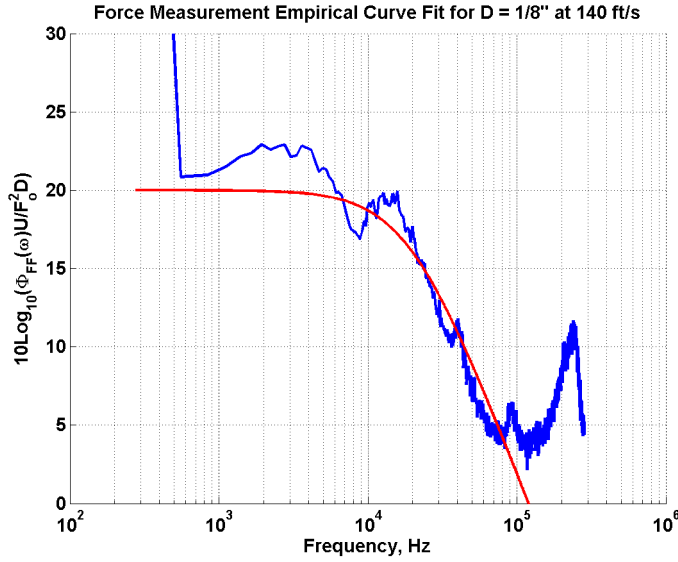


Figure 3.15: Comparison of the normalized unsteady force for the 1/8" nozzle at an exit velocity of 140 ft/s with the empirical curve fit from equation 3.3.1, $\alpha = 100$, $\epsilon = 0.7$

3.4 Conclusions

The analytical model for radiated acoustic noise depends on using an experimentally measured unsteady force spectrum as an input. Great care was made during the design of this experiment to eliminate unwanted noise due to vibrations. Comparisons with Foley's data show generally good agreement with less vibrational noise. The consistency between the two measurements is encouraging, and indicates that the unsteady force spectrum measured in this experiment should serve as a good input to the acoustic model.

Chapter 4

Acoustic measurements of gas jets impacting a planar air-water interface

This chapter involves the acoustic measurements of the underwater noise from gas jets impinging on the air-water interface. Section 4.1 describes the experimental setup and procedure for taking the measurements. Section 4.2 contains descriptions of the data analysis, including any post-processing, and a discussion of sources of uncertainty in the data. Section 4.3 presents the results in graphical format and discusses some of the trends in the data. Section 4.4 summarizes the important conclusions drawn from the experiments.

4.1 Experimental setup and procedures

Experiments were performed at the Acoustic Test Facility at NUWC to measure the noise generated by gas jets hitting the air-water interface Aug. 20-21 of 2012 at the Acoustic Test Facility (ATF) in NUWC Newport, RI. The ATF is a large indoor laboratory that specializes in accurate underwater sound recordings. The facility features a 700,000 gallon test tank, with dimensions of 60 ft. long, 40 ft. wide, and 35 ft. deep. Portions of the tank are lined with acoustic wedges to dampen out

reflections.

The gas ventilation system was positioned on a catwalk above the acoustic tank. The jet nozzle was attached to a lowering arm and positioned the jet 1.75" above the interface. A total of 4 hydrophones were positioned in the tank beneath the catwalk to record the underwater sound as shown in Figure 4.1. The primary hydrophone was oriented horizontally and positioned 3 m directly below the gas jet. Another 2 hydrophones were oriented vertically and positioned 1 m away from the jet and 1 m below the surface. The fourth hydrophone was again oriented horizontally and positioned 1 m away from the jet and 1 m below the surface. The orientation of the hydrophones is important because of the directivity of the hydrophones. The hydrophones are least sensitive in the direction towards the cable they are attached to. The fourth hydrophone was added so there would be two phones oriented in the same direction for comparison.

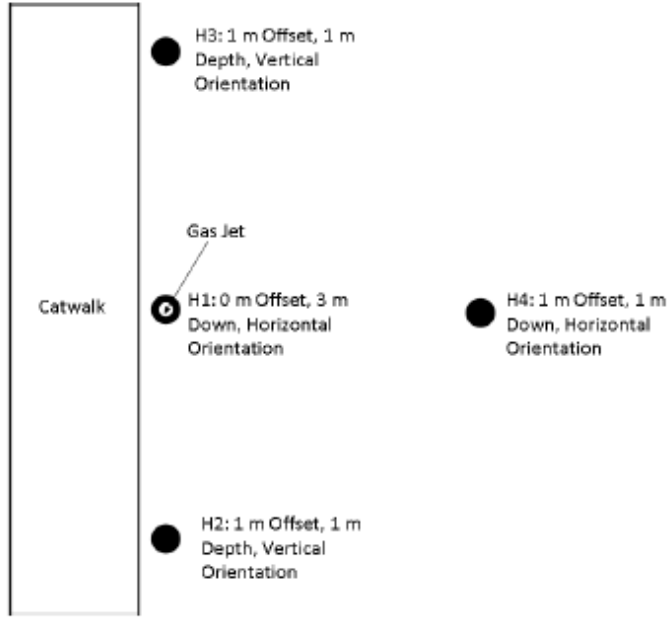


Figure 4.1: Hydrophone layout for acoustic experiments on Aug. 20-21 of 2012 at the ATF.

Data was acquired from the hydrophones with the data acquisition system at the ATF. The acoustic data was sampled at a rate of 150 kHz. The time series was then converted to a power spectrum using 16,384 points, and the final spectrum recorded was a result of 16 spectral averages. In this experiment, several jet diameters and jet velocities were examined. Jet diameters of $1/16''$, $1/8''$, $3/16''$ and $0.355''$ at exit velocities of 140 ft/s, 180 ft/s, and 220 ft/s were investigated. Table 4.2 summarizes the test matrix used in this experiment.

For each trial, the following procedure was used to acquire the data. First, recording of the gas instrumentation sensors was started in Labview. Then the gas flow was turned on, and the pressure regulator was adjusted to get the gas to the desired flow rate. This flow rate was estimated using incompressible flow theory,

Nozzle Diameter	Gas Jet Exit Velocities	Pressure Settings for Bubble Entrainment	Jet Distance from Interface
1/16"	140, 180, 220 fps	50 psi	1 3/8"
1/8"	140, 180, 220 fps	50 psi	1 3/8"
3/16"	140, 180, 220 fps		1 3/8"
0.355"	140, 180, 220 fps		1 3/8"

Table 4.1: Test matrix for acoustic measurements on Aug. 20-21 of 2012 at ATF.

along with the nozzle diameter and desired exit velocity. After the desired flow rate was achieved, the acoustic data acquisition system was started. After the system had performed the 16 spectral averages, gas flow was shut off, followed by the gas data acquisition system.

4.2 Data analysis

4.2.1 Post-processing

Data was acquired from the hydrophones with the data acquisition system at the ATF. The acoustic data was sampled at a rate of 150 kHz. The time series was then converted to a power spectrum using 16,384 points, and the final spectrum recorded was a result of 16 spectral averages. The data was then smoothed over frequency using a running average with a frequency window of 82 Hz and 90 percent overlap. Figure 4.2 shows the results of applying this filter to the data.

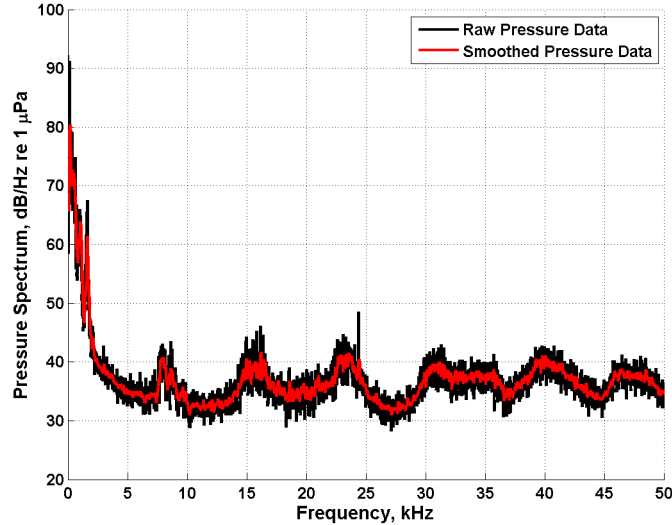


Figure 4.2: Comparisons of smoothed pressure frequency spectrum and raw pressure frequency spectrum data.

4.2.2 Uncertainty

The principal sources of uncertainty in this experiment are from the gas jet injection system. The measurements of the gas jet exit velocities shows that the exit velocity can fluctuate, especially at lower flow rates. This could impact the quality of data for the lower flow rates, especially the gas jets using the 1/16" nozzle.

Measurements of the in air pressure spectrum of the free jet shows that the system has a characteristic tone at 7 kHz for the 1/16", 1/8", and 3/16" nozzles. Individual bubbles could also potentially be contributing to the acoustic spectrum. Bubbles on the order of 100 microns could be present near the interface, undetectable by the naked eye. The only other source of error could be from the hydrophones. The acoustic data is converted to decibels, and due to their logarithmic nature the error is customarily marked as $+/- 1$ dB.

4.3 Results

Figures 4.3-4.6 show the smoothed sound pressure spectrum for all of the trials with no visible bubble entrainment. The data in Figure 4.3 shows very little variation in the sound pressure levels as a function of velocity for the 1/16" nozzle. The data in Figure 4.4 shows a dependence of the sound pressure level as a function of the velocity for the 1/8" jet nozzle. There also appear to be relative maxima near 16 and 23 kHz for this case. The data in Figure 4.5 shows variation between the runs at different velocities for the 3/16" jet. The spectrum also becomes pretty flat at the higher frequencies for this nozzle. The data in Figure 4.6 shows quite a bit of variation between the velocities for the 1/4" jet. For velocities above 168 ft/s a peak develops between 40-45 kHz. But when the jet velocity is reduced to 158 ft/s the peak vanishes.

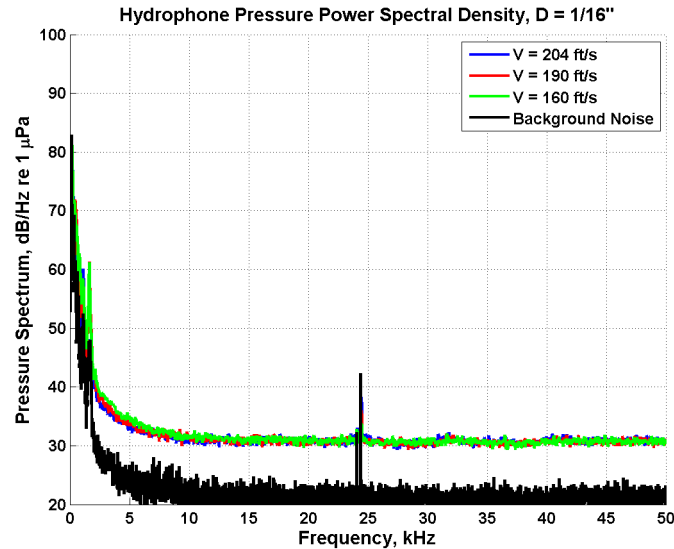


Figure 4.3: Measured acoustic pressure spectrums for the 1/16" nozzle jets.

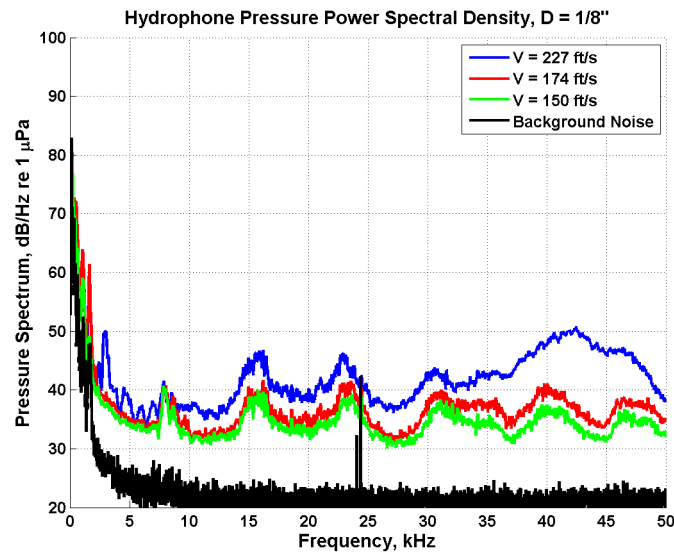


Figure 4.4: Measured acoustic pressure spectrums for the $1/8''$ nozzle jets.

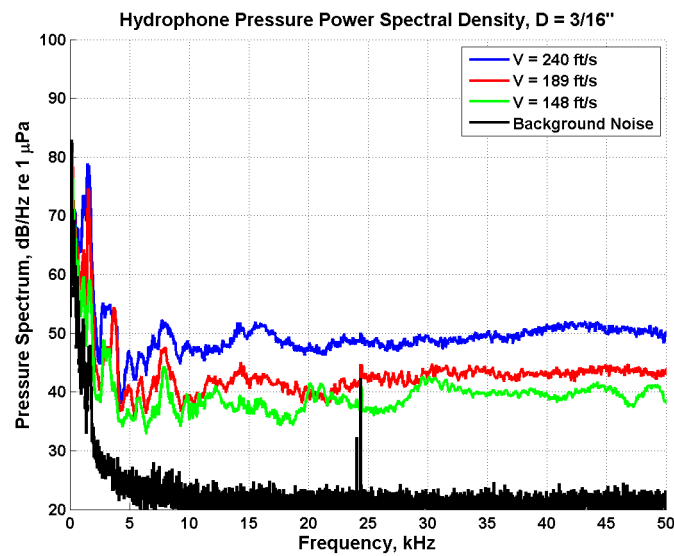


Figure 4.5: Measured acoustic pressure spectrums for the $3/16''$ nozzle jets.

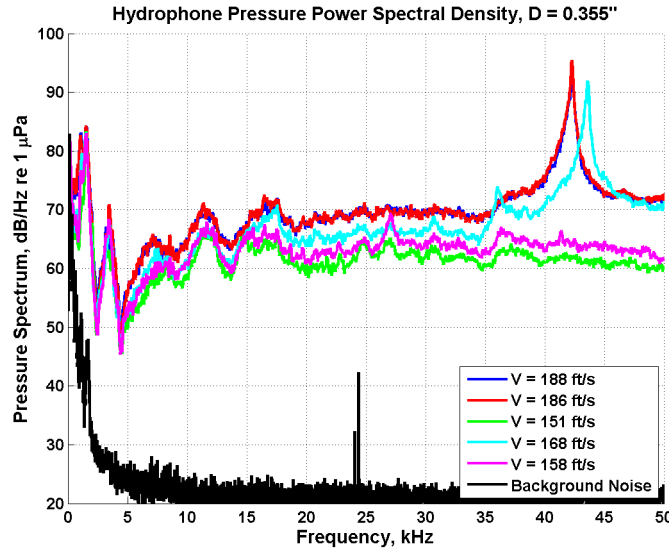


Figure 4.6: Measured acoustic pressure spectrums for the 0.355" nozzle jets.

Pictures were taken of gas jets impinging on the air-water interface in a small water tank. This tank would serve well for imaging purposes, but did not serve well as an acoustic tank. Pictures were taken of gas jets impinging on the air-water interface with nozzles of 1/16" and 1/8" with exit velocities of 140, 180, and 220 ft/s. The images were taken with a high speed camera sampling at a rate of 500 Hz.

Figure 4.7 shows the indentation created by a 1/16" nozzle jet with an exit velocity of 220 ft/s. In this picture the indentation is at a relative maximum, and penetrates about 3/8" below the surface. But the indentation is not fixed in time. Figure 4.8 shows another image from the same recording 5 frames later. In this picture the indentation has decreased in size. Figure 4.9 shows the indentation created by a 1/8" nozzle at an exit velocity of 220 ft/s. The indentation is at a maximum of about 1.25" in this picture. There are also several bubbles visible off to the side of the jet impact area. These are likely from water splashing back down onto the interface. The impact of the jet on the water surface sent some droplets

up into the air which then fell back onto the interface. Figure 4.10 shows another image of the $1/8''$ nozzle at 220 ft/s 8 frames after Figure 4.9. In this picture the indentation has shrunk down to a minimum of about $1''$.

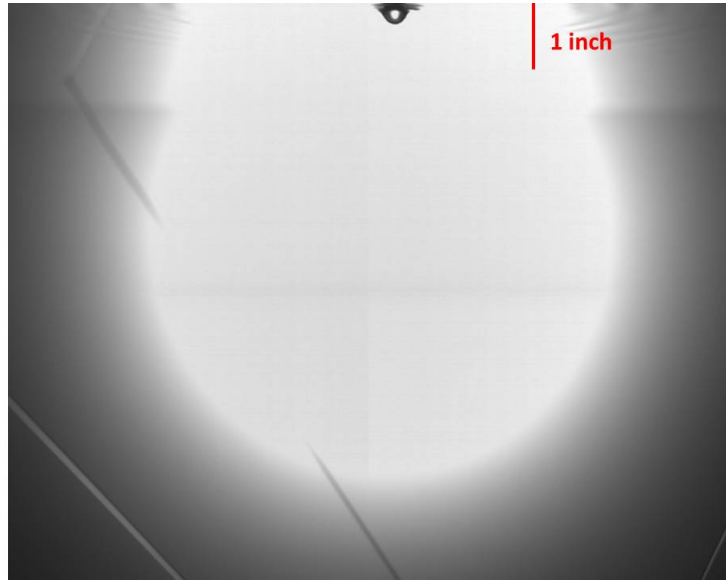


Figure 4.7: Picture of indentation created by a $1/16''$ nozzle jet with an exit velocity of 220 ft/s. The indentation is at a relative maximum of about $3/8''$.

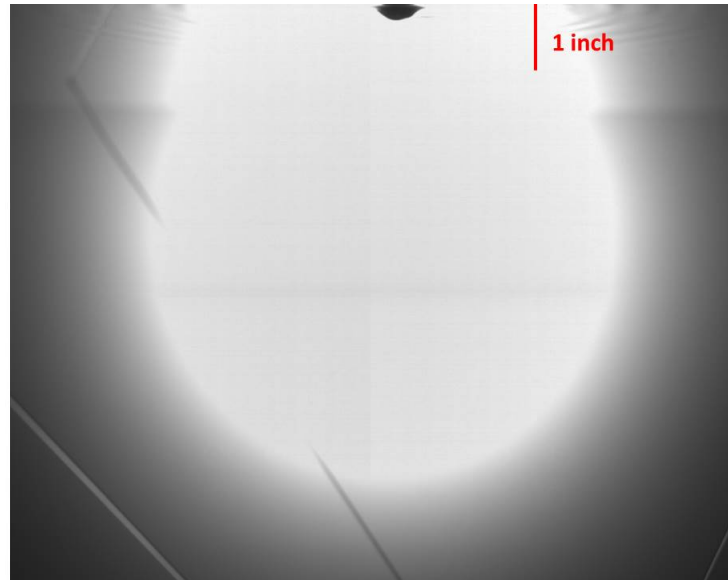


Figure 4.8: Picture of indentation created by a $1/16''$ nozzle jet with an exit velocity of 220 ft/s taken 5 frames after Figure 4.7. The indentation is at a relative minimum of about $1/4''$.

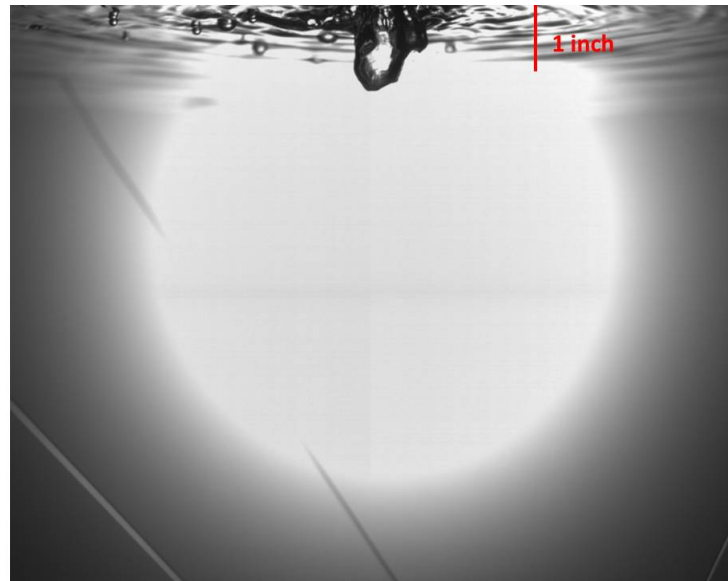


Figure 4.9: Picture of indentation created by a $1/8''$ nozzle jet with an exit velocity of 220 ft/s. The indentation is at a relative maximum of about $1.25''$.



Figure 4.10: Picture of indentation created by a $1/8''$ nozzle jet with an exit velocity of 220 ft/s taken 8 frames after Figure 4.9. The indentation is at a relative minimum of about $1''$.

4.3.1 Relationship between jet velocity and acoustic power

The data from the experiments has been plotted to check the dependence of the radiated sound on the jet velocity. Analytical predictions for a gas jet impinging on a water interface give a U^6 dependence between jet exit velocity and acoustic pressure spectrum in the water [1,2],

$$p_{acoustic}^2 \approx \rho_0^2 U^4 M^2 \quad (4.3.1)$$

where M is the jet Mach number relative to the sound speed in water. If we put $p = \alpha U^\beta$, then

$$20 \log_{10} p = 20 \log_{10} \alpha + \beta 20 \log_{10} U \quad (4.3.2)$$

Plotting the pressure spectrum as a function of the jet velocity on a logarithmic scale shows the slope β . A slope of $\beta = 3$ would correspond to a U^6 velocity dependence. Figure 4.11 is a plot of the average acoustic power spectrum vs the log of the velocity for the 1/16" nozzle. Unfortunately in this case, the acoustic power level does not show any dependence on the exit velocity of the gas jet. Figure 4.12 is a plot of the average acoustic power spectrum vs the log of the velocity for the 1/8" nozzle. The slope of this curve on a log scale is $\beta = 1.98$. Figure 4.13 is a plot of the average acoustic power spectrum vs the log of the velocity for the 3/16" nozzle. The slope of this curve on a log scale is $\beta = 2.55$. Figure 4.14 is a plot of the average acoustic power spectrum vs the log of the velocity for the 0.355" nozzle. The slope of this curve on a log scale is $\beta = 4.622$. It appears that there is a relation between the area of the jet nozzle and the associated power law for velocity. As the diameter of the jet nozzles increases, the slope of the fitted curves β increase.

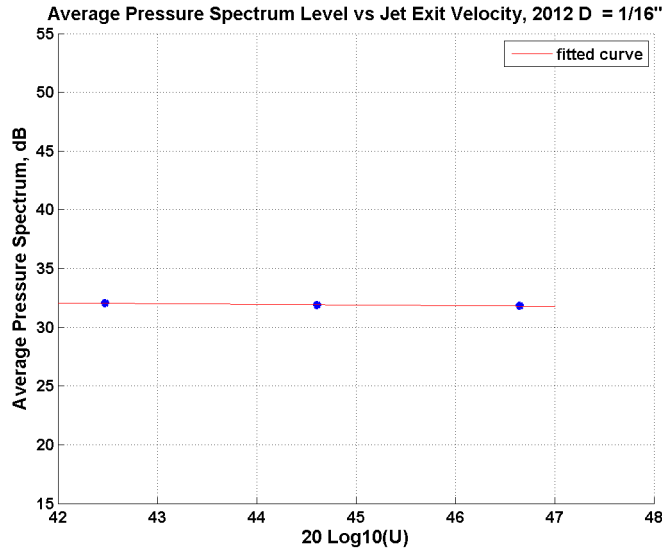


Figure 4.11: Average acoustic power spectrum vs the log of the velocity for the 1/16" nozzle. This plot shows no dependence on exit velocity.

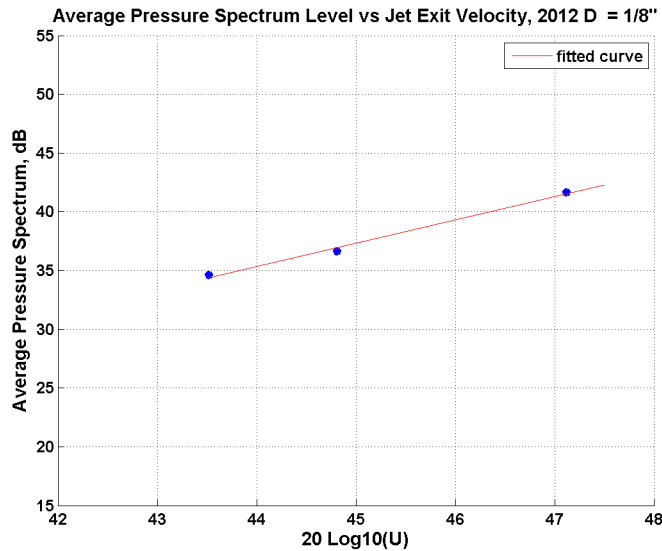


Figure 4.12: Average acoustic power spectrum vs the log of the velocity for the 1/8" nozzle. The slope of the data fit is $\beta = 1.98$.

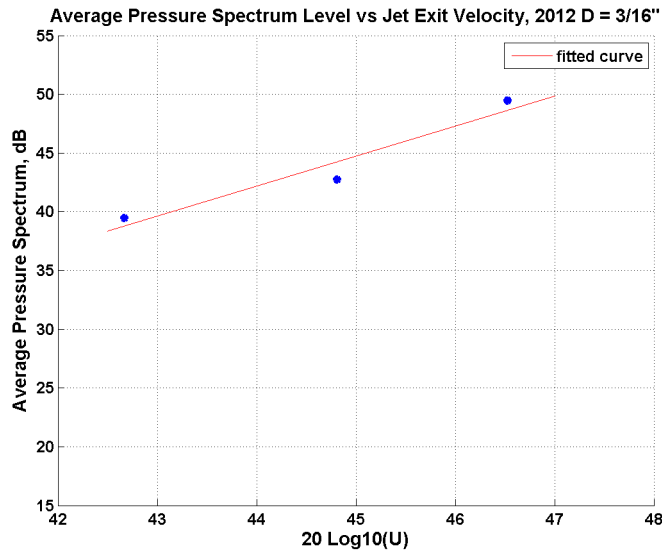


Figure 4.13: Average acoustic power spectrum vs the log of the velocity for the 3/16" nozzle. The slope of the data fit is $\beta = 2.55$.

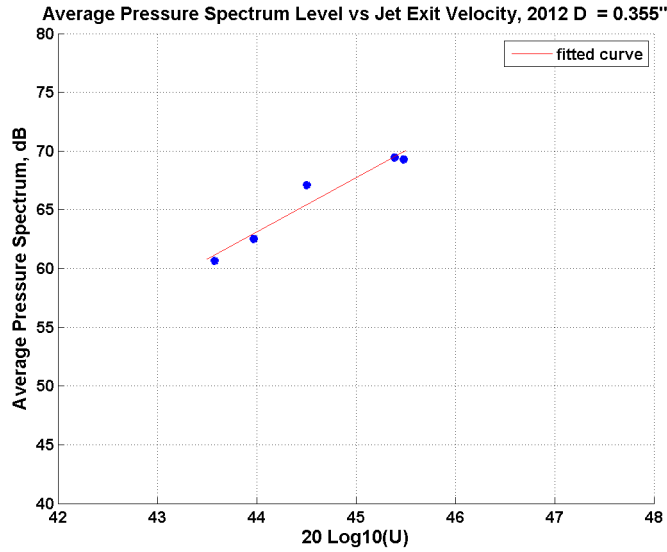


Figure 4.14: Average acoustic power spectrum vs the log of the velocity for the 0.355" nozzle. The slope of the data fit is $\beta = 4.622$.

Additional acoustic measurements were taken in August of 2013. These measurements were related to a deflector plate experiment that ended up being outside of the scope of this thesis. But for a couple of runs, the test setup was virtually identical to the measurements taken in 2012. The 3/16" nozzle was the only jet examined in 2013. The difference between these two experiments was that the nozzle was positioned 5.5" above the water. Figure 4.15 compares the data from 2012 and 2013 with an exit velocity of 140 ft/s. The spectrums shows some similar characteristics between the two measurements, especially the tone at 7 kHz. The overall power levels are considerably lower due to the increased distance of the jet from the air-water interface. Figure 4.16 compares the data from 2012 and 2013 with an exit velocity of 220 ft/s. Again, the spectra show similar features including the tone at 7 kHz.

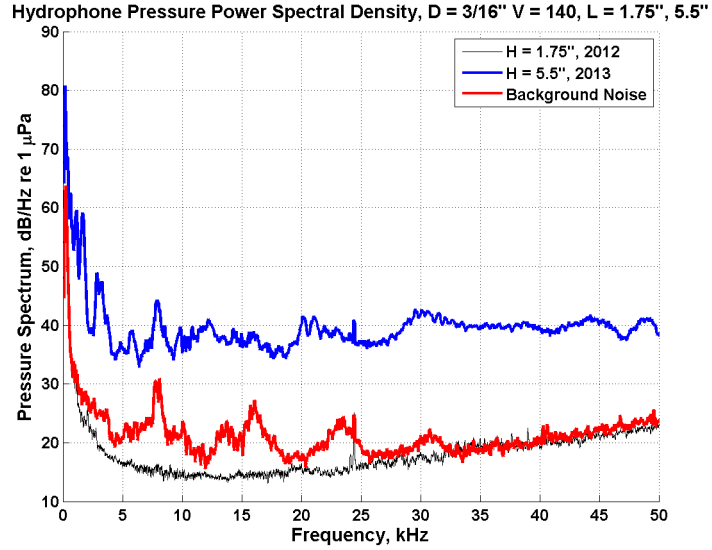


Figure 4.15: Comparison of measured acoustic spectra between 2012 and 2013 with jet exit velocities of 140 ft/s.

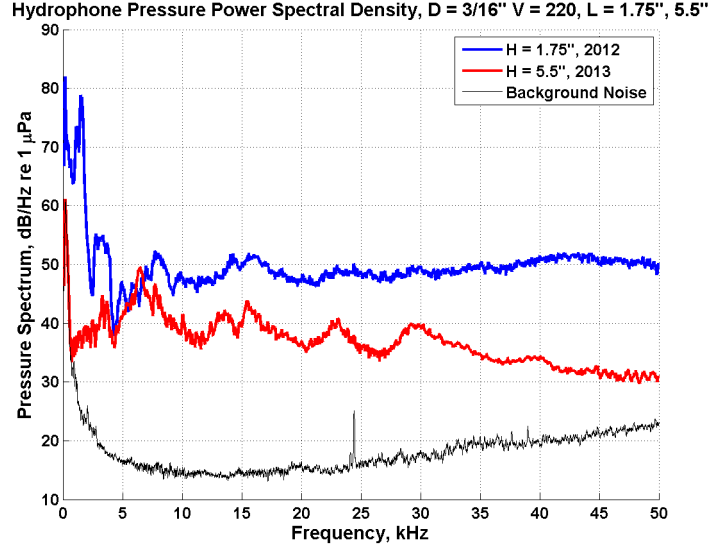


Figure 4.16: Comparison of measured acoustic spectra between 2012 and 2013 with jet exit velocities of 220 ft/s.

It looks like the power levels from 2013 increased more rapidly than the power levels in 2012 with an increase in velocity. To check this, the power law for the

2013 data is plotted in Figure 4.17. The slope of the curve fit for the 2013 data was $\beta = 3.45$. This is a bit higher than the power law predicted in 2012 for the same size nozzle. The longer jet length used in 2013 increases the impact area of the gas jet. This provides further evidence that the power law relation for velocity increases with an increase in jet impact area.

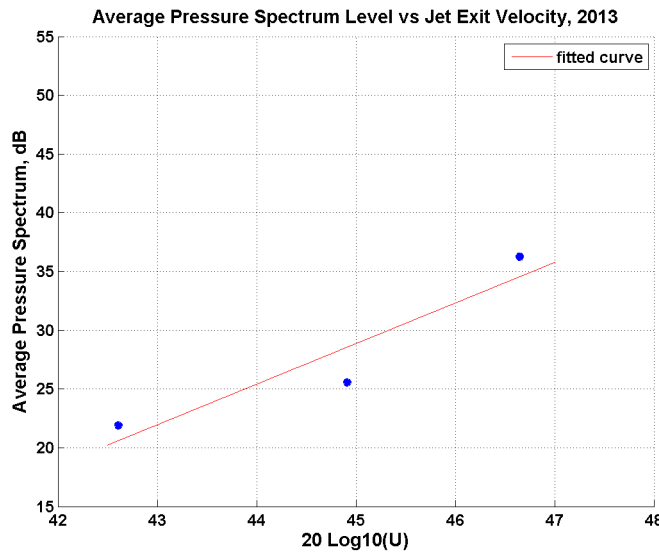


Figure 4.17: Average acoustic power spectrum vs the log of the velocity for the 3/16" nozzle taken in 2013. The slope of the data fit is $\beta = 3.45$.

The previous charts showed power law calculations using the average pressure level of the entire frequency range. In order to get an idea of what was happening in different bands of frequency, averages were taken of the pressure levels for specific ranges of frequencies. The low, middle, and high frequency bins averaged the spectrum pressure level between 2-7 kHz 7-20kHz, and 20-50 kHz respectively.

Figures 4.18-4.20 show the power law calculations for the 1/8" nozzle over the low, middle, and high frequency bins. For the 1/8" nozzle the low frequency bin calculated β was 1.04, the middle frequency calculated β was 1.44, and the high

frequency calculated β was 2.56. Figures 4.21-4.23 show the power law calculations for the $3/16''$ nozzle over the low, middle, and high frequency bins respectively. For the $3/16''$ nozzle the low frequency bin calculated β was 2.27, the middle frequency bin calculated β was 2.82, and the high frequency bin calculated β was 2.52. Figures 4.24-4.26 show the power law calculations for the $0.355''$ nozzle over the low, middle, and high frequency bins respectively. For the $0.355''$ nozzle the low frequency bin calculated β was 2.54, the middle frequency bin calculated β was 2.75, and the high frequency bin calculated β was 5.46. The power law calculations by frequency bin are similar to those calculated using the entire frequency range.

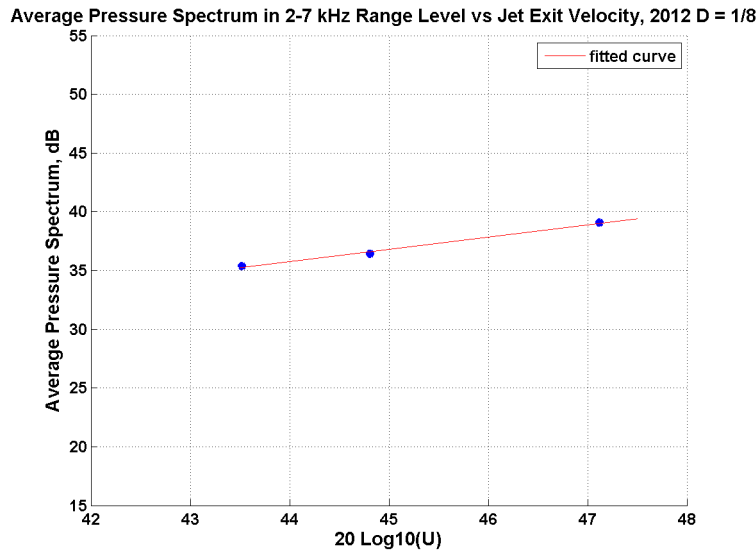


Figure 4.18: Average acoustic power spectrum between 2-7 kHz vs the log of the velocity for the $1/8''$ nozzle taken in 2012. The slope of the data fit is $\beta = 1.04$.

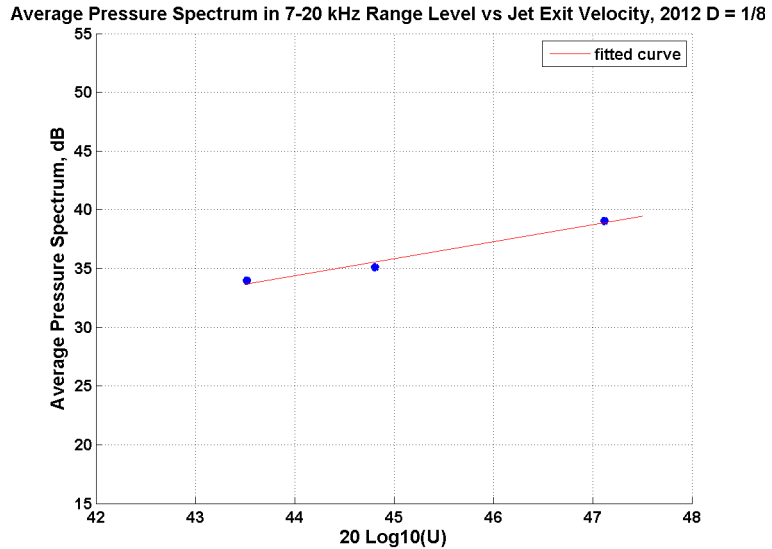


Figure 4.19: Average acoustic power spectrum between 7-20 kHz vs the log of the velocity for the 1/8" nozzle taken in 2012. The slope of the data fit is $\beta = 1.45$.

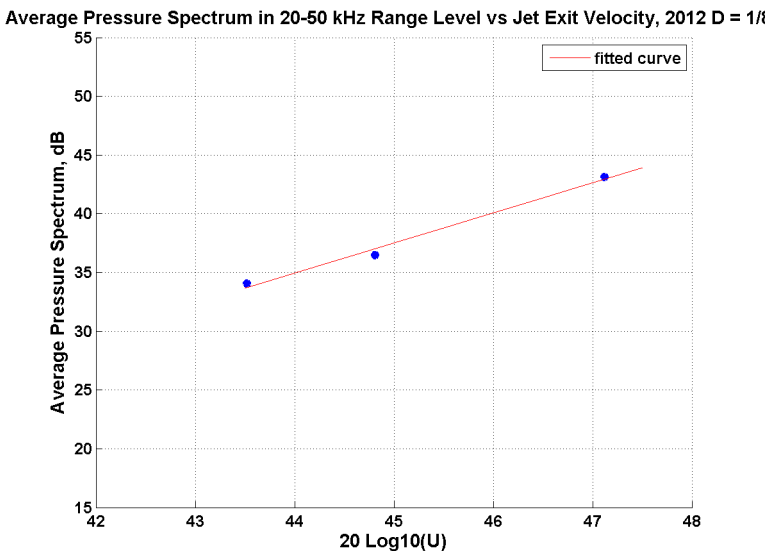


Figure 4.20: Average acoustic power spectrum between 20-50 kHz vs the log of the velocity for the 1/8" nozzle taken in 2012. The slope of the data fit is $\beta = 2.56$.

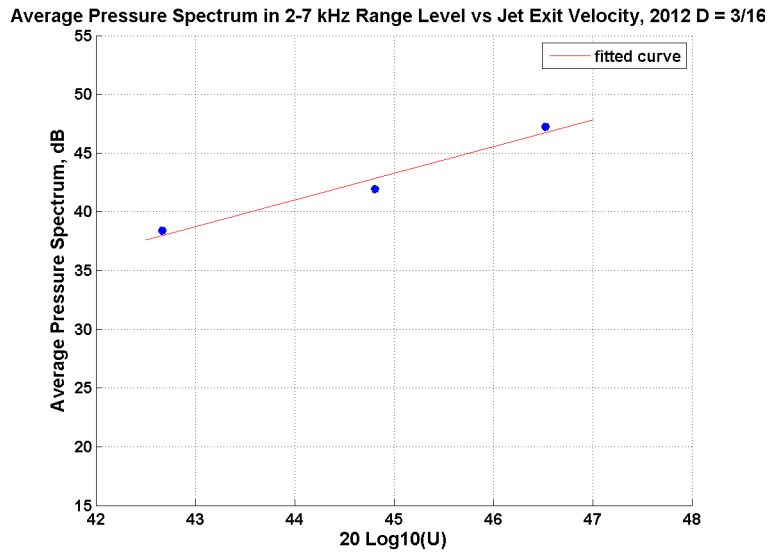


Figure 4.21: Average acoustic power spectrum between 2-7 kHz vs the log of the velocity for the 3/16" nozzle taken in 2012. The slope of the data fit is $\beta = 2.27$.

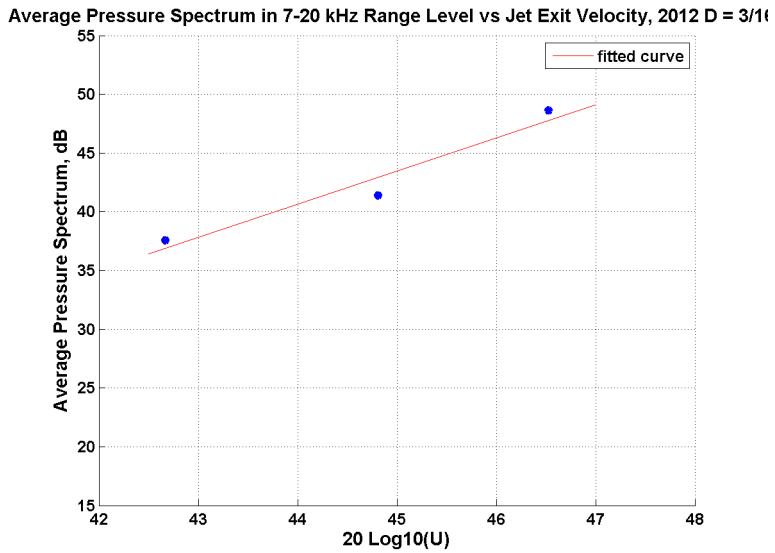


Figure 4.22: Average acoustic power spectrum between 7-20 kHz vs the log of the velocity for the 3/16" nozzle taken in 2012. The slope of the data fit is $\beta = 2.82$.

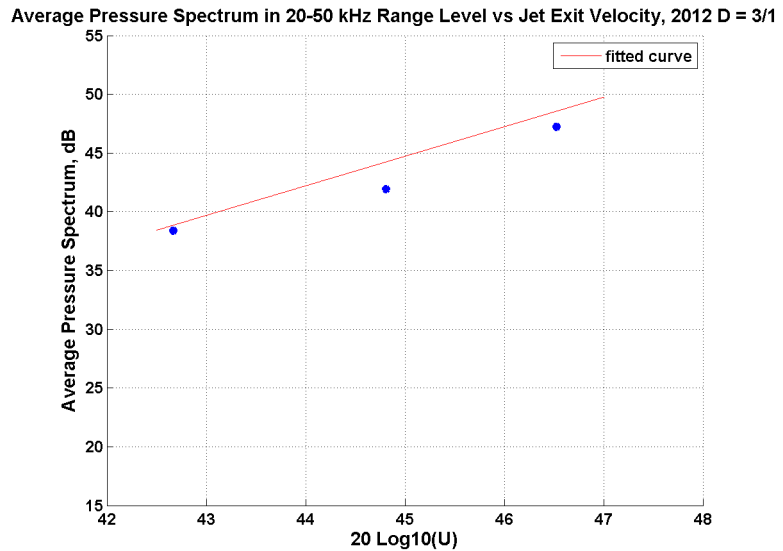


Figure 4.23: Average acoustic power spectrum between 20-50 kHz vs the log of the velocity for the 3/16" nozzle taken in 2012. The slope of the data fit is $\beta = 2.52$.

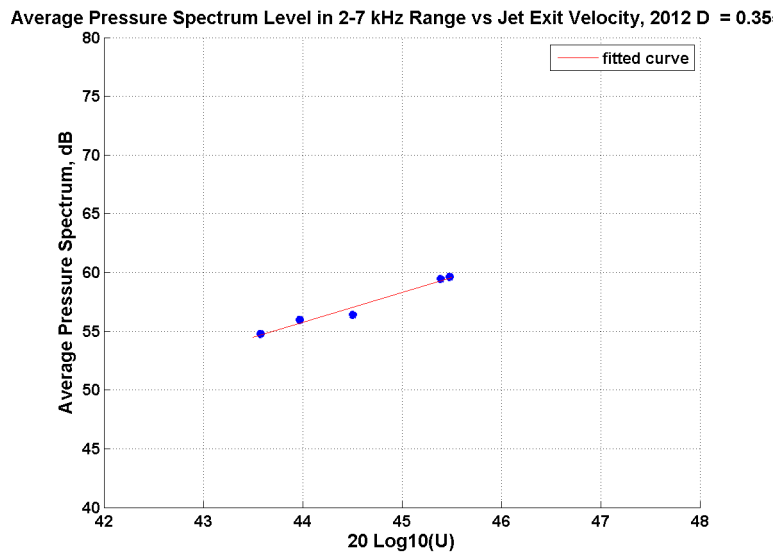


Figure 4.24: Average acoustic power spectrum between 2-7 kHz vs the log of the velocity for the 0.355" nozzle taken in 2012. The slope of the data fit is $\beta = 2.54$.

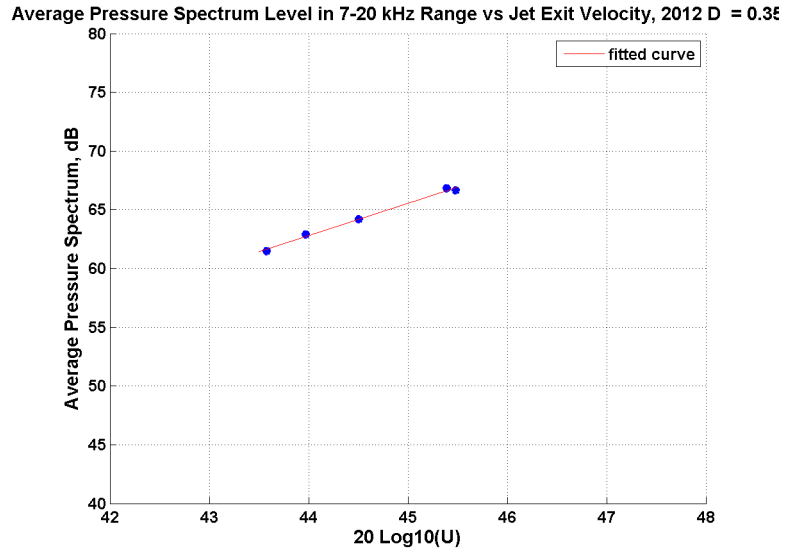


Figure 4.25: Average acoustic power spectrum between 7-20 kHz vs the log of the velocity for the 0.355" nozzle taken in 2012. The slope of the data fit is $\beta = 2.75$.

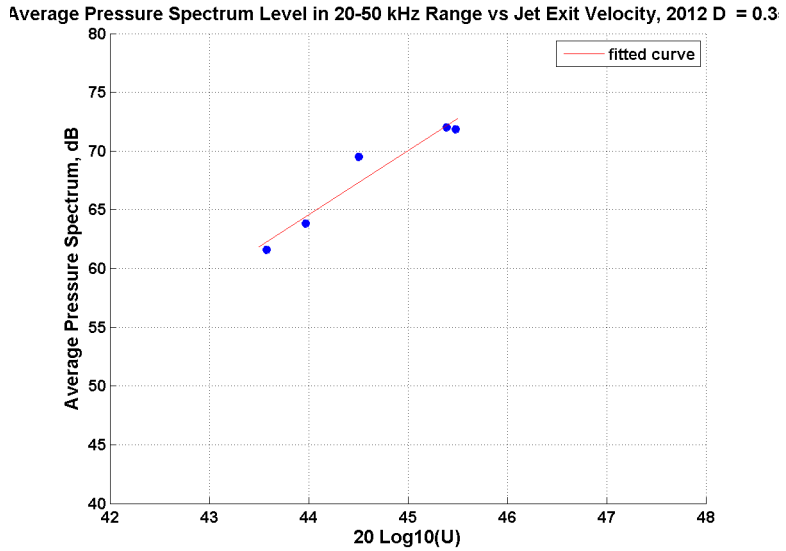


Figure 4.26: Average acoustic power spectrum between 20-50 kHz vs the log of the velocity for the 0.355" nozzle taken in 2012. The slope of the data fit is $\beta = 5.46$.

4.4 Conclusions

The recordings of the underwater acoustic pressure spectrums for various jets at different velocities provided additional insight into the radiated sound from supercavitating vehicles. The characteristic 7 kHz tone of the gas injection system was strong enough to radiate into the water. This indicates that it is vital to understand the in air sound produced by the ventilation system of a supercavitating vehicle.

The relationship between jet exit velocity and radiated sound was also explored. With the exception of the 1/16" nozzle, the measured power law relation was close to the U^6 relation predicted analytically. The power law relation for the gas jets also appeared to be related to the jet impact area. The levels of radiated sound from gas jets with larger impact areas change more rapidly than gas jets with smaller impact areas. This was particularly evident when comparing the data from 2012 and 2013. The only difference between the two experiments was the distance the nozzles were positioned above the air-water interface. The jet was positioned higher above the interface in 2013, which created a larger jet impact area at the surface. The power law related to exit velocity determined for the 2013 acoustic spectrum levels was higher than the data from 2012.

Chapter 5

Acoustic measurements of gas jets generating bubble entrainment at the air-water interface

This chapter involves the acoustic measurements of the underwater noise from gas jets impinging on the air-water interface with bubble entrainment. Section 5.1 describes the experimental setup and procedure for taking the measurements. Section 5.2 contains descriptions of the data analysis, including any post-processing, and a discussion of sources of uncertainty in the data. Section 5.3 presents the results in graphical format and discusses some of the trends in the data. Section 5.4 compares the measured data from the experiment to predicted sound levels from the analytical model of sound traveling through a bubble hemisphere. Section 5.5 summarizes the important conclusions drawn from the experiments.

5.1 Experimental setup and procedures

The setup and procedure for this measurement was very similar to the methods used to measure the underwater sound from the gas jets without bubble entrainment.

Experiments were performed at the Acoustic Test Facility at NUWC to measure the noise generated by gas jets hitting the air-water interface with bubble entrainment on Aug. 20-21 of 2012 at the Acoustic Test Facility (ATF) in NUWC Newport, RI. The ATF is a large indoor laboratory that specializes in accurate underwater sound recordings. The facility features a 700,000 gallon test tank, with dimensions of 60 ft. long, 40 ft. wide, and 35 ft. deep. Portions of the tank are lined with acoustic wedges to dampen out reflections.

The gas ventilation system was positioned on a catwalk above the acoustic tank. The jet nozzle was attached to a lowering arm and positioned the jet 1.75" above the interface. A total of 4 hydrophones were positioned in the tank beneath the catwalk to record the underwater sound as shown in Figure 4.1. The primary hydrophone was oriented horizontally and positioned 3 m directly below the gas jet. Another 2 hydrophones were oriented vertically and positioned 1 m away from the jet and 1 m below the surface. The fourth hydrophone was again oriented horizontally and positioned 1 m away from the jet and 1 m below the surface. The orientation of the hydrophones is important because of the directivity of the hydrophones. The hydrophones are least sensitive in the direction towards the cable they are attached to. The fourth hydrophone was added so there would be two phones oriented in the same direction for comparison.

In addition to the hydrophones, an underwater camera was used to take images of the bubble clouds generated by the impinging jets. In order to get better contrast in the underwater images, a black background was submerged behind the region where the jets impacted the surface of the water. Underwater lights were positioned off to the side, projecting light towards the bubble cloud and the black background. Finally, a meter stick was submerged near the entrained bubble cloud to provide a

sense of scale to the images.

Data was acquired from the hydrophones with the data acquisition system at the ATF. The acoustic data was sampled at a rate of 150 kHz. The time series was then converted to a power spectrum using 16,384 points, and the final spectrum recorded was a result of 16 spectral averages. For the bubble entrainment cases, the 1/16" and 1/8" nozzles were used. It was observed in preliminary trials that the 3/16" and .355" nozzles were not effective at entraining bubbles. The nozzles with larger diameters tend to produce relatively stable dimples at the surface, with few bubbles. It is easier for the jets with smaller diameters to break through the surface tension to entrain bubbles beneath the surface.

For each trial, the following procedure was used to acquire the data. First, recording of the gas instrumentation sensors was started in Labview. Then the gas flow was turned on, and the pressure regulator was adjusted to get the gas to the desired flow rate. This flow rate was estimated using incompressible flow theory, along with the nozzle diameter and desired exit velocity. After the desired flow rate was achieved, the acoustic data acquisition system was started. After the system had performed the 16 spectral averages, gas flow was shut off, followed by the gas data acquisition system.

5.2 Data analysis

5.2.1 Post-processing

Data was acquired from the hydrophones with the data acquisition system at the ATF. The acoustic data was sampled at a rate of 150 kHz. The time series was then

converted to a power spectrum using 16,384 points, and the final spectrum recorded was a result of 16 spectral averages. The data was then smoothed over frequency using a running average with a frequency window of 82 Hz and 90 percent overlap.

5.2.2 Uncertainty

The principal sources of uncertainty in this experiment are from the chaotic interaction of the high speed gas jets with the air-water interface. The entrained bubbles beneath the surface generally formed an ellipsoid shape, but the precise size of the cloud was rapidly changing. The size and distribution of the bubbles within the cloud were also rapidly changing. The high impact jets also splashed quite a bit of water into the air. These drops fell back down to the interface similar to raindrops, and could have impacted the acoustic measurements. Measurements of the exit velocities for these high speed jets indicate that the gas jet injection system can successfully maintain a steady exit velocity for these high flow rates. The only other source of error could be from the hydrophones. The acoustic data is converted to decibels, and due to their logarithmic nature the error is customarily marked as $+/- 1$ dB.

5.3 Results

The data from the bubble entrainment cases has been plotted in Figures 5.1-5.2. Figure 5.1 shows the smoothed pressure data for the 1/16" jet with the pressure regulator set to 50 psi. A plume of bubbles was created that extended about 4" below the surface of the water, as seen in Figure 5.3. Figure 5.2 shows the smoothed

pressure data for the 1/8" jet also with the pressure regulator set to 50 psi. Figure 5.4 shows a plume of bubbles was created that extended about 6.5" below the surface for the 1/8" nozzle. The recorded sound spectrum of the 1/16" jet and the 1/8" jet are of similar magnitude despite the larger impact area created by the 1/8" jet.

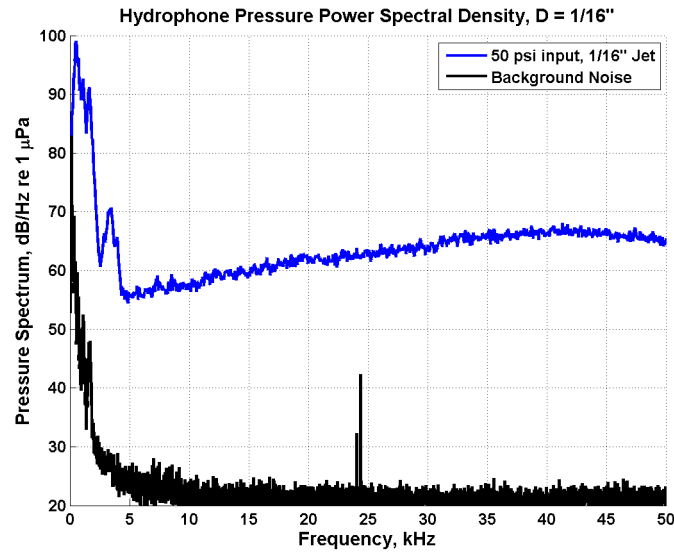


Figure 5.1: Pressure spectrum for 1/16" nozzle, pressure regulator set to 50 psi for bubble entrainment.

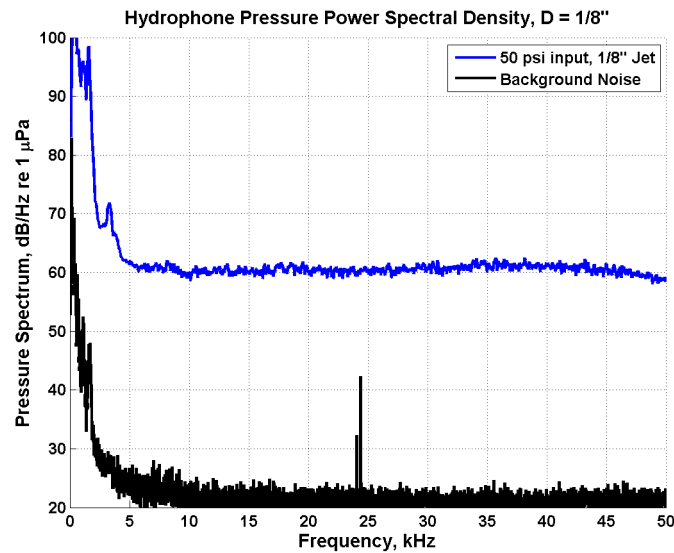


Figure 5.2: Pressure spectrum for $1/8''$ nozzle, pressure regulator set to 50 psi for bubble entrainment.

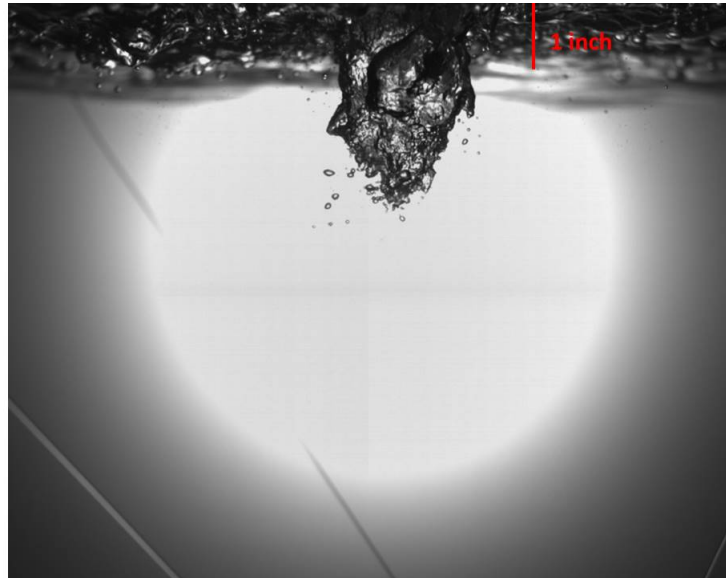


Figure 5.3: Underwater image of the bubble cloud produced by the $1/16''$ nozzle set to 50 psi for bubble entrainment.

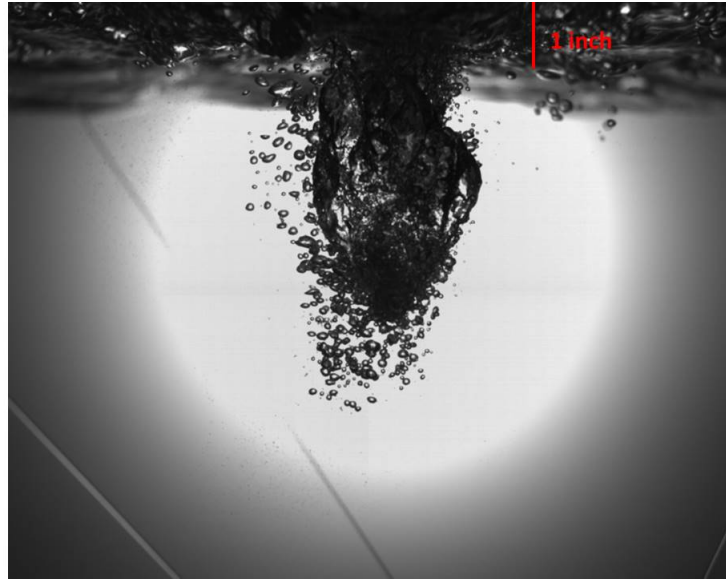


Figure 5.4: Underwater image of the bubble cloud produced by the $1/8''$ nozzle set to 50 psi for bubble entrainment.

5.4 Conclusions

When the pressure is set to 50 psi, the gas jet injection system is capable of entraining bubbles beneath the air-water interface with the $1/8''$ and $1/16''$ nozzles. The measurements of sound traveling through a bubble hemisphere provided experimental evidence of an acoustic signal being amplified over a range of frequencies by the bubble hemisphere. Observed dimensions of the bubble hemispheres will be used as an input to the theoretical model developed later in 6.3.5.

Chapter 6

Sound generated by a gas-jet impingement on a bubbly gas-water interface

This chapter describes the predicted sound radiation when a gas jet impacts a bubbly, two-phase interface. Section 6.1 presents the physical model and assumptions made in the initial formulation of the model. In the absence of bubbles, Foley *et al* [1] showed that the radiated sound was equivalent to that produced by a dipole source whose axis is normal to the interface and that the amplitude is dependent on the unsteady force applied by the gas jet. Section 6.2 outlines the important steps behind Foley's derivation. Section 6.3 describes the influence on Foley's result when a cloud of bubbles is created beneath the jet impact point. Section 6.4 discusses the effect of a bubbly layer at the air-water interface on the radiated sound. Section 6.5 summarizes the previous sections and discusses the implications of the predicted results.

6.1 The acoustic problem

Foley *et al.* [1,2] assumed that the unsteady forces produced by the 20 jets on the gas-water interface of the experimental supercavity can be regarded as statistically independent. Each jet is turbulent and impinges at near normal incidence, and together they form a set of uncorrelated acoustic sources. The spectrum of the overall far field jet noise can therefore be obtained by simple addition of the noise spectra of the individual jets.

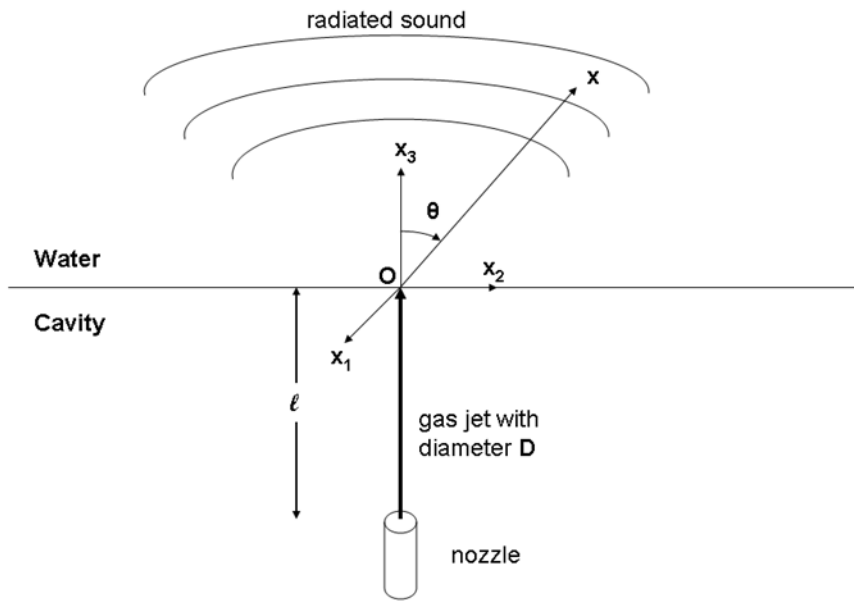


Figure 6.1: Foley's model used to estimate the sound generated by an unsteady jet incident normally on the gas-water interface.

6.2 Foley's problem

In practice the diameter D of the jet impact area on the interface is much smaller than the local cavity radius, so that the interface can be assumed locally plane.

Foley *et al.* [1,2] confined attention to those components of the sound having wavelengths (in the water) larger than D . This permits the impact region to be reduced to a fluctuating force applied at a single point on the interface. The model of sound generation at high frequencies is illustrated schematically in Figure 6.1. The locally plane jet-impact region of the gas-water interface is taken to coincide with the plane $x_3 = 0$ of the rectangular coordinate system $\mathbf{x} = (x_1, x_2, x_3)$, where the water of density ρ_o and sound speed c_o lies in $x_3 > 0$. The Mach number of the water flow relative to the cavity is assumed to be small enough that convection and refraction of sound by the mean flow can be neglected, such that small amplitude acoustic pressures $p(\mathbf{x}, t)$ in the water satisfy

$$\left(\frac{1}{c_o^2} \frac{\partial^2}{\partial t^2} - \nabla^2 \right) p = 0. \quad (6.2.1)$$

The idealized gas jet has circular cross-section, is coaxial with the x_3 axis and impinges normally on the interface from within the cavity ($x_3 < 0$). The jet exhausts at mean speed U_o from a circular nozzle of diameter D_o situated a distance ℓ from the interface (where $D_o \ll \ell$), and is assumed to exert an unsteady force on the water over a circular region of diameter $D \ll \ell$. If the dominant acoustic wavelengths produced by the jet are much larger than D the distributed force may be regarded as concentrated at a point on the interface, corresponding to a singular distribution of surface pressure $p = F\delta(x_1)\delta(x_2)$, where F is the net force. The force consists of a mean component together with a fluctuating part; only the unsteady part of the force is responsible for sound production, and we shall henceforth denote it by $F(t)$ and assume it to be a stationary random function of the time. The unsteady pressure elsewhere on the interface can be neglected because of the very large differences in the mean gas and water densities.

The mathematical problem of sound production by a single jet is accordingly governed by equation (6.2.1) in $x_3 > 0$ subject to the condition $p = F(t)\delta(x_1)\delta(x_2)$ on $x_3 = 0$. The solution with outgoing wave behavior is the dipole pressure field [8, 9]

$$p(\mathbf{x}, t) = -\frac{\partial}{\partial x_3} \left[\frac{1}{2\pi|\mathbf{x}|} F \left(t - \frac{|\mathbf{x}|}{c_o} \right) \right], \quad x_3 > 0, \quad (6.2.2)$$

$$\simeq \frac{\cos \theta}{2\pi c_o |\mathbf{x}|} \frac{\partial F}{\partial t} \left(t - \frac{|\mathbf{x}|}{c_o} \right), \quad |\mathbf{x}| \rightarrow \infty, \quad \cos \theta = \frac{x_3}{|\mathbf{x}|}. \quad (6.2.3)$$

The frequency spectrum $\Phi_{FF}(\omega)$ of the jet force is defined such that

$$\langle F^2(t) \rangle = \int_0^\infty \Phi_{FF}(\omega) d\omega, \quad (6.2.4)$$

where the angle brackets $\langle \rangle$ denote an ensemble or time average. The corresponding acoustic pressure frequency spectrum $\Phi_{pp}(\mathbf{x}, \omega)$ satisfies

$$\langle p^2(\mathbf{x}, t) \rangle = \int_0^\infty \Phi_{pp}(\mathbf{x}, \omega) d\omega \quad (6.2.5)$$

and it follows from (6.2.3) that

$$\Phi_{pp}(\mathbf{x}, \omega) \approx \frac{\cos^2 \theta}{2\pi^2 |\mathbf{x}|^2} k_o^2 \Phi_{FF}(\omega), \quad |\mathbf{x}| \rightarrow \infty. \quad (6.2.6)$$

where $k_o = \omega/c_o$ is the acoustic wavenumber.

6.2.1 Comparison of acoustic model to measured results

Foley's model was the most appropriate to use for cases where the interface was relatively smooth with no bubbles. The measured unsteady force spectra described

in Chapter 3 were used as inputs to Foley's original model. The measurements from each force sensor were added together for a cumulative force input for the model as shown in Equation 6.2.7.

$$F_{TOTAL} = F_{A11} + F_{C528} + F_{C501} + F_{C502} + F_{C532} + F_{C530} + F_{C519} \quad (6.2.7)$$

The total force was calculated by summing up the contributions from the individual force sensors in Newtons. The predicted acoustic model for the 1/16" nozzle is shown in Figure 6.2. For this nozzle, the force data hits the noise floor at about 8 kHz. The predicted models for the 1/8", 3/16", and 0.355" are shown in Figures 6.3-6.5. The spikes in the model at 32 kHz are from the resonant frequency of the force sensors.

Figures 6.6-6.8 shows a comparison of the measured and modeled acoustic spectrums for the 1/8", 3/16", and 0.355" nozzles respectively with an exit velocity of 220 ft/s. The predicted levels in all of the models were about 15 dB below the measured acoustic power level. There are a few possible explanations for the under prediction of the current acoustic model. It was assumed during the derivation of the model that the area of jet impact could be represented with a delta function. In reality, the jet exerts force on a small circular area on the interface. There could be additional sound radiated into the water that is not accounted for due to the use of a delta function to represent the impact area. Also, the current model does not account for any in-air jet noise transmitting through the interface. Sound of the air jet through the interface is not the primary mechanism of radiated sound in the water, but it could contribute some to the overall energy.

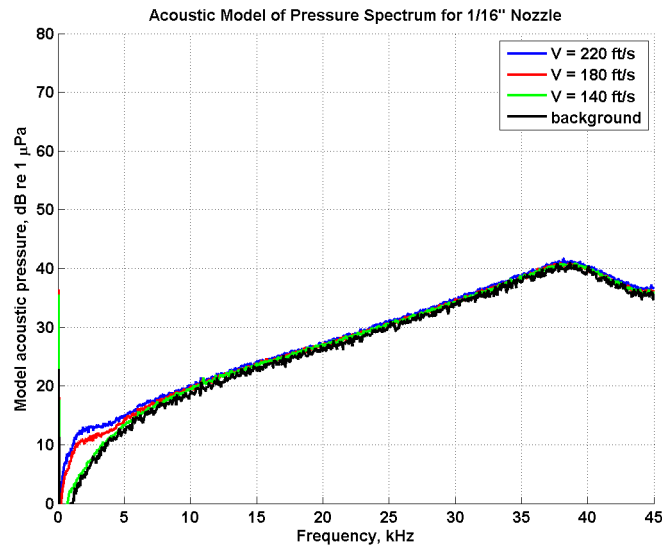


Figure 6.2: Predicted acoustic model for the 1/16" nozzle.

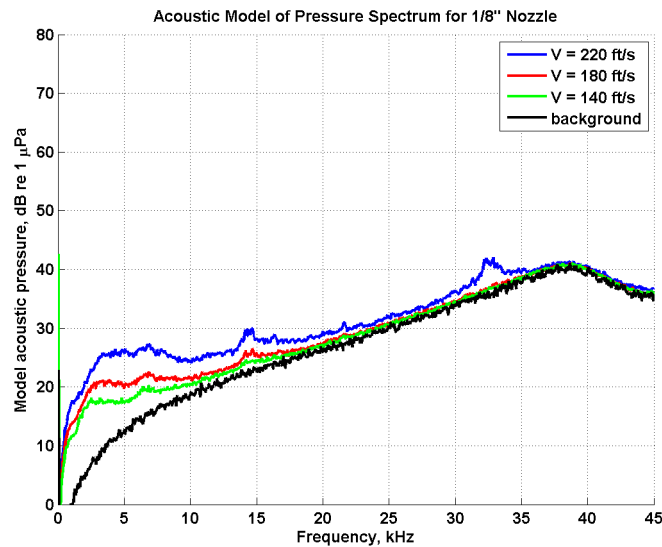


Figure 6.3: Predicted acoustic model for the 1/8" nozzle.

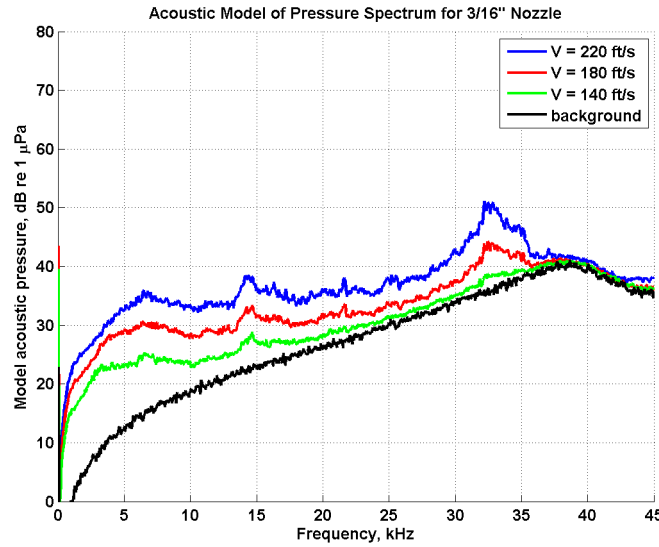


Figure 6.4: Predicted acoustic model for the 3/16" nozzle.

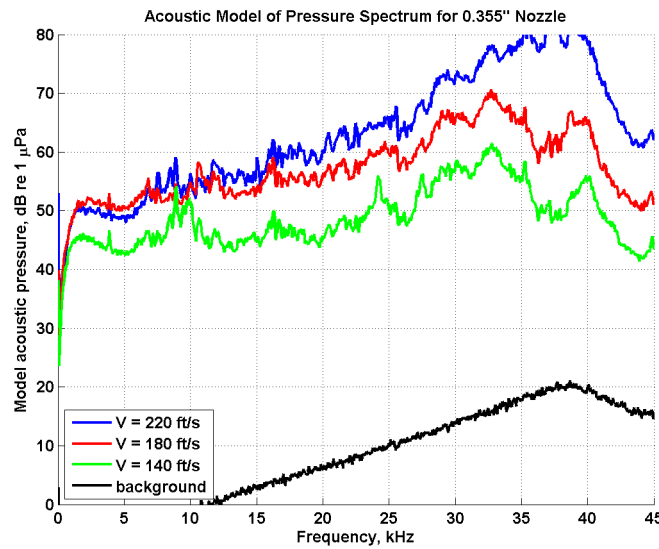


Figure 6.5: Predicted acoustic model for the 0.355" nozzle.

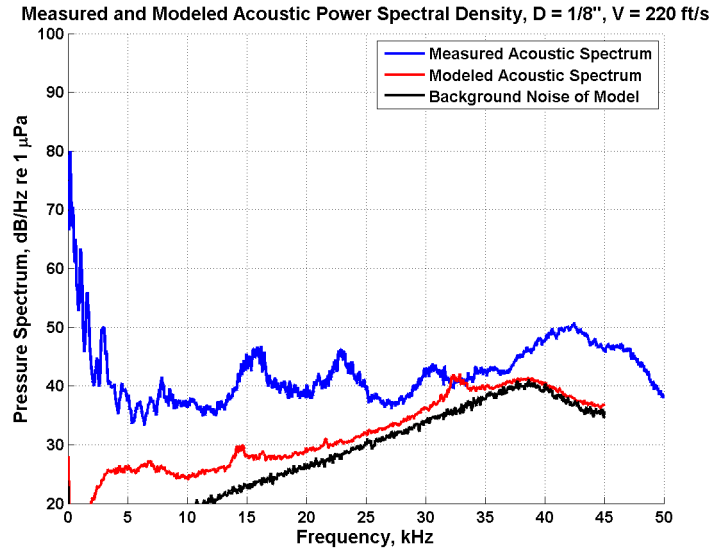


Figure 6.6: Comparison of measured and predicted acoustic pressure spectrum for the 1/8" nozzle with an exit velocity of 220 ft/s.

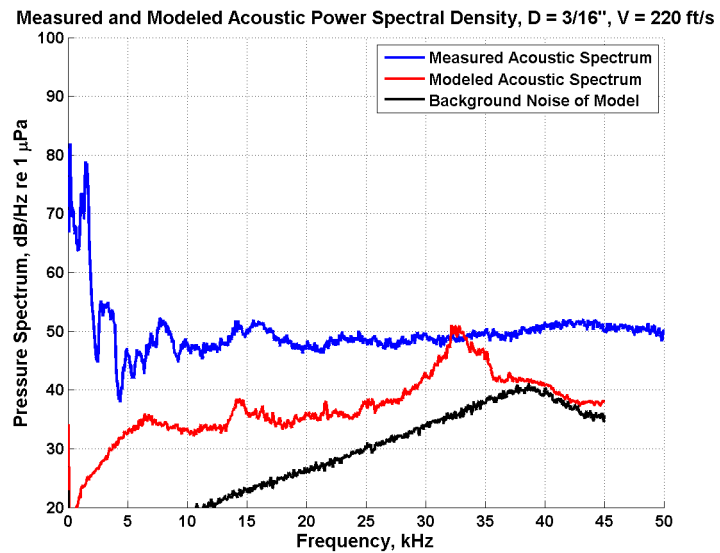


Figure 6.7: Comparison of measured and predicted acoustic pressure spectrum for the 3/16" nozzle with an exit velocity of 220 ft/s.

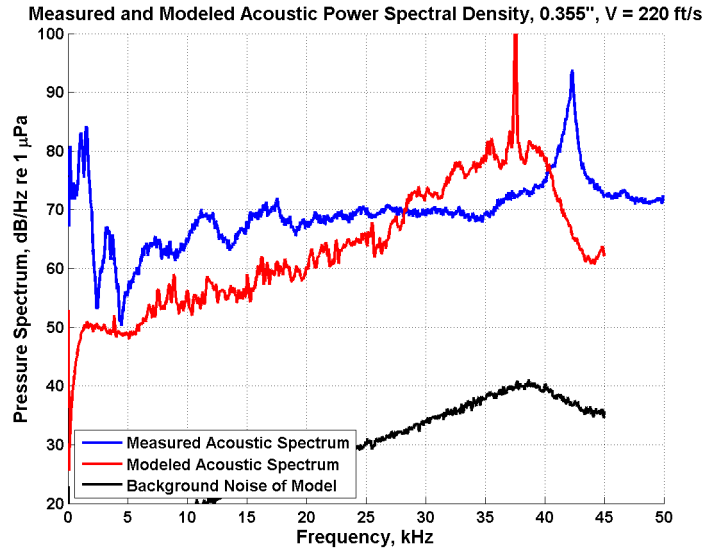


Figure 6.8: Comparison of measured and predicted acoustic pressure spectrum for the 0.355" nozzle with an exit velocity of 220 ft/s.

The relationship between jet exit velocity and the modeled acoustic pressure spectrum level was determined with the same logic applied in section 4.3.1. The pressure spectrum level was averaged between a range of frequencies and plotted against the log of the exit velocity. A curve fit yielded a coefficient β which determined the power law relation between jet exit velocity and pressure spectrum level. The noise floor associated with the force spectrum measurements was used as the limit for the frequency range of the analyzed model pressure levels.

Figure 6.9 shows the power law relation between exit velocity and modeled pressure spectrum levels for the 1/8" nozzle using a frequency range of 2-7 kHz. The model hits the noise floor of the force spectrum measurements above 7 kHz. A curve fit for the average pressure spectrums within the 2-7 kHz frequency ranges yielded a β of 1.82.

For the 3/16" nozzles, the model hits the noise floor at 17 kHz. The power

law relation β was calculated over two frequency bins, the first ranges from 2-7 kHz while the second ranges from 7-17 kHz. Figures 6.10-6.11 plot the calculated curve fits for the 3/16" nozzles over the first and second frequency bins respectively. This yielded a β of 2.21 between 2-7 kHz, and a β of 2.43 between 7-17 kHz.

For the 0.355" nozzle, there were no issues with the noise floor of the force spectrum measurements. But the modeled data in the upper frequencies above 20 kHz was significantly affected by the internal resonance of the force sensors. Therefore modeled data above 20 kHz was not used in the power law calculations. The power law relation β was calculated over two frequency bins, the first ranges from 2-7 kHz while the second ranges from 7-20 kHz. Figures 6.12-6.13 plot the calculated curve fits for the 0.3554" nozzles over the first and second frequency bins respectively. A β of 2.19 was calculated between 2-7 kHz, and a β of 3.63 was calculated between 7-20 kHz. The power law relations determined for the modeled pressure spectrum and jet exit velocity is similar in scale to the β 's calculated for the measured acoustic spectrum.

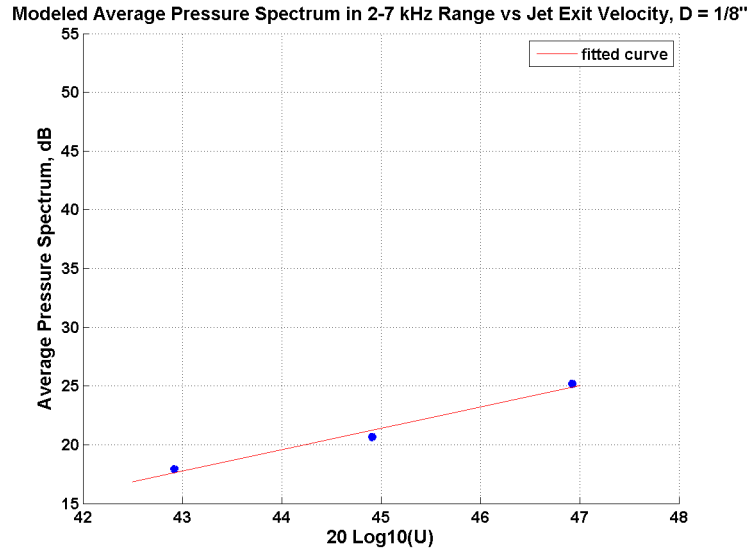


Figure 6.9: Average modeled acoustic power spectrum vs the log of the velocity for the $1/8''$ nozzle over the 2-7 kHz frequency range. The slope of the data fit is $\beta = 1.82$.

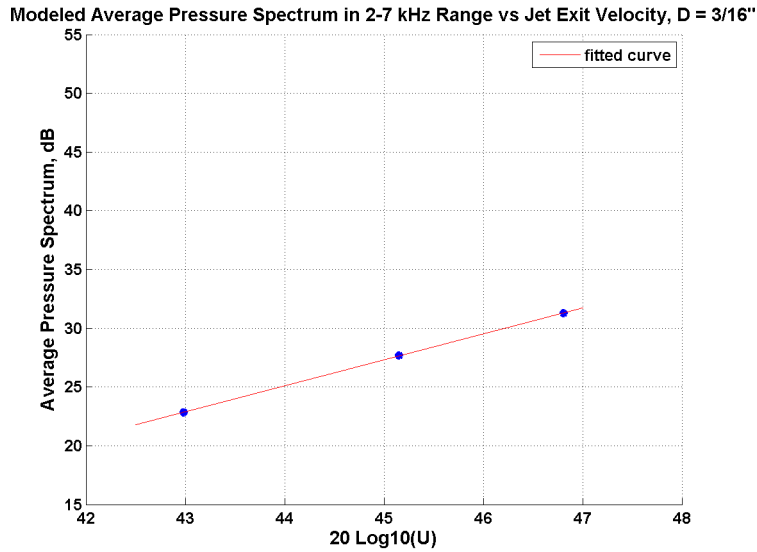


Figure 6.10: Average modeled acoustic power spectrum vs the log of the velocity for the $3/16''$ nozzle over the 2-7 kHz frequency range. The slope of the data fit is $\beta = 2.21$.

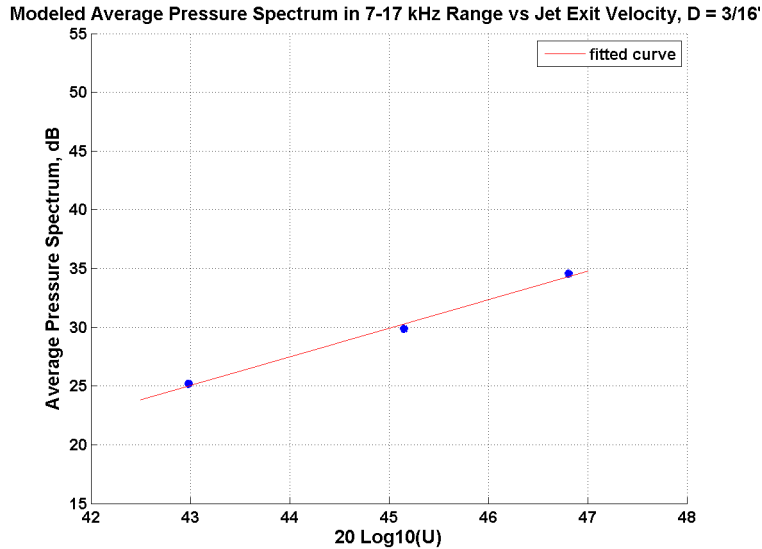


Figure 6.11: Average modeled acoustic power spectrum vs the log of the velocity for the $3/16''$ nozzle over the 7-17 kHz frequency range. The slope of the data fit is $\beta = 2.43$.

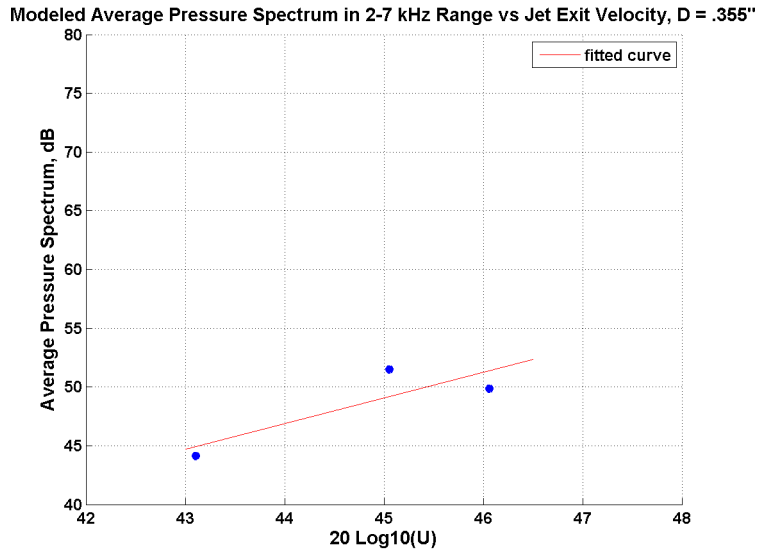


Figure 6.12: Average modeled acoustic power spectrum vs the log of the velocity for the $0.355''$ nozzle over the 2-7 kHz frequency range. The slope of the data fit is $\beta = 2.19$.

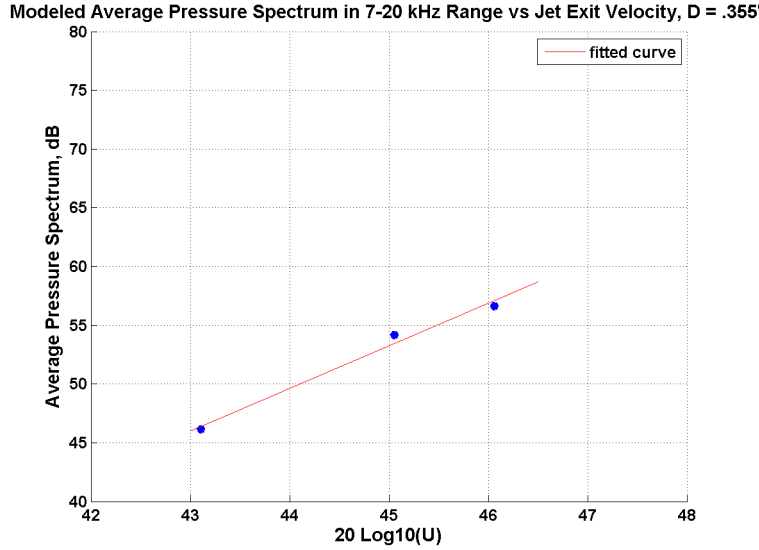


Figure 6.13: Average modeled acoustic power spectrum vs the log of the velocity for the 0.355" nozzle over the 7-20 kHz frequency range. The slope of the data fit is $\beta = 3.63$.

6.3 Influence of a bubbly cloud

This derivation was motivated by observations of gas jets impinging on the air-water interface at high velocities. At sufficient speeds, the gas jets would entrain a cloud of bubbles beneath the surface of the water. These clouds were generally ellipsoid in shape, but the precise geometry of the cloud would fluctuate rapidly. The best start at an analytical model for this observed phenomenon was to begin with a bubble hemisphere.

6.3.1 Mean properties of the cloud

The influence on sound production by a jet of a bubbly interface between the cavity and the water will be investigated by modifying Foley's [1,2] planar interface

approximation in the manner illustrated in Figure 6.14. It is assumed that the bubble cloud is a homogeneous hemisphere with radius R from the coordinate origin. It will be assumed that compression waves within the layer have wavelengths that are sufficiently large compared to the characteristic bubble diameter that the layer can be modeled analytically as a homogeneous acoustic medium of whose density $\bar{\rho}$ and sound speed \bar{c} are given by [12,38]

$$\left. \begin{aligned} \bar{\rho} &= (1 - \sigma)\rho_o + \sigma\rho_g \\ \bar{c}_o^2 &\simeq \frac{\gamma_g p_o}{\rho_o \sigma (1 - \sigma)} \end{aligned} \right\} \quad (6.3.1)$$

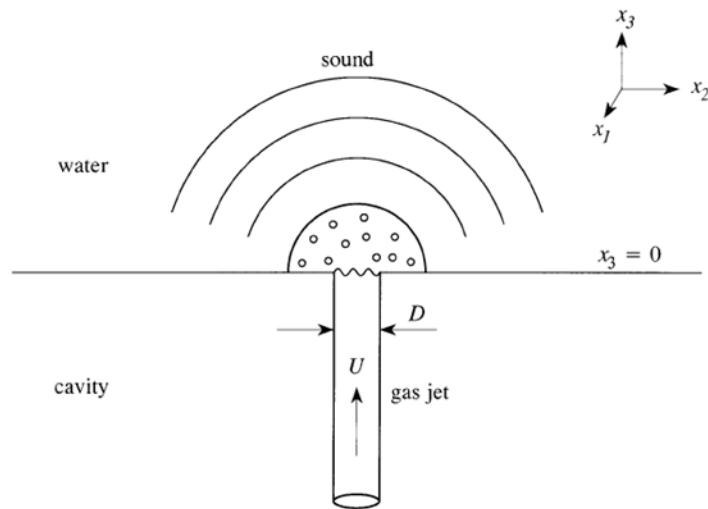


Figure 6.14: Production of sound by a jet incident on the water interface in the presence of a hemispherical bubble cloud.

where γ_g and ρ_g are the ratio of specific heats and the mean density of the gas

phase, which is assumed to occupy a fractional volume σ within the layer, and p_o is the mean cavity pressure. The precise value of σ has not been measured, but it is unlikely to exceed 0.1 and probably exceeds 0.01, so that typically $\bar{c}/c_o \sim 1/15 \ll 1$. Similarly, the specific acoustic impedance \mathcal{Z} of the bubbly layer (relative to water) is

$$\mathcal{Z} = \frac{\bar{\rho}\bar{c}}{\rho_o c_o}. \quad (6.3.2)$$

where typically $\mathcal{Z} \approx 0.07$.

At high frequencies the effective wave speed \bar{c} in the cloud is dependent on the value of the mean resonant frequencies of the individual bubbles. This is related to the mean bubble radius R_b by the approximate formula [6,12,30,38-40]

$$\omega_b \approx \left(\frac{3\gamma_g p_0}{\rho_o R_b^2} \right)^{1/2} \quad (6.3.3)$$

For acoustic waves with time dependence of the type $e^{-i\omega t}$ we have [6,40]

$$\frac{1}{\bar{c}^2} \approx \frac{1}{c_o^2} + \frac{1}{\bar{c}_o^2} \left(1 - \frac{\omega^2}{\omega_b^2} - i\eta \frac{\omega}{\omega_b} \right)^{-1}, \sigma \ll 1. \quad (6.3.4)$$

The empirical damping coefficient η has been estimated by Fox *et al*, [32,40] to be about $\frac{1}{2}$. This value of η is dependent on the resonant frequency of the bubbles. The effects of adjusting the value of η will be investigated later in 6.3.5.

6.3.2 Calculation of the radiated sound

Let

$$F(t) = \int_{-\infty}^{\infty} \hat{F}(\omega) e^{-i\omega t} dt, \quad (6.3.5)$$

where $\hat{F}(\omega)$ is the Fourier transform of the force $F(t)$. The pressure distribution on the interface $x_3 = 0$ can then be expressed by

$$p(x_1, x_2, 0, t) = F(t)\delta(x_1)\delta(x_2) = \int_{-\infty}^{\infty} \hat{F}(\omega)\delta(x_1)\delta(x_2)e^{-i\omega t}d\omega. \quad (6.3.6)$$

The first step in calculating the radiated sound is to solve for the time-harmonic pressure with amplitude of $\hat{F}(\omega)\delta(x_1)\delta(x_2)$ applied at $x_3 = 0$. The radiated sound is then obtained by multiplying by $e^{-i\omega t}$ and integrating over $-\infty < \omega < \infty$.

The main theme in this calculation is considering boundary conditions, and ensuring that there is continuity of pressure and normal velocity. Due to symmetry, the pressure radiated from the interface in $x_3 > 0$ depends only on the radial distance $r \equiv |\mathbf{x}|$ and the polar angle θ measured from the positive x_3 direction. The time-harmonic solution for this type of sound radiation is

$$\hat{p}(r, \theta, \omega) = \frac{ik_o^2 h_1(k_o r) \cos \theta}{2\pi} \hat{F}(\omega), \quad 0 < \theta < \frac{\pi}{2}, \quad (6.3.7)$$

where

$$h_1(x) = i \frac{\partial}{\partial x} \left(\frac{e^{ix}}{x} \right)$$

is the first order spherical Hankel function [12,41]. The boundary condition at $x_3 = 0$ is satisfied because $\cos \theta = x_3/r$, and as $r \equiv (x_1^2 + x_2^2 + x_3^2)^{\frac{1}{2}} \rightarrow 0$ the right hand side of equation (6.3.7) becomes

$$\frac{x_3 \hat{F}(\omega)}{2\pi (x_1^2 + x_2^2 + x_3^2)^{\frac{3}{2}}} \rightarrow \hat{F}(\omega)\delta(x_1)\delta(x_2)$$

The next region to consider is inside the bubble cloud. The time-harmonic solution which also satisfies the same boundary condition at $x_3 = 0$ the same

boundary condition is

$$\hat{p}(r, \theta, \omega) = \frac{i\bar{k}^2 \cos \theta}{2\pi} \left(\hat{F}h_1(\bar{k}r) + Aj_1(\bar{k}r) \right), \quad r < R, \quad (6.3.8)$$

where $\bar{k} = \omega/\bar{c}$ is the acoustic wavenumber within the cloud, $j_1(x)$ is the first order spherical Bessel function [41], and the coefficient $A = A(\omega)$ still needs to be solved for.

In the clear water beyond the bubble, we use a similar logic to write the time-harmonic solution

$$\hat{p}(r, \theta, \omega) = \frac{i\bar{k}^2 \cos \theta}{2\pi} Bh_1(k_0 r), \quad r > R, \quad (6.3.9)$$

where the coefficient $B = B(\omega)$ remains undetermined.

The coefficients A and B are solved from satisfying the continuity of pressure and normal velocity at $r = R$. The normal velocity is related to the pressure by $(1/\rho)\partial p/\partial r$, and so

$$\left. \begin{aligned} \hat{F}h_1(\bar{k}R) + Aj_1(\bar{k}R) &= Bh_1(k_o R), \\ \hat{F}h'_1(\bar{k}R) + Aj'_1(\bar{k}R) &= (\mathcal{Z}/f)Bh'_1(k_o R) \end{aligned} \right\} \quad (6.3.10)$$

where the prime indicates differentiation, and

$$f(\omega) = \left[\left(\frac{\bar{c}_o}{c_o} \right)^2 + \left(1 - \frac{\omega^2}{\omega_b^2} - i\eta \frac{\omega}{\omega_b} \right)^{-1} \right]^{\frac{1}{2}} \quad (6.3.11)$$

Solving the system of equations in (6.3.10) for B and using the Wronksian $h_1(x)j'_1(x) - h'_1(x)j_1(x) = -i/x^2$ [41], gives

$$B(\omega) = \frac{-i\hat{F}(\omega)}{(\bar{k}R)^2 [h_1(k_oR)j'_1(\bar{k}R) - (\mathcal{Z}/f)h'_1(k_oR)j_1(\bar{k}R)]}. \quad (6.3.12)$$

This coefficient can then be substituted into equation (6.3.9). The pressure outside the cloud is then found by multiplying this result by $e^{-i\omega t}$ and integrating over all frequencies

$$p(\mathbf{x}, t) = \frac{\cos \theta}{2\pi R^2} \int_{-\infty}^{\infty} \frac{\hat{F}(\omega)h_1(k_o|\mathbf{x}|)e^{-i\omega t}d\omega}{h_1(k_oR)j'_1(\bar{k}R) - (\mathcal{Z}/f)h'_1(k_oR)j_1(\bar{k}R)}, \quad |\mathbf{x}| > R \quad (6.3.13)$$

6.3.3 The far field pressure

At ranges $|\mathbf{x}|$ that are much greater than the characteristic acoustic wavelength, the asymptotic solution $h_1(x) \sim e^{ix}/x, |x| \gg 1$, can be used in (6.3.13) which gives

$$p(\mathbf{x}, t) \approx \frac{-\cos \theta}{2\pi R^2 |\mathbf{x}|} \int_{-\infty}^{\infty} \frac{\hat{F}(\omega)e^{-i\omega(t-|\mathbf{x}|/c_o)}d\omega}{k_o [h_1(k_oR)j'_1(\bar{k}R) - (\mathcal{Z}/f)h'_1(k_oR)j_1(\bar{k}R)]}, \quad |\mathbf{x}| \rightarrow \infty \quad (6.3.14)$$

In the absence of the bubble cloud, $\bar{k} \rightarrow k_o$, and the denominator of the integrand in (6.3.13) becomes $-i/(k_oR)^2$, and formula (6.3.13) becomes the exact result (6.2.2) for clear water. The approximation in (6.3.14) also reduces to the clear water far field approximation (6.2.3). The radiated acoustic field exhibits a dipole directivity with and without the presence of the bubble cloud.

6.3.4 The acoustic pressure frequency spectrum

The definitions of the force and pressure spectrums in (6.2.4) and (6.2.5) allows the acoustic pressure spectrum to be expressed as

$$\Phi_{pp}(\mathbf{x}, \omega) \approx \frac{\cos^2 \theta k_o^2 \Phi_{FF}(\omega)}{4\pi^2 |\mathbf{x}|^2 (k_o R)^4 \left[h_1(k_o R) j'_1(\bar{k}R) - (\mathcal{Z}/f) h'_1(k_o R) j_1(\bar{k}R) \right]^2}, \quad |\mathbf{x}| \rightarrow \infty. \quad (6.3.15)$$

When the void fraction σ of the bubble cloud goes to zero, (6.3.15) becomes equivalent to the pressure spectrum predicted by Foley [1,2].

The acoustic power gain $G(\omega)$ produced by the bubble cloud is determined by the terms in the denominator related to the composition of the bubble cloud

$$G(\omega) = -10 \log_{10} \left((k_o R)^4 \left[h_1(k_o R) j'_1(\bar{k}R) - (\mathcal{Z}/f) h'_1(k_o R) j_1(\bar{k}R) \right]^2 \right) dB. \quad (6.3.16)$$

There are peaks in the gain at the resonant frequencies of the bubble cloud, roughly corresponding to the interior oscillations of a hemisphere of fluid with a flat circular boundary. This can be seen in Figure 6.15 for the case in which the mean bubble resonant frequency $f_b = \omega_b/2\pi = 50$ kHz. Resonance frequencies over for other values of f_b show similar characteristics.

A more realistic model of the acoustic gain will take into account the time dependent

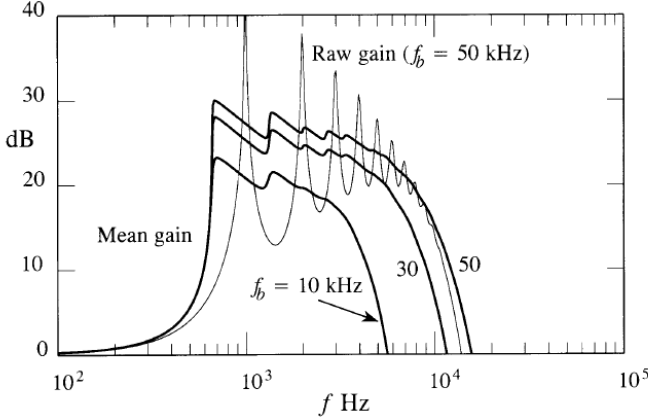


Figure 6.15: Mean gain $G(\omega)$ in the sound pressure level produced by a hemispherical bubble cloud of nominal radius 5 cm for different values of the bubble resonance frequency f_b . The 'Raw gain' is calculated without averaging with respect to the cloud radius when $f_b = 50$ kHz.

state of the composition of the bubble cloud. This is accomplished by assuming a uniform variation of the bubble cloud radius over the range $R_{min} < R < R_{max}$. The mean gain can then be expressed as

$$\langle G(\omega) \rangle = -10 \log_{10}(\Delta) \quad (6.3.17)$$

where

$$\Delta = \frac{1}{R_{max} - R_{min}} \int_{R_{min}}^{R_{max}} \frac{dR}{(k_o R)^4 \left[h_1(k_o R) j'_1(\bar{k}R) - (\mathcal{Z}/f) h'_1(k_o R) j_1(\bar{k}R) \right]^2} \quad (6.3.18)$$

Figure 6.15 also shows the variation of the mean gain $\langle G(\omega) \rangle$ for a bubble cloud of nominal radius $R = 5$ cm and for $f_b = 10, 30, 50$ kHz. The radius of the cloud fluctuates between $R_{min} = R/2$ and $R_{max} = 3R/2$. The averaging removes the large peaks in the gain, and tends to yield a more uniform gain of 20-30 dB over a range

of frequencies below the resonant frequencies of the bubbles. At higher frequencies, the predicted gain is negative, and decreases rapidly with increasing frequency.

6.3.5 Comparisons with measured acoustic power

The model for acoustic transmission through a bubble hemisphere was used to predict any acoustic signal gains through the bubble hemisphere. The hemisphere radius and bubble size inputs used in the model were based on the images taken of the entrained bubbles. The bubble clouds had an ellipsoid shape, but the simpler hemispherical model still provided some good results. Figure 6.16 shows the predicted acoustic gain through a bubble hemisphere with a radius of 2.5" composed of tiny bubbles with individual radii of 0.032". The thick blue curve shows the result of averaging the spectrum for different bubble hemisphere radii. The nominal radius was $2.5'' \pm 0.62''$. This helps to model a hemisphere which is rapidly changing size. The model predicts an increase of about 15 dB from about 800-2000 Hz.

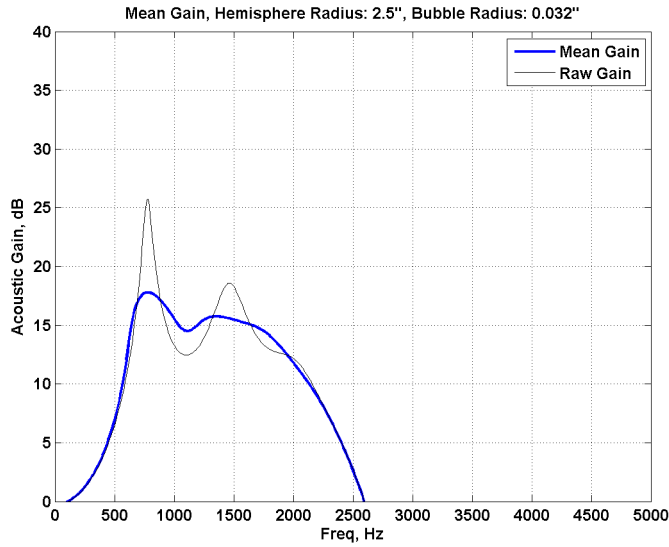


Figure 6.16: Predicted acoustic gains through a bubble hemisphere with a radius of 2.5" composed of bubbles with individual radii of 0.032".

Figures 6.17-6.18 zooms in on the 0-5 kHz range of the pressure spectrums for the 1/16" and 1/8" pressure spectrums. This view makes it easier to see if there are any bumps in the spectrum that match the prediction from the model. Both of these spectrums show an increase in signal through the frequency range predicted by the acoustic model.

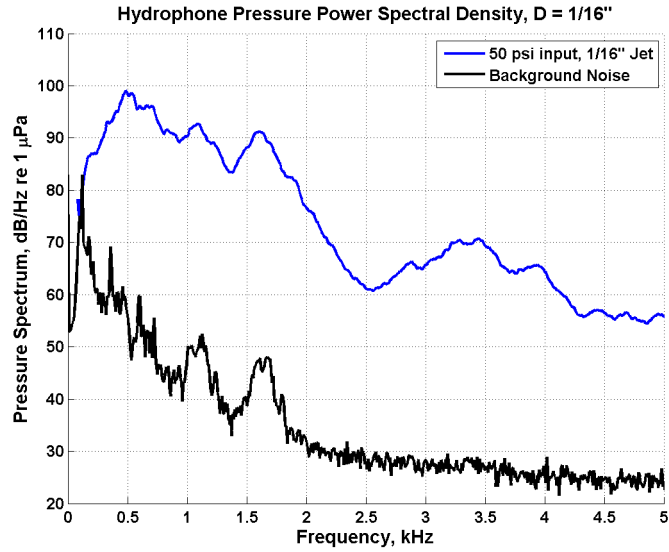


Figure 6.17: Measured acoustic pressure spectrum, 0-5 kHz, for the 1/16" nozzle set to 50 psi.

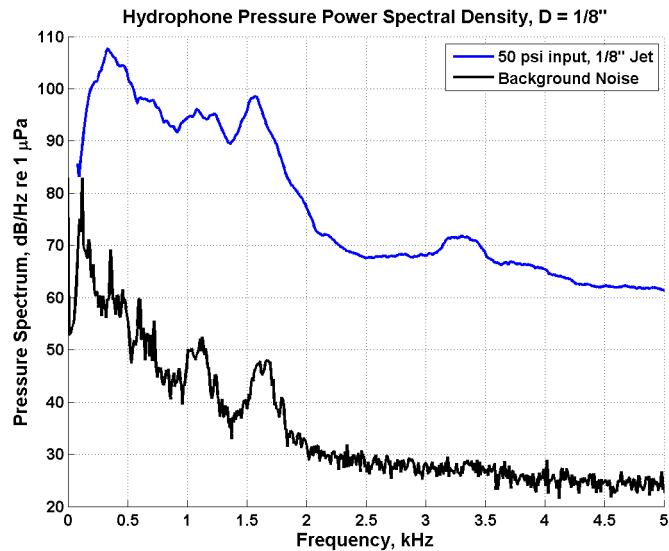


Figure 6.18: Measured acoustic pressure spectrum, 0-5 kHz, for the 1/8" nozzle set to 50 psi.

The measured force spectrums were used as an input to the bubble hemisphere model. The measurements from the individual force sensors were added together to

produce a cumulative force that was used as an input to the model (Equation 6.2.7). The measured force spectrums for the 50 psi cases were significantly affected by the resonance frequency of the force sensors. For this reason, the force spectrum was corrected to match the trend of the force spectrum data before the resonant spike of the force sensors. This straight line correction explains the smoothness of the modeled curves at the upper frequencies. Figure 6.19 plots the comparison of the bubble hemisphere acoustic model with the measured acoustic pressure spectrum for the 1/16" nozzle set at 50 psi. The hemisphere was modeled as having a radius of 1.18" composed of bubbles with internal radii of .0354". The effects of varying the damping coefficient η is explored in Figures 6.19-6.20. A damping coefficient η of 0.1 yields the highest spike from the bubble hemisphere, but also predicts a large unrealistic dip in the predicted curve. Larger values of η smooth this spike out. Figure 6.20 plots the comparison of the bubble hemisphere acoustic model with the measured acoustic pressure spectrum for the 1/8" nozzle set at 50 psi. The same bubble hemisphere parameters were used in this figure.

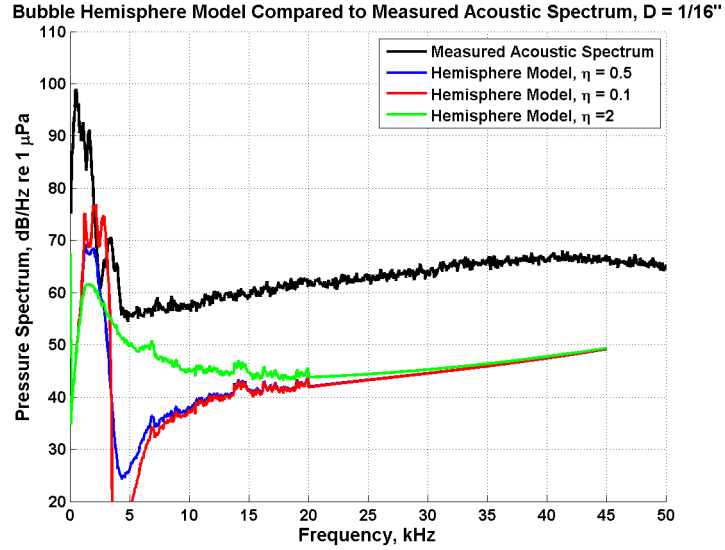


Figure 6.19: Comparison of modeled bubble hemisphere acoustic results and measured pressure spectrums for the 1/16" set at 50 psi. The hemisphere was modeled with a radius of 1.18" composed of bubbles with internal radii of .0354"

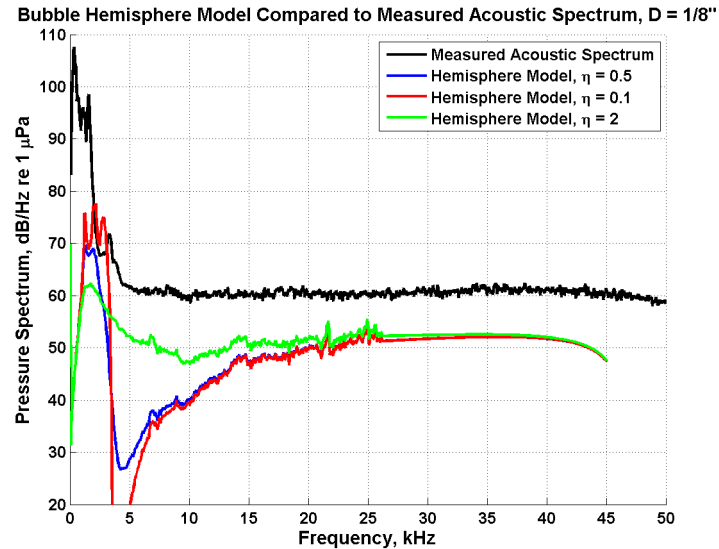


Figure 6.20: Comparison of modeled bubble hemisphere acoustic results and measured pressure spectrums for the 1/8" set at 50 psi. The hemisphere was modeled with a radius of 1.18" composed of bubbles with internal radii of .0354"

6.4 Influence of a bubbly layer

This derivation was motivated by observations of a supercavitating vehicle in a water tunnel with a rough and bubbly interface as seen in Figure 1.2. This was a result of the ventilating jets being oriented normal to the interface instead of being deflected to hit the interface at a shallow angle. In a dynamic and unpredictable environment such as the ocean, it is likely that the interface of a supercavity will be as perfectly smooth as one generated in a water tunnel. Therefore the potential presence and impact of a bubbly layer near the interface is an important case to consider in the application of supercavitating vehicles. Unfortunately it was not within the scope of this study to experimentally replicate a bubble layer near an air-water interface. All of our studies involved gas jets hitting a still body of water. At low impact velocities the gas jet would create an indentation on the interface. If the water were moving, some of these indentations would shear off and create a layer of bubbles near the interface.

6.4.1 Mean properties of the bubble layer

The influence on sound production by a jet of a bubbly interface between the cavity and the water will be investigated by modifying Foley's [1,2] planar interface approximation in the manner illustrated in Figure 6.21. The bubbles form a homogeneous layer of nominal thickness h between the gas cavity and the water (within the interval $0 < x_3 < h$). It will be assumed that compression waves within the layer have wavelengths that are sufficiently large compared to the characteristic bubble diameter that the layer can be modeled analytically as a homogeneous

acoustic medium of whose mean density $\bar{\rho}$ and sound speed \bar{c} are given by [12,38] Equation 6.3.1.

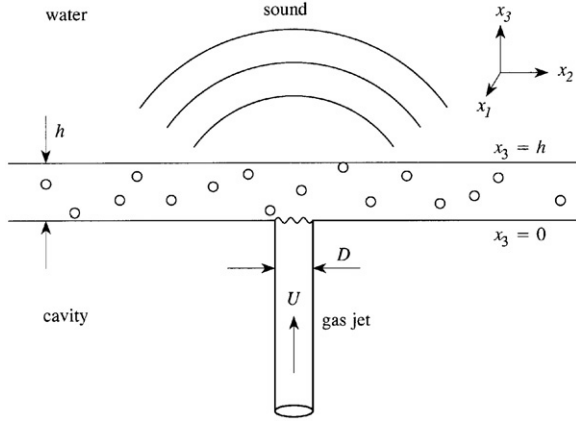


Figure 6.21: Model used to calculate the sound generated when the jet is incident normally on the lower face $x_3 = 0$ of a uniform bubbly interface between the cavity in $x_3 < 0$ and water in $x_3 > h$.

The actual wave speed \bar{c} in the bubble layer is affected by the mean resonance frequency of the bubbles, ω_b , which in turn depends on the bubble radius R_b , which is given approximately by [6,12,38,40,42] Equation 6.3.3. In a first approximation when $\sigma \ll 1$, and for waves of time dependence $\propto e^{-i\omega t}$, we have [6,40] Equation 6.3.4. In terms of these variables, it is convenient to introduce the specific acoustic impedance \mathcal{Z} of the bubbly layer (relative to water) is given in Equation 6.3.2.

6.4.2 Calculation of the radiated sound

Introduce the Fourier transform of the force strength $F(t)$, defined by

$$\hat{F}(\omega) = \frac{1}{2\pi} \int_{-\infty}^{\infty} F(t) e^{i\omega t} dt. \quad (6.4.1)$$

Then

$$F(t)\delta(x_1)\delta(x_2) = \frac{1}{(2\pi)^2} \iint_{-\infty}^{\infty} \hat{F}(\omega) e^{i(\mathbf{k}\cdot\mathbf{x}-\omega t)} d^2\mathbf{k} d\omega, \quad (6.4.2)$$

where $\mathbf{k} = (k_1, k_2, 0)$ and $d^2\mathbf{k} = dk_1 dk_2$. The sound produced by jet impact can now be determined by first considering that radiated into the water when the elementary pressure distribution $\hat{F}(\omega) e^{i(\mathbf{k}\cdot\mathbf{x}-\omega t)}$ is applied at $x_3 = 0$, over the lower face of the bubble layer. The aggregate sound generated by the jet is then obtained by application of the integral operator

$$\frac{1}{(2\pi)^2} \iint_{-\infty}^{\infty} (\cdot) d^2\mathbf{k} d\omega. \quad (6.4.3)$$

To do this, the pressure field above the interface (in $x_3 > h$) in the simplified problem is put in the form [43]

$$p = A e^{i(\mathbf{k}\cdot\mathbf{x} + \gamma(x_3 - h) - \omega t)}, \quad (6.4.4)$$

where $A = A(\mathbf{k}, \omega)$ is to be determined, and $\gamma = (\omega^2/c_o^2 - k^2)^{\frac{1}{2}}$. The radiation condition is satisfied by requiring the square root $(\omega^2/c_o^2 - k^2)^{\frac{1}{2}}$ to have the same sign as ω when the argument is positive and to be positive imaginary when the argument is negative.

Within the bubble layer it is assumed that pressure fluctuations satisfy the wave equation (6.2.1) with c_o replaced by \bar{c} , so that we can write

$$p = (B e^{i\bar{\gamma}x_3} + C e^{-i\bar{\gamma}x_3}) e^{i(\mathbf{k}\cdot\mathbf{x} - \omega t)}, \quad \bar{\gamma} = (\omega^2/\bar{c}^2 - k^2)^{\frac{1}{2}}, \quad (6.4.5)$$

where the $B(\mathbf{k}, \omega)$, $C(\mathbf{k}, \omega)$ are to be determined.

The coefficients A , B , C are obtained by application of conditions of continuity

of pressure at $x_3 = 0$, h and (when the mean flow Mach number is infinitesimal) continuity of the x_3 component of velocity. The pressure conditions yield

$$\left. \begin{aligned} \hat{F}(\omega) &= B + C, & \text{at } x_3 = 0, \\ A &= B e^{i\bar{\gamma}h} + C e^{-i\bar{\gamma}h}, & \text{at } x_3 = h. \end{aligned} \right\} \quad (6.4.6)$$

Continuity of normal velocity requires that $(1/\rho)\partial p/\partial x_3$ be continuous at $x_3 = h$, i.e. that

$$\frac{\gamma\bar{\rho}}{\bar{\gamma}\rho_o} A = B e^{i\bar{\gamma}h} - C e^{-i\bar{\gamma}h}. \quad (6.4.7)$$

The solution of equations (6.4.6), (6.4.7) give

$$A = \frac{\hat{F}(\omega)}{\cos(\bar{\gamma}h) - i \left(\frac{\gamma\bar{\rho}}{\bar{\gamma}\rho_o} \right) \sin(\bar{\gamma}h)}. \quad (6.4.8)$$

The substitution of this result into equation (6.4.4) and application of the integral operator (6.4.3) the supplies the acoustic pressure in the water in the form [43]

$$p(\mathbf{x}, t) = \frac{1}{(2\pi)^2} \iint_{-\infty}^{\infty} \frac{\hat{F}(\omega) e^{i(\mathbf{k} \cdot \mathbf{x} + \gamma(x_3 - h) - \omega t)} d^2 \mathbf{k} d\omega}{\cos(\bar{\gamma}h) - i \left(\frac{\gamma\bar{\rho}}{\bar{\gamma}\rho_o} \right) \sin(\bar{\gamma}h)}, \quad x_3 > h. \quad (6.4.9)$$

6.4.3 The far field acoustic pressure

The radiated acoustic power is determined by the far field limit of the pressure determined by equation (6.4.13). In the propagating region at \mathbf{x} ($|\mathbf{x}| \rightarrow \infty$) the integral is dominated by contributions from those wavenumbers \mathbf{k} in the

neighborhood of $(k_1, k_2, \gamma) \simeq k_o \mathbf{x}/|\mathbf{x}|$, and the leading approximation to the integral (the stationary phase approximation [12,40,42,44]) is obtained by expanding the integrand about this point. This gives

$$p(\mathbf{x}, t) \simeq \frac{\cos \theta}{2\pi c_o |\mathbf{x}|} \int_{-\infty}^{\infty} \frac{-i\omega \hat{F}(\omega) e^{-i\omega(t-|\mathbf{x}|/c_o)} d\omega}{\cos(\bar{\gamma}h) - i \left(\frac{\gamma \bar{\rho}}{\bar{\gamma} \rho_o} \right) \sin(\bar{\gamma}h)}, \quad \cos \theta = \frac{x_3}{|\mathbf{x}|}, \quad |\mathbf{x}| \rightarrow \infty, \quad (6.4.10)$$

where the denominator of the integrand is evaluated at $(k_1, k_2, \gamma) = k_o \mathbf{x}/|\mathbf{x}|$. Thus, $\gamma = k_o \cos \theta$ and

$$\bar{\gamma} = \frac{\omega}{\bar{c}_o} f(\omega, \theta),$$

where

$$f(\omega, \theta) = \left[\left(\frac{\bar{c}_o}{c_o} \right)^2 \cos^2 \theta + \left(1 - \frac{\omega^2}{\omega_b^2} - i\eta \frac{\omega}{\omega_b} \right)^{-1} \right]^{1/2} \quad (6.4.11)$$

The term $(\bar{c}_o/c_o)^2 \cos^2 \theta$ in this formula can be neglected except at large frequencies when ω is comparable to $\omega_b(c_o/\bar{c}_o)$. At very low frequencies $f \approx 1$.

Hence, equation (6.4.10) reduces to

$$p(\mathbf{x}, t) \simeq \frac{\cos \theta}{2\pi c_o |\mathbf{x}|} \int_{-\infty}^{\infty} \frac{-i\omega \hat{F}(\omega) e^{-i\omega(t-|\mathbf{x}|/c_o)} d\omega}{\cos \left(\frac{\omega h}{\bar{c}} \right) - i(\mathcal{Z}/f) \cos \theta \sin \left(\frac{\omega h}{\bar{c}} \right)}, \quad |\mathbf{x}| \rightarrow \infty. \quad (6.4.12)$$

where $f \equiv f(\omega, \theta)$.

As $h \rightarrow 0$ the integral representation (6.4.12) reduces to the exact result (6.2.2) in the absence of the bubble layer; similarly both of the approximate representations (6.4.10), (6.4.12) reduce to the corresponding far field approximation (6.2.3). Note also that whereas the radiation in the absence of the bubble layer has the usual dipole directivity, the peak sound radiating in the direction normal to the interface, the corresponding directivity in the presence of the bubble layer is frequency

dependent. In particular at those frequencies at which $\cos(\omega h/\bar{c}) = 0$ it is clear that the radiation directivity becomes omnidirectional. This is because at these frequencies the collective response of the bubbles in the vicinity of the jet impact point produces near resonant volume fluctuations of the layer, which accordingly radiates as a monopole source.

6.4.4 The acoustic pressure frequency spectrum

The definitions (6.2.4), (6.2.5) permit the acoustic pressure frequency spectrum to be cast in the form

$$\Phi_{pp}(\mathbf{x}, \omega) \approx \frac{\cos^2 \theta k_o^2 \Phi_{FF}(\omega)}{4\pi^2 |\mathbf{x}|^2 \left[\cos\left(\frac{\omega h}{\bar{c}} f\right) - i(\mathcal{Z}f) \cos \theta \sin\left(\frac{\omega h}{\bar{c}} f\right) \right]^2}, \quad |\mathbf{x}| \rightarrow \infty. \quad (6.4.13)$$

This reduces to Foley's [1,2] formula (6.2.6) when the nominal thickness of the bubbly interface $h \rightarrow 0$. The non-dimensional Foley spectrum

$$\frac{\Phi_{pp}(\mathbf{x}, \omega) U D^3}{F_o^2 (D/|\mathbf{x}|)^2} \approx \frac{\cos^2 \theta}{2\pi^2} \frac{\alpha(k_o D)^2}{(1 + \epsilon^2(\omega D/U)^2)^{\frac{5}{4}}} \quad (6.4.14)$$

is plotted as the broken line curve (---) in Figure 6.22 for radiation in the normal direction to the interface ($\theta = 0$) in the case

$$U = 27.1 \text{ m/s}, \quad D = 18.6 \text{ mm}, \quad \alpha = 17.28. \quad (6.4.15)$$

The corresponding spectra in the presence of a bubble layer of thickness $h = 10$ mm are plotted as the solid line curves on Figure 6.22 for cases where the mean

bubble resonance frequency $f_b \equiv \omega_b/2\pi = 5, 10, 20, 30, 40$ kHz, and for

$$\bar{c}_o = 100 \text{ m/s}, \quad \bar{\rho} = 980 \text{ kg/m}^3. \quad (6.4.16)$$

All of these spectra exhibit a large peak at $k_o D \approx 0.2$, or at about 2.5 kHz (typically 10-20 dB above the Foley spectrum). This is the fundamental resonance frequency of the 'quarter wave' series

$$\frac{\omega h}{\bar{c}_o} = \frac{\omega_n h}{\bar{c}_o} \equiv \left(n + \frac{1}{2} \right) \pi, \quad n = 0, 1, 2, \dots, \quad (6.4.17)$$

at which $\cos(\omega h/\bar{c}_o) = 0$ for a tube of open length h open at one end (the upper interface at $x_3 = h$ corresponds to the 'closed' end). The only relevant additional peaks in Figure 6.22 correspond to the resonances $n = 1$ and 2 . It is also clear from the figure that propagation through the bubble layer is progressively attenuated at frequencies approaching and exceeding the mean bubble resonance frequency f_b . This eventually cuts off the higher frequency components of the sound that radiate in the absence of bubbles.

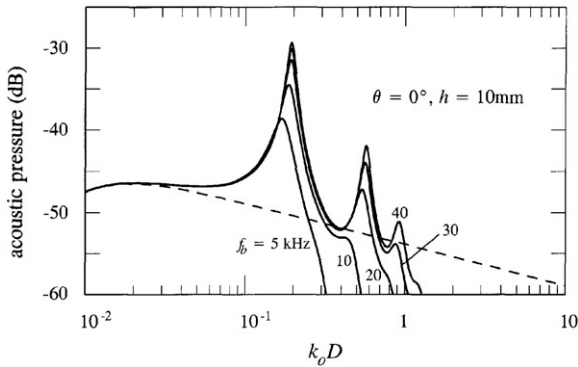


Figure 6.22: The non-dimensional acoustic pressure frequency spectrum. The dashed line is for $h = 0$ and the solid line is for a bubble layer of thickness 0.39".

This very large amplification of the radiated sound by the bubble layer is probably unrealistic, because it is unlikely that the layer will be stable enough to maintain the constant value of h required for a resonant mode to saturate. It is only the relatively slowly varying components of h that are likely to contribute significantly to a resonance-like behavior. The magnitude of such terms can be estimated by averaging the spectrum (6.4.13) with respect to its dependence on h .

The simplest hypothesis is to assume that h is uniformly distributed in probability between, say, zero and a maximum value h_{\max} . The rectified form of the acoustic pressure frequency spectrum (6.4.13) is then obtained by integrating with respect to h over $(0, h_{\max})$ and dividing by h_{\max} . The result can be written as

$$\Phi_{pp}(\mathbf{x}, \omega) \approx \frac{\cos \theta}{4\pi^2 |\mathbf{x}|^2} k_o^2 \Phi_{FF}(\omega) \frac{\Delta(\Omega, \theta)}{\mathcal{Z}}, \quad |\mathbf{x}| \rightarrow \infty, \quad \Omega = \frac{\omega h_{\max}}{\bar{c}_o}, \quad (6.4.18)$$

where

$$\Delta(\Omega, \theta) = \frac{\mathcal{Z} \cos \theta}{h_{\max}} \int_0^{h_{\max}} \frac{dh}{\left[\cos \left(\frac{\omega h}{\bar{c}_o} f \right) - i(\mathcal{Z}/f) \cos \theta \sin \left(\frac{\omega h}{\bar{c}_o} f \right) \right]^2} \quad (6.4.19)$$

The factor $\mathcal{Z} \cos \theta$ before the integral is included because the value of the integral tends to be dominated by contributions from the peaks of the integrand (seen in Figure 6.23) causing its order of magnitude $1/(\mathcal{Z}/\cos \theta)$. Figure 6.23 shows the plot of $\Delta(\Omega, \theta)$ as a function of $\Omega = \omega h_{\max}/\bar{c}_o$ for $h_{\max} = 10$ mm, $\theta = 0^\circ$, and for the mean bubble resonance frequencies $f_b = 5, 10, 20, 30, 40$ kHz.

The function $\Delta(\Omega, \theta)$ turns out to be only weakly dependent on the radiation direction θ when $1 < \Omega < 10$, and peaks roughly at $\omega h_{\max}/\bar{c}_o \approx \pi/2$. In this range the directivity of the rectified acoustic pressure frequency spectrum (6.4.18) is

approximately proportional to $\cos \theta$, which is midway between the dipole obtained by Foley et al [7,8] in the absence of a bubble layer and the omnidirectional monopole that is predicted by Equation (6.4.13) at this quarter-wave resonance frequency for a constant, uniform bubble layer. At lower frequencies $\Delta(\Omega, \theta) \approx \mathcal{Z} \cos \theta$ and Equation (6.4.18) provides a smooth transition from the $\cos \theta$ to $\cos^2 \theta$ dependence of the directivity.

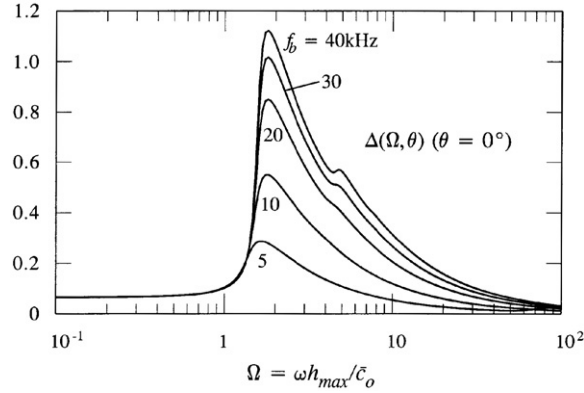


Figure 6.23: Illustrating the variation of $\Delta(\Omega, \theta)$ when $\theta = 0^\circ$, $\bar{\rho} = 980 \text{ kg/m}^3$, $\bar{c}_o = 100 \text{ m/s}$, $h_{\max} = 10 \text{ mm}$ and $f_b = 5, 10, 20, 30, 40 \text{ kHz}$.

Figure 6.24 compares the Foley [7,8] spectrum and the rectified spectrum for radiation in the normal direction ($\theta = 0$) for conditions (6.4.13),(6.4.18) when $h_{\max} = 10 \text{ mm}$ and for bubble resonance frequencies of $f_b = 5, 10, 20, 30, 40 \text{ kHz}$. In all cases there are significant increases in the sound pressure level in the range $0.1 < k_o D < 1$ as large as 10 dB when f_b exceeds 20 kHz. At higher frequencies the bubble layer causes the levels to fall rapidly below that in the absence of bubbles. For the range of frequencies illustrated in Figure 6.24 the high frequency decay is $\Phi_{pp}(\mathbf{x}, \omega) \approx (k_o D)^{-3/2}$.

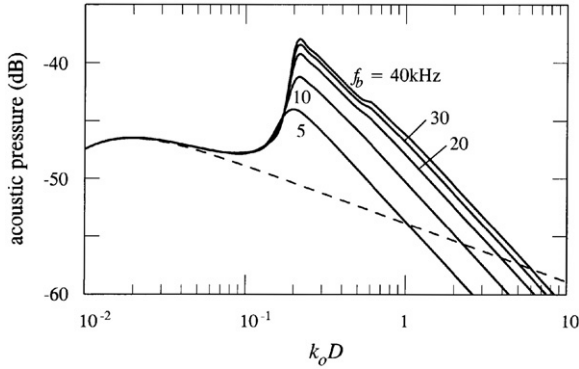


Figure 6.24: The non-dimensional acoustic pressure frequency spectrum in the normal direction $\theta = 0$ and conditions (6.4.16),(6.4.18). The dotted line represents Foley's spectrum [7,8] for $h = 0$. The solid lines are of the rectified acoustic spectrum for $h_{\max} = 10$ mm and $f_b = 5, 10, 20, 30, 40$ kHz.

6.5 Conclusions

The motivation behind these mathematical models came from observations of bubble entrainment due to gas jets impacting a free air-water interface. The resulting model predicts that the radiated sound will exhibit a dipole radiation pattern, with or without a bubbles at the interface. At a range of frequencies, the acoustic spectrum is increased by 10-30 dB. At higher frequencies which have wavelengths that are on the same length scale of the mean cloud radius R or bubble layer thickness h , the sound power is predicted to be lower than in the absence of bubbles.

The sum of the measured unsteady force spectrums from all the force sensors were used as an input to Foley's acoustic model. The predicted levels were generally about 15 dB below the measured acoustic spectrum. This indicates that the current acoustic model is not representing all of the energy transmitted through the air-water interface. Some of this could be in-air jet noise transmitting directly

through the interface. The inaccuracy in the model could also stem from the assumption that the jet impact area can be idealized as a delta function. In reality, the jet impacts the surface over a finite area that could lead to contributing sources over the whole impact area.

Finally, the sum of the measured unsteady force spectrums from all the force sensors were used as an input to the bubble hemisphere model. The predicted levels for the 1/16" nozzle was about 20 dB below the measured levels for most of the spectrum. While the overall levels are lower, the shape of the model matches the measured spectrum. The predicted levels for the 1/8" nozzle was about 10 dB below the measured levels over most of the spectrum. Again, the overall predicted levels were lower, but the shape of the model matches the measured data. There are a few possible explanations for this discrepancy. The in-air jet noise transmitted directly through the interface is not accounted for in the model. Also certain parameters, such as the void fraction and bubble size within the bubble hemisphere were estimated. This would effect the sound speed within the bubble hemisphere, and would change the predicted level of the model. Direct measurement of the composition of the bubble cloud, including the void fraction and bubble size, could improve the quality of the bubble model.

Chapter 7

Conclusions

This chapter acts as a link between the work performed in this investigation and future research. Section 7.1 summarizes the contents of this thesis along with the most important results. Section 7.2 provides recommendations to vehicle designers for reducing the self noise of supercavitating vehicles. Finally, Section 7.3 discusses the questions brought up by this study, and proposes some future experiments.

7.1 Summary

This thesis describes the investigation into the self noise from a ventilated supercavitating vehicle. This problem was approached analytically and experimentally. Chapter 2 extended Foley's original theory and derived acoustic models for sound traveling through the air-water interface in the presence of either a bubbly layer or hemisphere. Chapter 3 discussed measurements of the gas jet system to be used in later experiments. It was important to understand the flow properties and radiated noise of the jet system. This turned out to be the major sources of uncertainty in later experiments. Chapter 4 described the measurements of the unsteady force spectrum of a gas jet hitting a rigid wall. These results were compared to measurements taken by Foley. The spectrums measured in this experiment were

similar to those measured by Foley, but with less noise. Chapter 5 outlined the acoustic measurements of gas jets hitting the air-water interface with no bubble entrainment. This experiment matches with the original acoustic model developed by Foley. The measured force data was used as an input to Foley's model, but the predicted levels were much lower than those measured. The relationship between jet exit velocity and acoustic pressure levels was also explored in this chapter. This led to the observation that the acoustic pressure level is also dependent on the jet impact area at the surface. Gas jets with larger impact areas on the air-water interface had a higher slope power law. Chapter 6 described the acoustic pressure spectrum measurements for the bubble entrainment cases. Observed dimensions of the entrained bubble clouds were used as inputs to the acoustic model developed in Chapter 2. The acoustic model predicted an amplification in acoustic signal over a range of frequencies that was verified by the measured data.

7.2 Recommendations to reduce self noise

The most important factor in the self noise due to the ventilation system of supercavitiating vehicles is the exit velocity of the gas jets. Higher velocity jets lead to higher radiated noise (Figures 4.4-4.6, Section 4.3.1). A relationship between the size of the jet impact area and radiated noise was also discovered. Larger diameter jet impact areas are more sensitive to changes in exit velocity (Section 4.3.1). It seems that the best solution would be to vent the minimum amount of gas to produce a stable cavity around the vehicles. It was shown that in-air tones from the ventilation system could be transmitted through the air-water interface (Section 4.2.2). Detailed in-air measurements of the ventilation system would be advisable.

It would be a good idea to keep the ventilation flow as smooth as possible to eliminate this self noise (Section 2.3.2). It has also been shown that the existence of bubbles can increase an acoustic signal (Equations 6.3.15 and 6.3.16, Figures 6.16, 6.19, 6.20). Therefore any ventilation strategies that visibly produces bubbles at the interface should be avoided if possible. But in a realistic saltwater environment, the complete elimination of bubbles near a high speed underwater vehicle is impossible.

7.3 Recommendations of future work

The main recommendation from this thesis would be to study the interactions of gas jets with deflector plates above the air-water interface. This topic was just beyond the scope of this investigation to fully cover. But interesting analytical predictions about the influence of a deflector were derived. Begin by writing the outgoing acoustic pressure in terms of the Fourier integral

$$p(\mathbf{x}, t) = \int \int_{-\infty}^{\infty} \hat{p}(\mathbf{k}, \omega) e^{i(\mathbf{k} \cdot \mathbf{x} + \gamma x_3 - \omega t)} d^2 \mathbf{k} d\omega \quad (7.3.1)$$

where $\mathbf{k} = (k_1, k_2, 0)$ and $\hat{p}(\mathbf{k}, \omega)$ is the space-time Fourier transform of the pressure perturbation on the interface $x_3 = 0$. This can be rearranged to form

$$\hat{p}(\mathbf{k}, \omega) = \frac{1}{(2\pi)^3} \int \int_{-\infty}^{\infty} F(t) \delta(x_1) \delta(x_2) e^{-i(\mathbf{k} \cdot \mathbf{x} - \omega t)} dx_1 dx_2 dt = \frac{\hat{F}(\omega)}{(2\pi)^2} \quad (7.3.2)$$

with $\gamma = (\omega^2/c_o^2 - k^2)^{\frac{1}{2}}$. The radiation condition is satisfied by requiring $(\omega^2/c_o^2 - k^2)^{\frac{1}{2}}$ to have the same sign as ω when $\omega^2/c_o^2 > k^2$ and to be positive imaginary for other

real values of \mathbf{k} . Therefore

$$p(\mathbf{x}, t) = \frac{1}{(2\pi)^2} \int \int_{-\infty}^{\infty} \hat{F}(\omega) e^{i(\mathbf{k} \cdot \mathbf{x} + \gamma x_3 - \omega t)} d^2 \mathbf{k} d\omega, x_3 > 0. \quad (7.3.3)$$

In the far field at $\mathbf{x}(|\mathbf{x}| \rightarrow \infty)$ the wavenumber integral is dominated by the region near $(k_1, k_2, \gamma) = k_o \mathbf{x}/|\mathbf{x}|$, and the leading approximation to the integral (the 'stationary phase approximation') is obtained by expanding the integrand about this point, yielding

$$p(\mathbf{x}, t) \approx \frac{\cos \theta}{2\pi c_o |\mathbf{x}|} \int_{-\infty}^{\infty} -i\omega \hat{F}(\omega) e^{-i\omega(t-|\mathbf{x}|/c_o)} d\omega, |\mathbf{x}| \rightarrow \infty \quad (7.3.4)$$

This implies that $\hat{p}(\mathbf{x}, \omega) \approx -i\omega \hat{F}(\omega) e^{i\omega|\mathbf{x}|/c_o} \cos \theta / (2\pi c_o |\mathbf{x}|)$ when $|\mathbf{x}| \rightarrow \infty$, which leads back to Foley's original theory [7,8].

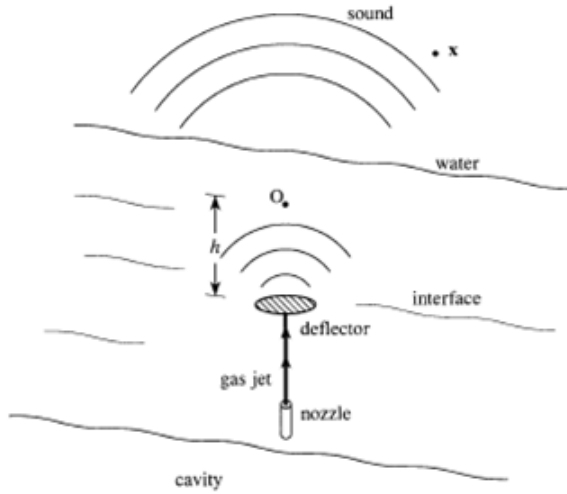


Figure 7.1: Diagram of gas jet interacting with a deflector plate normal to the interface.

Next consider the case in which a rigid deflector plate has been placed between the jet and the water at distance h from the surface, as shown in Figure 7.1. In

a first approximation it may be assumed that the unsteady force experienced at the plate is the same as that $F(t)$ produced by impingement on the gas-water interface. The impact with the plate generates dipole aerodynamic sound. The direct radiation p_d within the cavity is given by Curle's formula

$$p_d = \frac{\partial}{\partial x'_3} \left[\frac{1}{4\pi|\mathbf{x}'|} F \left(t - \frac{|\mathbf{x}'|}{c_1} \right) \right] \quad (7.3.5)$$

where $\mathbf{x}' = (x_1, x_2, x_3 - h)$ and c_1 is the speed of sound within the cavity. In the region $0 < x'_3 < h$ between the deflector and the interface the result (7.2.5) can also be expressed in the following manner corresponding to equation (7.2.3):

$$\frac{1}{(2\pi)^2} \int \int_{-\infty}^{\infty} \frac{1}{2} \hat{F}(\omega) e^{i(\mathbf{k} \cdot \mathbf{x}' + \gamma' x'_3 - \omega t)} d^2 \mathbf{k} d\omega, x'_3 > 0, \quad (7.3.6)$$

where $\gamma' = (\omega^2/c_1^2 - k^2)^{\frac{1}{2}}$. The incidence on the interface $x_3 = h$ of the acoustic pressure p_d produces (to first order) a reflected wave of equal amplitude and phase. The Fourier transform of the net interface pressure is therefore

$$\hat{p}(\mathbf{k}, \omega) = \frac{\hat{F}(\omega) e^{i\gamma' h}}{(2\pi)^2} \quad (7.3.7)$$

The analogues of equations (7.2.2) and (7.2.3) accordingly yield the acoustic pressure in the water in the form

$$p(\mathbf{x}, t) = \frac{1}{(2\pi)^2} \int \int_{-\infty}^{\infty} \hat{F}(\omega) e^{i(\mathbf{k} \cdot \mathbf{x} + \gamma x_3 + \gamma' h - \omega t)} d^2 \mathbf{k} d\omega \quad (7.3.8)$$

which can be approximated as

$$p(\mathbf{x}, t) \approx \frac{\cos \theta}{2\pi c_o |\mathbf{x}|} \int_{-\infty}^{\infty} -i\omega \hat{F}(\omega) e^{-i\omega(t-|\mathbf{x}|/c_o) + i\omega h \left(\frac{1}{c_1^2} - \frac{\sin^2 \theta}{c_o^2} \right)^{\frac{1}{2}}} d\omega, |\mathbf{x}| \rightarrow \infty, x_3 > 0 \quad (7.3.9)$$

so that

$$\hat{p}(\mathbf{x}, \omega) \approx \frac{-i\omega \hat{F}(\omega) \cos \theta}{2\pi c_o |\mathbf{x}|} e^{i\omega |\mathbf{x}|/c_o + i\omega h \left(\frac{1}{c_1^2} - \frac{\sin^2 \theta}{c_o^2} \right)^{\frac{1}{2}}} \quad (7.3.10)$$

Because $\frac{1}{c_1^2} > \frac{\sin^2 \theta}{c_o^2}$, it follows that the acoustic pressure is given by

$$\Phi_{pp}(\mathbf{x}, \omega) \approx \frac{\cos^2 \theta}{4\pi^2 |\mathbf{x}|^2} k_o^2 \Phi_{FF}(\omega), |\mathbf{x}| \rightarrow \infty \quad (7.3.11)$$

This is the same result as if the jet were to be impinging directly on the interface.

Next consider a deflector plate oriented within a cavity that is oriented so that its outward normal is in the forward direction, as shown in Figure 7.2.

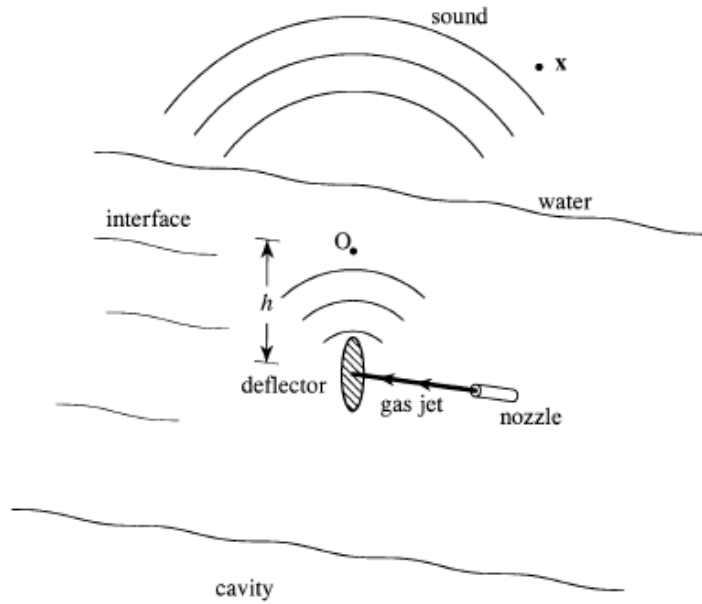


Figure 7.2: Diagram of gas jet interacting with a deflector in a cavity oriented in the forward direction.

The dipole source at the deflector is parallel to the x_2 direction of Figure 7.1, and equations (7.2.9) and (7.2.10) become

$$p(\mathbf{x}, t) = \frac{1}{(2\pi)^2} \int \int_{-\infty}^{\infty} \frac{k_1 \hat{F}(\omega)}{\gamma'(\mathbf{k})} e^{i(\mathbf{k} \cdot \mathbf{x} + \gamma x_3 + \gamma' h - \omega t)} d^2 \mathbf{k} d\omega \quad (7.3.12)$$

$$p(\mathbf{x}, t) \approx \frac{x_2 x_3}{2\pi c_o |\mathbf{x}|^3 \sqrt{(c_o/c_1)^2 - \sin^2 \theta}} \int_{-\infty}^{\infty} -i\omega \hat{F}(\omega) e^{-i\omega(t - |\mathbf{x}|/c_o) + i\omega h \left(\frac{1}{c_1^2} - \frac{\sin^2 \theta}{c_o^2} \right)^{\frac{1}{2}}} d\omega, |\mathbf{x}| \rightarrow \infty, x_3 > 0. \quad (7.3.13)$$

Therefore

$$\Phi_{pp}(\mathbf{x}, \omega) \approx \frac{(x_2 x_3)^2}{4\pi^2 |\mathbf{x}|^6 \left(\frac{c_o^2}{c_1^2} - \sin^2 \theta \right)} k_o^2 \Phi_{FF}(\omega), |\mathbf{x}| \rightarrow \infty \quad (7.3.14)$$

The sound speed ratio $c_o/c_1 \approx 5$. The acoustic pressure spectrum in the water is therefore reduced by about $10 \times \log_{10}(25) \approx 14$ dB compared to a deflector oriented out to the interface. Taking in air measurements of gas jets impinging on deflector plates at various angles would be a good start towards understanding this interaction. The next step would be to take underwater measurements of gas jets hitting a deflector plate above the interface.

Improved measurements of the composition of the bubble hemisphere would likely improve the quality of the bubble hemisphere model. This would include direct measurements of the void fraction and bubble size within the bubble hemisphere. It would also be interesting to study the indentations of the low speed gas jets hitting the air-water interface. In these experiments, the water was still. If the water were moving at a steady rate, the indentation might shear off and entrain bubbles. This could potentially produce a layer of bubbles near the interface. It could be useful to determine the minimum indentation size necessary to entrain bubbles in moving water.

Appendix A

Review of select topics in linear acoustics

This appendix summarizes some of the fundamentals of acoustic theory related to this dissertation. Material is taken from Blackstock[45], Howe[12], and Pierce[44]. See these references for greater detail on each topic or a more general review of the principles of linear acoustics.

A.1 The linear wave equation

The acoustic wave equation is derived from the conservation and constitutive equations which describe a fluid. We consider a fluid volume V defined by a surface S in which body forces and thermal and viscous effects are negligible. The fluid inside the volume has velocity $\mathbf{u}(\mathbf{x}, t)$, pressure $P(\mathbf{x}, t)$, and density $\rho(\mathbf{x}, t)$ at a position $\mathbf{x} = (x_1, x_2, x_3)$ and time t .

Conservation of mass requires that the increase of mass inside V must be equal to the influx of mass through S . This is expressed by the continuity equation

$$\frac{D\rho}{Dt} + \rho \nabla \cdot \mathbf{u} = 0$$

where the material derivative $D/Dt = \partial/\partial t + \mathbf{u} \cdot \nabla$.

Conservation of momentum holds that the time rate of change of momentum inside V is equal to the sum of all forces acting on the fluid volume and the momentum flux through the surface S . Neglecting body and viscous forces, momentum conservation can be expressed by

$$\rho \frac{D\mathbf{u}}{Dt} + \nabla P = 0$$

Finally we require an equation of state, a relationship between thermodynamic variables. We will assume that our fluid volume is isentropic, the entropy s in the volume is constant.

$$P = P(\rho)$$

We consider that the pressure P and density ρ can be decomposed into a mean, or static, and excess constituent such that

$$P = p_o + p$$

$$\rho = \rho_o + \delta\rho$$

where p_o and ρ_o are respectively the mean pressure and density in the fluid volume $\delta\rho$ is the excess density, and p is the acoustic pressure. This leads to the Taylor expansion of the equation of state

$$P = p_o + A \frac{\rho - \rho_o}{\rho} + \frac{B}{2!} \left(\frac{\rho - \rho_o}{\rho_o} \right)^2 + \dots$$

where A, B , etc. are empirically determined coefficients. Introduce the sound speed c in the fluid defined by

$$c^2 = \frac{dP}{d\rho} = \frac{A}{\rho_o} + \frac{B}{\rho_o} \frac{\rho - \rho_o}{\rho_o} + \dots$$

Letting $\rho \rightarrow \rho_o$, we find that c becomes a constant c_o and that $A = \rho_o c_o^2$. Substitute for p and ρ to get the equation of state

$$p = c_o^2 \delta\rho \left(1 + \frac{B}{2!A} \frac{\delta\rho}{\rho_o} + \dots \right)$$

To simplify these equations, we first observe that the changes in the fluid properties due to sound energy are small. In a quiet fluid, $P = p_o, \rho = \rho_o$, and $\mathbf{u} = 0$ across V . We also assume that the fluid is homogeneous with constant pressure and density across the volume. When sound is introduced the excess pressure, density, and induced particle velocity are very small compared to their static values

$$\delta\rho \ll \rho$$

$$|p| \ll \rho_o c_o^2$$

$$|u| \ll c_o$$

Substitute for P and ρ and expand the continuity equation as

$$\frac{\partial}{\partial t}(\delta\rho) + u \nabla \delta\rho + \rho_o \nabla \cdot \mathbf{u} + \delta\rho \nabla \cdot \mathbf{u} = 0$$

Considering our small value approximations, we note that the second and fourth terms on the left hand side above are an order of magnitude smaller than the first

and third. Eliminating them leads to the linearized continuity equation

$$\frac{\partial}{\partial t}(\delta\rho) + \rho_o \nabla \cdot \mathbf{u} = 0$$

Next apply the same procedure to the conservation of momentum equation.

$$\rho_o \frac{\partial \mathbf{u}}{\partial t} + \rho_o \mathbf{u} \cdot \nabla \mathbf{u} + \delta\rho \frac{\partial \mathbf{u}}{\partial t} + \delta\rho \mathbf{u} \cdot \nabla \mathbf{u} + \nabla p = 0$$

As before, keep only the first and third terms of the series. The linearized conservation of momentum equation is

$$\rho_o \frac{\partial \mathbf{u}}{\partial t} + \nabla p = 0$$

The equation of state is linearized to

$$p = c_o^2 \delta\rho$$

Use this to eliminate δp from the continuity equation

$$\frac{1}{c_o^2} \frac{\partial p}{\partial t} + \rho_o \nabla \cdot \mathbf{u} = 0$$

Taking the difference of the time derivative of this equation with the spatial derivative of the linearized momentum equation results in the linear acoustic wave equation

$$\left(\frac{1}{c_o^2} \frac{\partial^2}{\partial t^2} - \nabla^2 \right) p = 0$$

It is often convenient to consider sound transmission in the frequency domain rather than the time domain. The wave equation is brought into the frequency spectrum

by applying a Fourier transform, which gives the Helmholtz equation

$$(k_o^2 + \nabla^2)p = 0$$

where the acoustic wavenumber $k_o = \omega/c_o$ and ω is angular frequency. Next consider a fluid volume that contains an acoustic source. The source can be considered to add a volume source to the right side of the continuity equation and a force term to the right side of the momentum equation. Carrying these terms through the derivation yields

$$\left(\frac{1}{c_o^2} \frac{\partial^2}{\partial t^2} - \nabla^2 \right) p = F(\mathbf{x}, t)$$

where the volume and force terms have been replaced by a generalized pressure source $F(\mathbf{x}, t)$. This result is called the inhomogeneous wave equation.

In general, the solution of the wave equation and Helmholtz equation can be decomposed into an outgoing and incoming wave. At time $t = 0$ an acoustic source begins to generate sound in the fluid. Causality requires that for $t > 0$ the wave energy radiates outward, and in the absence of other sources or bodies, there is no incoming energy. The consideration that all incoming solutions of the wave equation must be zero is called the radiation condition.

A.2 Acoustic impedance, intensity, and power

Acoustic impedance quantifies the sound absorption of a fluid, It is defined as the ratio of acoustic pressure to particle velocity in the medium. For an outgoing wave,

the characteristic impedance Z_o is given as

$$Z_o = \frac{p}{u} = \rho_o c_o$$

A medium is considered acoustically rigid if its impedance $Z \rightarrow \infty$. A normally incident plane wave traveling through a medium of impedance Z_1 is reflected back entirely when it reaches a medium of impedance Z_2 when $Z_1 \ll Z_2$. If $Z_1 \gg Z_2$, there is again no transmission. The reflective wave identically cancels the incident wave and the interface is known as a pressure release surface, because the acoustic pressure p is zero at the interface. When the impedance $Z \rightarrow 0$ the medium is considered acoustically compliant.

Acoustic intensity is the time average of sound energy flow through a unit area in the direction normal to that area. In integral form, acoustic intensity I is

$$I = \frac{1}{t_{av}} \int_0^{t_{av}} p \mathbf{u} dt$$

The directivity of radiated sound is the directional dependence of the acoustic intensity. For sound radiating omnidirectionally, intensity on a spherical surface of radius r simplifies to a scalar quantity

$$I = \frac{p(r)^2}{\rho_o c_o}$$

The acoustic power W passing through a surface S is the integral of the sound intensity over that surface

$$W = \int_S I dS'$$

where S' is a differential element of the surface S . For omnidirectional sound, the power through a sphere of radius r is

$$W = 4\pi r^2 I$$

A.3 Acoustic compactness and the near and far fields

An acoustic source occupying a fluid region of characteristic dimension l and angular frequency ω radiates sound of wavelength $2\pi c_o/\omega$. The source is considered to be acoustically compact when l is much smaller than this wavelength, or $\omega l/c_o \equiv k_o l \ll 1$. The acoustic far field exists at point $|\mathbf{x}|$ many wavelengths from the source where $k_o |\mathbf{x}| \gg 1$. The acoustic near field is the region in the immediate vicinity of the source where $k_o \leq 1$.

A.4 Monopoles, dipoles, and quadrupoles

A monopole is an acoustic source which can be considered analogous to a pulsating sphere. Sound radiates from the source omnidirectionally, diminishing in the far field (as $|\mathbf{x}| \rightarrow \infty$) like $1/|\mathbf{x}|$. A general expression for a monopole is a source of the form $q(t)\delta(\mathbf{x})$, where $q(t)$ is the strength of the source.

A dipole is a source of the form

$$\frac{\partial}{\partial x_j} [f_j(t)\delta(\mathbf{x})]$$

with strength $f_j(t)$. A dipole is analogous to an oscillating sphere. Sound emanates from the source as two lobes protruding in the direction of that os-

cillation as shown in Figure A.1, diminishing as $1/|\mathbf{x}|^2$ in the far field. A point dipole is also equivalent to two monopoles of opposite strength a short distance apart.

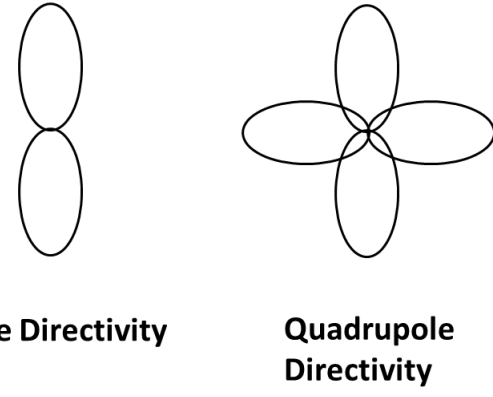


Figure A.1: Directivity of the sound from a dipole and quadrupole source.

A source distribution equivalent to four monopoles with net strength zero is called a quadrupole. A quadrupole source is expressed as

$$\frac{\partial^2 T_{ij}}{\partial x_i \partial x_j}(\mathbf{x}, t)$$

and diminishes in the far field as $1/|\mathbf{x}|^3$. The directivity of a quadrupole is shown in Figure A.1.

An acoustic source can be represented as the sum of component sources of monopole, dipole, and quadrupole strength. Typically it is necessary only to consider the leading order term in determining the radiated acoustic pressure generated by the source.

Appendix B

Acoustic Green's function

This appendix discusses the use of acoustic Green's functions as solutions to the inhomogeneous wave equation. The material is taken from Howe's *Acoustics of Fluid Structure Interactions*[12] and *Theory of Vortex Sound*[46].

The free space Green's function is the outgoing solution of the wave equation generated by the point source $\delta(\mathbf{x} - \mathbf{y})\delta(t - \tau)$ in an unbounded fluid located at the point $x = y$ and at time $t = \tau$.

$$\left(\frac{1}{c_o^2} \frac{\partial^2}{\partial t^2} - \nabla^2 \right) G = \delta(\mathbf{x} - \mathbf{y})\delta(t - \tau)$$

where $G = 0$ for $t < \tau$. This has the solution

$$G(\mathbf{x}, \mathbf{y}, t - \tau) = \frac{1}{4\pi|\mathbf{x} - \mathbf{y}|} \delta\left(t - \tau - \frac{|\mathbf{x} - \mathbf{y}|}{c_o^2}\right)$$

The inhomogeneous wave equation

$$\left(\frac{1}{c_o^2} \frac{\partial^2}{\partial t^2} - \nabla^2 \right) p = F(\mathbf{x}, t)$$

describes the behavior of waves generated by a distributed source $F(\mathbf{x}, t)$. This source can be regarded as an array of point sources, such that

$$F(\mathbf{x}, t) = \int \int_{-\infty}^{\infty} F(\mathbf{y}, \tau) \delta(\mathbf{x} - \mathbf{y}) \delta(t - \tau) d^3 \mathbf{y} d\tau$$

The solution for each constituent source of strength $F(\mathbf{y}, \tau) \delta(\mathbf{x} - \mathbf{y}) \delta(t - \tau) d^3 \mathbf{y} d\tau$ is $F(\mathbf{y}, \tau) G(\mathbf{x}, \mathbf{y}, t - \tau) d^3 \mathbf{y} d\tau$. Add these individual contributions to obtain

$$\begin{aligned} p(\mathbf{x}, t) &= \int \int_{-\infty}^{\infty} F(\mathbf{y}, \tau) G(\mathbf{x}, \mathbf{y}, t - \tau) d^3 \mathbf{y} d\tau \\ p(\mathbf{x}, t) &= \frac{1}{4\pi} \int \int_{-\infty}^{\infty} \frac{F(\mathbf{y}, \tau)}{|\mathbf{x} - \mathbf{y}|} \delta \left(t - \tau - \frac{|\mathbf{x} - \mathbf{y}|}{c_o^2} \right) d^3 \mathbf{y} d\tau \\ p(\mathbf{x}, t) &= \frac{1}{4\pi} \int_{-\infty}^{\infty} \frac{F(\mathbf{y}, t - \frac{|\mathbf{x}-\mathbf{y}|}{c_o^2})}{|\mathbf{x} - \mathbf{y}|} d^3 \mathbf{y} \end{aligned}$$

Green's functions can be applied to more general acoustic problems involving solid or fluid boundaries, and have equivalent expressions in the time and frequency domains. The use of the Green's function will be demonstrated by solving the inhomogeneous Helmholtz equation. Consider an acoustic source on the boundary of a volume of fluid defined by some surface S . The source generates acoustic pressure $p(\mathbf{x}, \omega)$ within the fluid volume which satisfies

$$(\nabla^2 + k_o^2)p = 0$$

subject to the boundary condition $p = p'(\mathbf{x}, \omega)$ on S . Introduce a Green's function $G(\mathbf{x}, \omega)$ with outgoing wave behavior

$$(\nabla^2 + k_o^2)G = 0$$

with the boundary condition $G = G'(\mathbf{x}, \omega)$ on S . Taking the difference of G and p

$$p\nabla^2G - G\nabla^2p = 0$$

Integrating over the fluid volume V ,

$$\int_V (p\nabla^2G - G\nabla^2p)dV = 0$$

Introduce the vector identities

$$p\nabla^2G = \nabla^2(pG) - \nabla \cdot (G\nabla p) - \nabla G \cdot \nabla p$$

$$G\nabla^2p = \nabla^2(Gp) - \nabla \cdot (p\nabla G) - \nabla p \cdot \nabla G$$

into the integrand

$$\int_V [\nabla \cdot (p\nabla G) - \nabla \cdot (G\nabla p)]dV = 0$$

Applying the divergence theorem reduces this to

$$\int_V [\nabla \cdot (p\nabla G) - \nabla \cdot (G\nabla p)]dV = \oint_S \left[p \frac{\partial G}{\partial x_n} - G \frac{\partial p}{\partial x_n} \right] dS = 0$$

where x_n is the vector outward normal to the surface S . The acoustic pressure p is then solved for by substitution into the integrand of the Green's function G and the boundary conditions on S specific to the problem's geometry and source parameters.

Appendix C

Equipment specifications

This appendix summarizes the important characteristics of the sensors used in this study.

C.1 Flow rate sensor, Sierra 824 Top-Trak Mass Flow Meter

Mass flow rate range: 0 to 50 slpm

Power requirements: 12-15 VDC nominal, 100 mA maximum

Accuracy: $\pm 1.5\%$ of full scale

Output signal: 0-5 VDC

C.2 Pressure sensor, Omega PX209 Pressure Transducer

Pressure range: 0-60 psi

Power requirements: 12-15 VDC

Accuracy: $\pm 0.25\%$

Output signal: 0-5 VDC

C.3 Temperature sensor, Omega SCASS-1256-6 Thermocouple

Temperature range: 0 – 220° C

Power requirements: 12-15 VDC

Accuracy: $\pm 1^\circ$ C

Output signal: 0-5 VDC

C.4 In air microphone, Brüel and Kjaer 4938 Series Microphone

Dynamic range: 30-172 dB

Sensitivity: 16 mV/Pa

C.5 Unsteady force transducers, PCB Piezotronics 208C01 and 208A11 Dynamic Force Sensors

Force input range: 0-10 lbs

Power requirements: 20-30 VDC with constant current of 2-20 mA

Sensitivity: 500 mV/lb

Accuracy: $\pm 1 \%$

Output signal: 0-5 VDC

Internal resonance frequency: 32 kHz

C.6 Hydrophones, G.R.A.S. 10CC Hydrophone

Frequency range: 5Hz-120kHz

Sensitivity: -170 dB re 1 V/ μ Pa

Appendix D

Bibliography

- [1] A. W. Foley, M. S. Howe and T. A. Brungart, Sound generated by gas-jet impingement on the interface of a supercavity. *Proceedings of IMECE2008, 2008 ASME International Mechanical Engineering Congress and Exposition*, November 2-6, 2008, Boston MA, USA.
- [2] A. W. Foley, *Investigations of the sound generated by supercavity ventilation*, PhD thesis, Boston University Department of Mechanical Engineering, 2009.
- [3] J. P. Franc and J. M. Michel, *Fundamentals of Cavitation*, Kluwer Academic Publishers, Dordrecht (2004).
- [4] G. Birkhoff and E. H. Zarantonello. *Jets, Wakes, and Cavities*. Academic Press Inc., 1957.
- [5] R. T. Knapp, J. M. Daily, and F. G. Hammitt. *Cavitation*. McGraw-Hill, Inc., 1970.
- [6] C. E. Brennen, *Cavitation and bubble dynamics*. Oxford University Press (1995).
- [7] R. Kuklinski, C. Henoch, C. and J. Castano, Experimental study of ventilated cavities on dynamic test model. Paper presented at *Cav2001: Session B3.004* (2001).

- [8] E. Silberman and C. S. Song, Instability of ventilated cavities. *Journal of Ship Research* **5**(1) (1961), 13 - 33.
- [9] C. S. Song, Pulsation of ventilated cavities. *J. Ship Research* **5**(4) (1962), 8 - 20.
- [10] R. S. Scorer. *Natural Aerodynamics*. Pergamon Press, Oxford, 1958.
- [11] W. K. Blake, *Mechanics of flow-induced sound and vibration*, New York: Academic Press, 1986.
- [12] M. S. Howe, *Acoustics of Fluid-Structure Interactions*, Cambridge University Press, 1998.
- [13] M. S. Howe. Surface pressure and sound produced by turbulent pressure release edge flow, 1998. Applied Research Laboratory TM 98-148.
- [14] M. J. Lighthill. On sound generated aerodynamically. Part 1: General theory. *Proceedings of the Royal Society of London* **211** 564-587, 1952.
- [15] S. D. Young, T. A. Brungart, G. C. Lauchle, and M. S. Howe, Effect of a downstream ventilated gas cavity on the spectrum of turbulent boundary layer wall pressure fluctuations, *Journal of the Acoustical Society of America* **118**, 3506 - 3512, 2005.
- [16] A. W. Foley, M. S. Howe and T. A. Brungart, Spectrum of the sound produced by a jet impinging on the gas-water interface of a supercavity. *Journal of Sound and Vibration* **329** (2010) 415 - 424.
- [17] M. S. Howe, A. M. Colgan and T. A. Brungart, On self noise at the nose of a supercavitating vehicle. *Journal of Sound and Vibration* **322** (2009) 772 - 784.
- [18] M. C. Junger and D. Feit, *Sound, Structures and their Interactions*, Acoustical Society of America, New York, 1993).

- [19] M. S. Howe. Sound produced by a vortex interacting with a cavitated wake. *Journal of Fluid Mechanics* **543** 333-347, 2005.
- [20] J. E. Ffowcs Williams. Sound production at the edge of a steady flow. *Journal of Fluid Mechanics* **66** 791-816, 1974.
- [21] C. M. Ho and N. S. Nossier. Dynamics of an impinging jet. Part 1. The feedback phenomenon. *Journal of Fluid Mechanics* **105** 119-142, 1981.
- [22] W. Peng and D. E. Parker. An ideal fluid impinging on an uneven surface. *Journal of Fluid Mechanics* **333**, 231-255, 1997.
- [23] J. M. Vanden-Broeck. Deformation of a liquid surface by an impinging gas jet. *SIAM Journal of Applied Mathematics* **41** (2) 306-309, 1981.
- [24] L. Y. Kuo and A. P. Dowling. Acoustics of a two dimensional compact jet impinging normally onto a flat plate. *Journal of Fluid Mechanics* **414**, 251-284, 2000.
- [25] W. A. Olsen, J. H. Miles, and R. G. Dorsch. Noise generated by the impingement of a jet upon a large flat board. Technical Report TN D-7075, NASA, 1972.
- [26] J. Shen and W. L. Meecham. Quadrupole directivity of jet noise associated when impinging on normal plates. *Journal of the Acoustical Society of America* **94**, 1415-1424, 1993.
- [27] D. R. Strong, T. E. Siddon, and W. T. Chu. Pressure fluctuation on a flat plate with oblique jet impingement. Technical Report CR-839, NASA, 1967.
- [28] J. O. Hinze. *Turbulence*. McGraw-Hill, New York, Second Edition, 1975.
- [29] A. B. Wood, *A Textbook of Sound*, G. Bell and Son Ltd., London 1932.

- [30] M. Minnaert, On musical air bubbles and the sounds of running water. *Philosophical Magazine* S.7, 16 (1933) 235-249.
- [31] C. Devin. Survey of thermal, radiation, and viscous damping of pulsating air bubbles in water. *Journal of the Acoustical Society of America* **31**, 1654-1667, 1959.
- [32] F. E. Fox, S. R. Curley and G. S. Larson, Phase velocity and absorption measurements in water containing air bubbles. *Journal of the Acoustical Society of America* **27** (1995) 534-539.
- [33] J. Nystuen, C. McGlothin, M. Cook, The Underwater Sound Generated By Heavy Rainfall, *Journal of Acoustical Society of America* 93 (6) June 1993, 3169-3177.
- [34] G. J. Orris and M. Micholas. Collective oscillations of fresh and salt water bubble plumes. *Journal of the Acoustical Society of America* **107** (2), 771-787, 2000.
- [35] M. S. Howe, N. A. A. Hagen, On the impact of a drop falling on water, *Journal of Sound and Vibration*, 330 (2011), 625-635.
- [36] W. M. Carey, J. W. Fitzgerald, Low frequency noise and bubble plume oscillations, Presented at the *114th Meeting of the Acoustical Society of America*, November 16-20 1987, Miami, FL.
- [37] F. M. White, *Fluid Mechanics 4th Edition*, Boston: McGraw Hill, 1998.
- [38] L. van Wijngaarden, Sound and Shock Waves in Bubbly Liquids, *Cavitation and Inhomogeneities in Underwater Acoustics*, Springer-Verlag, New York (1980) 127-140.
- [39] D. G. Crighton and J. E. Ffowcs Williams, Sound generation by turbulent two-phase flow. 1969 *Journal of Fluid Mechanics* **36** (1969) 585-603.

- [40] G. K. Batchelor, Compression waves in a suspension of gas bubbles in liquid. 1969 *Fluid Dynamics Transactions* **4**(1969) 425-445.
- [41] M. Abramowitz and I. A. Stegun, (editors) *Handbook of Mathematical Functions* (Ninth corrected printing), US Department of Commerce, National Bureau of Standards Applied Mathematics Series, No.55 (1970).
- [42] L. van Wijngaarden, On sound radiated by a turbulent bubbly flow, *Journal of Engineering Mathematics* **34** (1998) 45-55.
- [43] J. B. Gilbert, M. S. Howe, R. M. Koch, On sound generated by gas-jet impingement on a bubbly gas-water interface, with applications to supercavity self noise, *Journal of Sound and Vibration* **331** (2012) 4438-4447.
- [44] A. D. Pierce, *Acoustics, An introduction to its principles and applications*, American Institute of Physics, New York, 1989.
- [45] D. T. Blackstock. *Fundamentals of Physical Acoustics*. John Wiley and Sons, Inc., 2000.
- [46] M. S. Howe. *Theory of Vortex Sound*. Cambridge University Press, 2003.

REPORT DOCUMENTATION PAGE					Form Approved OMB No. 0704-0188
<p>The public reporting burden for this collection of information is estimated to average 1 hour per response, including the time for reviewing instructions, searching existing data sources, gathering and maintaining the data needed, and completing and reviewing the collection of information. Send comments regarding this burden estimate or any other aspect of this collection of information, including suggestions for reducing the burden, to Department of Defense, Washington Headquarters Services, Directorate for Information Operations and Reports (0704-0188), 1215 Jefferson Davis Highway, Suite 1204, Arlington, VA 22202-4302. Respondents should be aware that notwithstanding any other provision of law, no person shall be subject to any penalty for failing to comply with a collection of information if it does not display a currently valid OMB control number.</p> <p>PLEASE DO NOT RETURN YOUR FORM TO THE ABOVE ADDRESS.</p>					
1. REPORT DATE (DD-MM-YYYY)	2. REPORT TYPE			3. DATES COVERED (From - To)	
30-04-2015	Final Technical			Jan. 2011 - April 2015	
4. TITLE AND SUBTITLE Study of the Self Noise Generated by Ventilated Supercavitating Vehicles				5a. CONTRACT NUMBER	
				5b. GRANT NUMBER N00014-11-1-0314	
				5c. PROGRAM ELEMENT NUMBER	
6. AUTHOR(S) Gilbert, Jeffrey; Howe, Michael S.				5d. PROJECT NUMBER	
				5e. TASK NUMBER	
				5f. WORK UNIT NUMBER	
7. PERFORMING ORGANIZATION NAME(S) AND ADDRESS(ES) Trustees of Boston University Office of Sponsored Programs 881 Commonwealth Avenue Boston, MA 02215-1303				8. PERFORMING ORGANIZATION REPORT NUMBER	
9. SPONSORING/MONITORING AGENCY NAME(S) AND ADDRESS(ES) Ronald D. Joslin Office of Naval Research, Code 331 875 North Randolph Street Arlington, VA 22203-1995				10. SPONSOR/MONITOR'S ACRONYM(S) ONR 331 - ULI	
				11. SPONSOR/MONITOR'S REPORT NUMBER(S)	
12. DISTRIBUTION/AVAILABILITY STATEMENT Approved for Public Release; distribution is Unlimited.					
13. SUPPLEMENTARY NOTES					
14. ABSTRACT A study is made of the self noise from a ventilated supercavitating vehicle, which could vitiate successful vehicle deployment. A principal noise source is associated with ventilating gas jets impinging on the air-water interface. Analytical models are developed of sound production, with account also taken of bubble entrainment during impingement. Experiments were performed at the Naval Undersea Warfare Center (NUWC Newport RI), including the measurement of the unsteady force spectrum of a gas jet impinging on a rigid wall, and the acoustic pressure spectrum produced by a gas jet striking an air-water interface. Results were compared with theoretical predictions.					
15. SUBJECT TERMS supercavitating vehicle, aerodynamic sound, self noise, jet noise, bubble noise					
16. SECURITY CLASSIFICATION OF: a. REPORT b. ABSTRACT c. THIS PAGE			17. LIMITATION OF ABSTRACT UU	18. NUMBER OF PAGES 156	19a. NAME OF RESPONSIBLE PERSON
					19b. TELEPHONE NUMBER (Include area code)
<p style="text-align: right;">Standard Form 298 (Rev. 8/98) Prescribed by ANSI Std. Z39.18</p>					